

# UC Riverside

## UC Riverside Electronic Theses and Dissertations

### Title

Electrodes/Electrolyte Interphase Design for Li Metal Batteries

### Permalink

<https://escholarship.org/uc/item/07j049zq>

### Author

Zhang, Jian

### Publication Date

2021

Peer reviewed|Thesis/dissertation

UNIVERSITY OF CALIFORNIA  
RIVERSIDE

Electrodes/Electrolyte Interphase Design for Li Metal Batteries

A Dissertation submitted in partial satisfaction  
of the requirements for the degree of

Doctor of Philosophy

in

Materials Science and Engineering

by

Jian Zhang

September 2021

Dissertation Committee:

Dr. Juchen Guo, Chairperson

Dr. Lorenzo Mangolini

Dr. Yadong Yin

Copyright by  
Jian Zhang  
2021

The Dissertation of Jian Zhang is approved:

---

---

---

Committee Chairperson

University of California, Riverside

## ACKNOWLEDGEMENTS

Throughout the writing of this dissertation, I have received a great deal of support and assistance.

First and foremost I am extremely grateful to my supervisor, Prof. Juchen Guo for his ultimate patients and continuous support through my whole Ph.D study. I have benefited from not only his wealth of knowledge and meticulous editing, but also his attitude towards problems in the projects and life. After almost 6 years Ph.D study, I have learned the most important skills for my future life, how to find, analyze, and solve the problems. I also would like to thank University of California, Riverside for providing me the great opportunity to study and enjoy my life. I would like to thank all the committee members who spent the precious time and gave me valuable advice.

I would like to thank my dear wife Dr. Jiayan Shi, who always trust me and encourage me through the ups and downs in my life. Thanks for the discussions about the projects and the advice for my Ph.D study, I always can learn from you. Thanks for your accompany with me, and make me treasure every day. I would like to thank my lovely cats Ginny and Miaomiao, and my lovely dog Peanut, who bring me lots of happy moments during my Ph.D life.

I would like to thank my parents, Wanxing Zhang and Shunying Ke, for your endless support. You have always stood behind me throughout my life. I hope I made you proud. But for your support, I wouldn't have achieved all this.

I would like to thank all my friends, collaborators and other people who either offer the help or teach me a lesson in my Ph.D study, these all makes me become better.

To my dear wife, Dr. Jiayan Shi

To my loving parents, Wanxing Zhang and Shunying Ke

To my advisor, Prof. Juchen Guo

## ABSTRACT OF THE DISSERTATION

Electrodes/Electrolyte Interphase Design for Li Metal Batteries

by

Jian Zhang

Doctor of Philosophy, Materials Science of Engineering  
University of California, Riverside, September 2021  
Prof. Juchen Guo, Chairperson

To understand the baseline performance of lithium (Li) metal anode in liquid electrolytes, the electrochemical and physical properties of Li anode are studied with realistic parameters including: thin thickness ( $50\ \mu\text{m}$ ), practical areal capacity ( $1\ \text{to}\ 4\ \text{mAh}\ \text{cm}^{-2}$ ), practical areal current ( $0.5\ \text{to}\ 2\ \text{mA}\ \text{cm}^{-2}$ ), and low electrolyte/capacity ratio. Two different Li salts, lithium hexafluorophosphate ( $\text{LiPF}_6$ ) and lithium bis(fluorosulfonyl)imide (LiFSI), are used to probe the effects of the electrolyte chemistry and concentration. The cycling of Li||Li symmetric cells, combined with investigation using the scanning electron microscope, demonstrates that the soft-short of Li||Li cells is induced by the continuous volume expansion of Li electrodes during cycling instead of dendrites. The volume change of a Li electrode is dictated by the depth of deposition and stripping (i.e., areal capacity) and the electrolyte/capacity ratio, with no strong correlation with the type of Li salt and concentration. On the other hand, the average coulombic efficiency (CE) measurement demonstrates inherent correlation with the type of Li salt and its concentration in the electrolyte. Li electrode surface chemical analysis indicates that the fluoride-rich surface layer formed in the  $\text{LiPF}_6$  electrolyte can be detrimental to both CE and Li deposition-

stripping overpotential. The failure mechanism of Li metal batteries has been studied in order to design reasonable routine for identify the dominant factor which result in the cell failure.

By thoroughly understanding the failure mechanism of Li metal batteries, the corresponding strategies to mitigate the cell failure has been studied. We report acrylonitrile (AN) as an effective additive in carbonate-based electrolytes to enable uniform and dense lithium (Li) deposition and to improve the coulombic efficiency of Li metal anode. Our electrochemical, spectroscopic, and theoretical study reveal that AN is cathodically electropolymerized on the Li surface prior to the electrochemical decomposition of the electrolyte during Li deposition. The resultant polyacrylonitrile artificial solid electrolyte interphase enables uniform nucleation and growth of Li deposition with significantly reduced side reactions. The effectiveness of the AN additive is demonstrated in 0.4 Ah Li||LiNi<sub>0.6</sub>Mn<sub>0.2</sub>Co<sub>0.2</sub>O<sub>2</sub> pouch cells (using 50- $\mu$ m Li anode, 3 mAh cm<sup>-2</sup> cathode areal capacity, and 4g Ah<sup>-1</sup> electrolyte) with excellent cycle stability under realistic charge-discharge condition.

The hydrofluoric acid (HF) based side reaction in lithium (Li) hexafluorophosphate (LiPF<sub>6</sub>) electrolyte system hindered the direct application of LiPF<sub>6</sub> electrolyte (in organic carbonate solvents) for Li metal batteries. In this study, we report phosphorus pentoxide (P<sub>2</sub>O<sub>5</sub>) as an effective additive in LiPF<sub>6</sub> based electrolyte not only enable uniform and dense Li deposition but also mitigate the transition metal (TM) dissolution and cracking problems of LiNi<sub>0.6</sub>Mn<sub>0.2</sub>Co<sub>0.2</sub>O<sub>2</sub> (NMC622) particle. The poor Li metal deposition behavior and the increasingly growth of cathode impendence caused the poor cycle life of the Li||NMC622

pouch cell in 1M LiPF<sub>6</sub> electrolyte. The cycle life of the pouch cell in 1M LiPF<sub>6</sub> electrolyte with P<sub>2</sub>O<sub>5</sub> additive was greatly enhanced from 30 cycles to more than 230 cycles, with the capacity retention: 87.7% (230 cycles).

## TABLE OF CONTENTS

ACKNOWLEDGEMENTS .....	iv
ABSTRACT OF THE DISSERTATION .....	vii
TABLE OF CONTENTS.....	x
LIST OF FIGURES .....	xiv
LIST OF TABLES.....	xvii
Chapter 1: Introduction.....	1
1.1 Lithium-ion batteries overview.....	1
1.2 Principles of Li-ion batteries and its components.....	1
1.2.1 Mechanism of SEI formation.....	4
1.2.2 Electrode materials for Li-ion batteries .....	5
1.2.3 Electrolyte for Li-ion batteries.....	6
1.2 Motivation of developing Li metal batteries.....	9
1.2.1 Interphase design rules for Li metal anode .....	13
1.3 Conclusion and future directions .....	14
References.....	15
Chapter 2: Properties of thin Li metal anode in carbonate electrolytes .....	18
2.1 Introduction.....	18
2.2 Experimental methods .....	19

2.2.1 Preparation of thin Li electrodes.....	19
2.2.2 Li  Li symmetric coin cells cycling.....	21
2.2.3 Three-electrode GITT measurement.....	21
2.2.4 Electrochemical Impedance Spectroscopy (EIS).....	22
2.2.5 Demonstrating the cause of soft-short .....	22
2.2.6 SEM Characterizations .....	24
2.2.7 Average Coulombic Efficiency Measurement.....	25
2.2.8 EIS Measurement during GITT Li Deposition-Stripping.....	27
2.2.9 XPS Characterizations .....	28
2.3 Results and discussion .....	28
2.4 Conclusions.....	47
References.....	48
Chapter 3: Identification of failure mechanism study of Li metal batteries .....	53
3.1 Introduction.....	53
3.2 Experimental methods .....	54
3.2.1 Materials .....	54
3.2.2 Electrodes preparation for coin-cells and pouch cells .....	54
3.2.3 Cell assembly and electrochemical experiments .....	55
3.3 Results and discussion .....	56

3.4 Conclusion .....	61
References.....	62
Chapter 4: Regulating Lithium Deposition via Electropolymerization of Acrylonitrile in Rechargeable Lithium Metal Batteries .....	
4.1 Introduction.....	63
4.2 Experimental Methods .....	64
4.2.1 Materials .....	64
4.2.2 Cell assembly and electrochemical experiments .....	64
4.2.3 Coulombic efficiency measurement .....	67
4.2.4 Characterization methods.....	68
4.2.5 Computational Method .....	70
4.3 Results and Discussion .....	72
4.4 Conclusion .....	83
References.....	85
Chapter 5: Electrodes/electrolyte interphases stabilization of Li metal battery by phosphorus pentoxide additive in LiPF <sub>6</sub> electrolyte .....	
5.1 Introduction.....	89
5.2 Stabilization of Li metal anode/electrolyte interphase by P <sub>2</sub> O <sub>5</sub> additive .....	92
5.3 Uniform Li deposition layer enabled by P <sub>2</sub> O <sub>5</sub> additive .....	95

5.4 Superior electrochemical performance and the working mechanism of P <sub>2</sub> O <sub>5</sub> additive.....	98
5.5 Conclusion .....	104
5.6 Methods.....	104
5.6.1 Materials .....	104
5.6.2 Electrodes preparation for coin-cells and pouch cells .....	105
5.6.3 Cell assembly and electrochemical experiments .....	106
5.6.4 Average coulombic efficiency measurement.....	108
5.6.5 Li  Li, NMC622  NMC622 symmetric cells for EIS test.....	108
5.6.6 SEM, EDS and FIB.....	109
5.6.7 XPS .....	110
References.....	112
Chapter 6: Summary and future directions .....	117

## LIST OF FIGURES

Figure 1. 1 Schematic diagram of Li-ion cell with graphite anode and LiCoO <sub>2</sub> cathode...	2
Figure 2. 1 Schematics of the preparation for thin Li electrodes.....	20
Figure 2. 2 XPS survey spectrum and Digital images of the lab-made Li electrode and the commercial Li foil.....	20
Figure 2. 3 The configuration of the three-electrode coin cell system for GITT measurement. ....	22
Figure 2.4 Symmetric Li  Li cells cycling curves with electrolyte replenished after soft-short occurred.....	23
Figure 2. 5 Digital images and SEM image of the inner side of the separator showing..	24
Figure 2. 6 SEM images of the Li electrode surface, EDX elemental mapping and elemental composition .....	25
Figure 2. 7 Calibration curve of columbic efficiency measurement.....	27
Figure 2. 8 SEM image of the cross-section of the thin Li electrode on Cu substrate; (b) cycling curve of a Li  Li symmetric cell (c) representative cycling curves and (d) cycle lives of the Li  Li symmetric cells.....	29
Figure 2. 9 Constant-current Li plating-stripping cycling with intermittent GITT measurement .....	31
Figure 2. 10 Galvanostatic Li deposition-stripping curves and EIS Nyquist plots of the symmetric Li  Li cells.....	32
Figure 2. 11 Effect of electrolyte/capacity ratio on the cycle life of Li  Li symmetric cells .....	35
Figure 2. 12 SEM images illustrating the thickness of the deposited Li and the thickness of deposited Li as the function of cycle number .....	37
Figure 2. 13 SEM images of the thickness measurement of the deposited Li layer .....	38
Figure 2. 14 SEM images of the thickness measurement of the deposited Li layer .....	39
Figure 2. 15 Voltage and current profiles in the measurement of average coulombic efficiency and the results.. .....	41

Figure 2. 16 GITT Li deposition-stripping curves and the corresponding charge transfer resistance change. ....	43
Figure 2. 17 Chemical stability of Li electrode in different electrolytes: .....	44
Figure 2. 18 Atomic concentration of Li electrode surface after soaking in different electrolyte for 2 days from XPS analysis.....	46
Figure 3. 1 Schematic diagram illustration of the experimental design for identification of failure mechanism for Li metal batteries. ....	57
Figure 3. 2 Cycling performance of Li metal batteries. ....	58
Figure 3. 3 Illustration of the remaining Li source evaluation by Li  Li symmetric cell. .	60
Figure 4. 1 Optical images of Li  NMC622 pouch cells. ....	66
Figure 4. 2 Voltage and current profiles in the measurement of average CE. ....	68
Figure 4. 3 The initial molecular dynamics simulation cell.....	70
Figure 4. 4 Cathodic linear sweep and galvanostatic Li deposition curves. Calculated reduction potential. SEM images of Li deposited on Cu galvanostatically .....	74
Figure 4. 5 (a) F 1s, (b) S 2p, (c) N 1s XPS spectra, and (d) the atomic percentage .....	75
Figure 4. 6 (a) C 1s and (b) O 1s XPS spectra.....	76
Figure 4. 7 Top-view SEM images of galvanostatic Li deposition. Cross-section SEM images. ....	77
Figure 4. 8 SEM images of deposited Li anode under constant voltage. The corresponding EDX spectra and elemental mapping of deposited Li anode under constant voltage.....	79
Figure 4. 9 Representative cycling curves of Li  Li symmetric cells in lean electrolyte. Average CE of Li deposition-stripping.....	80
Figure 4. 10 Li deposition-stripping CE vs. cycle number from Li  Cu cells with 1mAh cm <sup>-2</sup> areal capacity under (a) 0.5mA cm <sup>-2</sup> and (b) 1mA cm <sup>-2</sup> currents. ....	81
Figure 4. 11 Electrochemical performance of Li  NMC622 cell using 600- $\mu$ m Li anode and 50 $\mu$ L electrolytes with and without AN.....	83
Figure 5. 1 <sup>19</sup> F and <sup>31</sup> P NMR spectra. SEM image of Li metal electrode and the corresponding XPS spectra. ....	92

Figure 5. 2 Nyquist plots at different rest time for Li  Li symmetric cell in 1M LiPF <sub>6</sub> electrolyte (a) without and (b) P <sub>2</sub> O <sub>5</sub> additive.....	94
Figure 5. 3 . Top view SEM images of Li deposited on Li metal. Cross-sectional SEM images of Li deposition layer.....	95
Figure 5. 4 F 1s, P 2p XPS spectra, and the relative atomic percentage of F and P on Li metal foil.....	96
Figure 5. 5 C 1s, O 1s, Li 1s XPS spectra, and) the relative atomic percentage of C, O, and Li on Li metal foil.....	97
Figure 5. 6 Cycling performance of Li  NMC622 pouch cell in lean electrolyte .....	98
Figure 5. 7 dQ/dV vs. voltage plot of the comparison and the deconvoluted EIS analysis of interfacial resistance and charge transfer resistance	100
Figure 5. 8 Nyquist plots for reassembled Li  Li symmetric cell using Li metal anodes after cycling in Li  NMC622 full cells and schematic illustration of the impedance fitting model for reassembled Li  Li symmetric cell.....	102
Figure 5. 9 EDS spectra of Li metal anode and FIB-SEM images of NMC622 particles .....	103
Figure 5. 10 Optical images for Li  NMC622 pouch cells.....	107

## LIST OF TABLES

Table 1. 1 Positive electrode materials for Li-ion batteries. ....	5
Table 1. 2 Approximate weight for the components of a Panasonic NCR18650B .....	10
Table 3. 1 Cell parameters and testing conditionals for the Li  NMC622 cell.....	56
Table 3. 2 Summary of the discharge capacity by changing parts after cell dead .....	59
Table 4. 1 Bond dissociation energy in gas and solution phase in AN.....	73
Table 4. 2 Cell parameters of the 0.4Ah Li  NMC622 pouch cell. ....	82
Table 5. 1 <sup>19</sup> F and <sup>31</sup> P NMR spectra data of electrolyte without and with P <sub>2</sub> O <sub>5</sub> additive. 93	
Table 5. 2 Relative sensitivity factors for Karatos AXIS. ....	110

## **Chapter 1: Introduction**

### **1.1 Lithium-ion batteries overview**

Through the continuously improvements, Li-ion batteries have become the most predominant energy storage devices owing to its high capacity, low cost and long cycle life. In 2019, three scientists (John B Goodenough, M Stanley Whittingham, and Akira Yoshino) have been awarded the Nobel Prize in Chemistry for the development of Li-ion batteries. However, the developments of mature Li ion batteries were not easy and lasted for several decades.

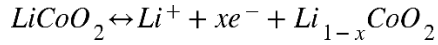
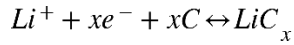
In 1960s, the unique characteristics of Li (low negative electrode potential and light weight) and the reversible insertion of Li ion into layered transition metal sulfides attracted the high interests. In 1976, Stanley Whittingham, who was hired by the Exxon Mobil Corporation, created the rechargeable Li battery by layered titanium disulfide.<sup>1</sup> During that time, John B Goodenough has investigated the stable extraction of Li from  $\text{LiCoO}_2$  could reach over half and without critical structure change. And the anode material was found by Akira Yoshino, who studied the carbon-rich anode materials. Then in 1991, Sony released the first commercial Li-ion battery, and after that, the revolution of mobile devices has start changing significantly.

### **1.2 Principles of Li-ion batteries and its components**

The basic Li-ion cells typically consists of anode (negative electrode), cathode (positive electrode) and electrolyte, which are illustrated in **Figure 1.1**.<sup>2</sup>

In this specific example, graphite is the anode, lithium cobalt oxide (LiCoO<sub>2</sub>) is the cathode.

The reactions are as follows:



During discharging, Li ion undergo the extraction from layered graphite anode materials and migrate through electrolyte and inserted into anode materials. At the same time, the generated electrons from anode would flow through external circuit and arrive at positive electrode, to participate the reduction reaction in cathode.

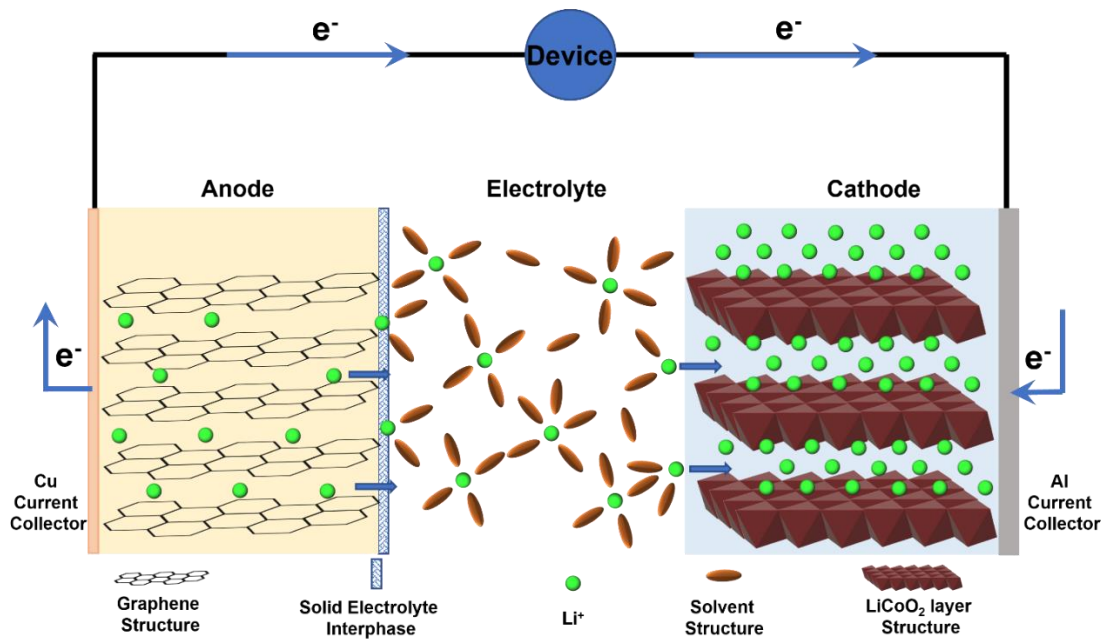


**Figure 1. 1** Schematic diagram of Li-ion cell with graphite anode and LiCoO<sub>2</sub> cathode.

The open circuit voltage of the cell ( $V_{OC}$ ) is determined by the difference between the electrochemical potential of anode ( $\mu_A$ ) and cathode ( $\mu_C$ ), which was shown in **Figure 1.2**

a.

$$V_{OC} = \frac{\mu_A - \mu_C}{e}$$

Where  $e$  is the magnitude of electronic charge. The open circuit potential is confined by the electrochemical potentials of electrodes and the electrochemical window of electrolyte.<sup>3</sup>

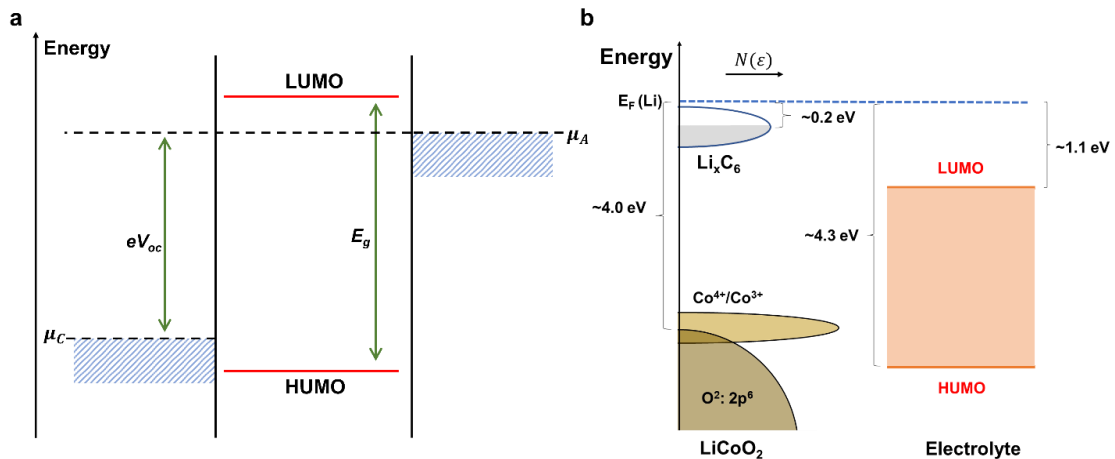


**Figure 1.2** (a) Relative energies of electrolyte window and electrodes electrochemical potentials without electrodes/electrolyte reactions. (b) scheme diagram of energy level for characteristic Li-ion battery (graphite as anode and LiCoO<sub>2</sub> as cathode with carbonate electrolyte system).<sup>3</sup>

In **Figure 1.2** a, the electrochemical window of the electrolyte is determined by the energy level difference ( $E_g$ ) between the highest occupied molecular orbital (HUMO) and the lowest unoccupied molecular orbital (LUMO). In principle, the electrochemical potential of electrodes should be located within the electrochemical window of electrolyte. Otherwise, the reduction reaction would take place on anode if  $\mu_A$  is higher than the LUMO of the

electrolyte or the oxidation reaction would take place on cathode if  $\mu_C$  is lower than the HUMO of the electrolyte, to form a passivating solid electrolyte interphase (SEI) film.

### 1.2.1 Mechanism of SEI formation

The typical example could be found in **Figure 1.2b**, this is a schematic energy diagram of relative energy position of battery components consisting of graphite anode, LiCoO<sub>2</sub> cathode and organic carbonate electrolytes. The carbonate electrolytes (DMC/DEC electrolytes) usually offer a electrochemical window of ~3 eV, where the LUMO level of the electrolyte is ~1.1eV lower than  $\mu_A(Li)$  (electrochemical energy of Li),<sup>4</sup> and the HUMO level of the electrolyte is ~ 4.3 eV below  $\mu_A(Li)$ .<sup>5</sup>

The energy level of layered oxide cathode materials is ~ 4.0 eV below  $\mu_A(Li)$ ,<sup>6,7</sup>

so that the cathode electrolyte interphase would be stable before the electrochemical energy level change for cathode. However, for graphite anode, its energy level lies ~ 0.2 eV below  $\mu_A(Li)$ <sup>7</sup>, which higher than the LUMO of the carbonate electrolyte (~1.1 eV below  $\mu_A(Li)$  for DMC/DEC electrolytes). The reduction reaction between graphite and carbonate electrolytes would happen once the charging process take place, and it will be stopped until a stable SEI layer forms.

## 1.2.2 Electrode materials for Li-ion batteries

**Table 1. 1** Positive electrode materials for Li-ion batteries.

Material	Nominal Voltage (V)	Specific Capacity (mAh g <sup>-1</sup> )
LiCoO <sub>2</sub>	3.6-3.7	140
LiFePO <sub>4</sub>	3.2	150
LiNi <sub>x</sub> Mn <sub>y</sub> Co <sub>z</sub> O <sub>2</sub>	3.6-3.7	180-220
LiMn <sub>2</sub> O <sub>4</sub>	3.7-3.8	120

LiCoO<sub>2</sub> was the firstly used cathode material in commercialized Li-ion batteries and is still widely used in consumer products. However, considering the safety and total inventory of cobalt in the world, the market has reducing the manufacturing of Li-ion batteries consists of LiCoO<sub>2</sub> as cathode material. Lithium iron phosphate (LiFePO<sub>4</sub>) has very good stability for Li-ion batteries and considering its low cost, the LiFePO<sub>4</sub> batteries are suitable for off-grid products. The lower capacity of LiFePO<sub>4</sub> and the lower output voltage than competing Li-ion chemistries makes it not suitable for the application for electric vehicles.<sup>8</sup>

The lithium nickel manganese cobalt oxide (NMC) could be the most promising cathode materials for Li-ion batteries used in electric vehicles considering the good cycle life, safety and high capacity. Although lithium manganese oxide could offer higher voltage and good thermal stability, the lower cycle life limited its application.

As for the anode materials for Li-ion batteries, graphite is the mostly used anode materials including: natural graphite, artificial graphite or amorphous carbon.<sup>9</sup>

Lithium titanate (LTO) anode materials have much better safety, thermal stability and low temperature operation. The Li-ion batteries made by LTO anode will offer very high cycle life. However, the much lower energy density limit its application in Li-ion batteries because of the low cell voltage (2.4 V).

### 1.2.3 Electrolyte for Li-ion batteries

For Li-ion battery electrolytes, they are usually consists of Li salts and organic solvents. The solvents are usually a mixture of two or more solvents. The rationale behind that is the diverse and often the contradicting requirements of battery applications can hardly be fulfilled by single solvent, for example, the high fluidity versus high dielectric constant.<sup>2</sup>

The requirements of electrolytes for Li-ion batteries should have reasonable Li ion conductivity and stable against electrodes. The most commonly used Li salts and solvents are listed below.

Einstein Stokes equation:

$$D = \frac{k_B T}{6\pi\mu R} \quad (1)$$

Conductivity vs. Diffusivity

$$\sigma = \frac{q^2 C}{k_B T} D \quad (2)$$

$$\sigma = \frac{q^2 C}{6\pi\mu R} \quad (3)$$

From Einstein-Stokes equation and the relationship between conductivity and diffusivity,<sup>10</sup> the general equation for conductivity for electrolyte was described in equation (3),

Where  $\sigma$  is ionic conductivity,  $q$  is charge,  $C$  is the concentration of electrolyte,  $\mu$  is the viscosity and  $R$  represents the hydrodynamic radius. In order to increase the electrolyte ionic conductivity, the higher concentration and smaller viscosity and hydrodynamic radius of Li ion should obtain from equation (3). However, with the addition of lithium salt, the viscosity of the electrolyte would also increase. So, normally, the conductivity of the electrolyte would have optimum value.<sup>11</sup>

The stability of electrolyte against electrodes mainly contains two parts: (1) forming stable decomposition layer on electrodes (for example: the SEI for graphite electrodes); (2) wide electrochemical window to prevent electrolyte being oxidized or reduced.

The most famous example of the SEI enabling good performance of Li-ion batteries can be found in the comparison between EC (ethylene carbonate) and PC (propylene carbonate) based electrolytes. The successful application of Li-ion batteries was largely depending on the introduction of EC in the organic electrolyte for its stable SEI formation capability. However, for PC based electrolyte in Li-ion batteries, the SEI formation by PC reduction on graphite anode can not form stable robust SEI may be due to the more severe gas evolution (ethylene gas) (Basenhard Model) and the methyl group in PC structure hindered the formation of compact SEI (Peled's Model).<sup>2,12</sup>

For Li-ion batteries with transition metal oxide cathodes, the HUMO energy level of the electrolytes should located above the energy level of cathodes ( $\sim 4.0$  eV below  $\mu_A(Li)$ ).

Organic carbonates-based electrolytes are able to fulfill this requirement while the ethers are usually have lower HOMO energy level than the energy level of cathodes. In other word, the electrolyte would oxidize on cathode surface.<sup>2</sup>

## 1.2 Motivation of developing Li metal batteries

Lithium metal anode has generated great interest in recent years owing to the unique properties: it has the lowest electrochemical potential ( $\sim 3.0\text{V}$  vs SHE), which delivers a high cell voltage when pairing with certain cathodes (for example, lithium transition metal oxides), and it is the lightest metal ( $0.534\text{g/cm}^3$ ), which provides high theoretical capacity at  $3860\text{mAh/g}$ .

Research on lithium metal batteries went ups and downs during the past seventy years. Stabilizing lithium metal in certain non-aqueous solvents was first started from 1950s.<sup>13</sup> From 1960s to 1970s<sup>14</sup>, lithium based primary cells were invented and commercialized. Continued research found needlelike lithium crystals (called “dendrite”) growth upon plating and “dead lithium” form stripping causing continuous reaction between lithium and electrolyte, which result in low columbic efficiency and even internal short when dendrite pierces the separator. In addition, in 1989, the incident of fire caused by lithium metal in rechargeable battery highlighted the end of general enthusiasm in lithium metal anode.<sup>15</sup> To composite the demand of increasing high energy density batteries, in 1991, Sony release the first lithium-ion battery using graphite as anode and  $\text{LiCoO}_2$  as cathode.<sup>16</sup> Followed by other lithium transition metal oxide materials proposed by John Goodenough. After that, Li-ion batteries have made a great success in the last twenty years.

However, the intercalation mechanism that fundamentally enables the excellent cycling of Li-ion batteries also places an upper limit on energy density because of the weight and volume of the hosts into which  $\text{Li}^+$  intercalates. The current Li-ion batteries cannot meet the requirements of US Department of Energy’s (DOE) electric vehicle pack goals: increase the electric vehicle range to 300 miles with reasonable price ( $<100$  \$/ kWh for cell, and  $<125$  \$/ kWh for battery pack), which corresponded to the energy content of  $\sim 350$  Wh  $\text{kg}^{-1}$  and  $750$  Wh  $\text{L}^{-1}$  at cell level.<sup>17</sup> Nowadays the high-energy demand inspires the resurgence of lithium metal investigations. Motivation of this project comes from significant increase in specific energy density, more than 28 percentage as

shown in supporting information, by simply changing graphite anode with lithium metal anode.<sup>18</sup>

**Table 1. 2** Approximate weight for the components of a high energy density Panasonic NCR18650B [6]

Component	Weight(g)
Passive Weight	14.1
Graphite	11.4
NCA	17.4
Electrolyte	5.3
Total weight	48.2

The Specific energy density of a NCR18650B cell:

$$= \frac{(\text{Specific Capacity of Electrode} \times \text{Electrode Weight})}{(\text{Battery Weight})} \times \text{Voltage}$$

$$= \frac{285\text{mAh/g} \times 11.4\text{g}}{48.2\text{g}} \times 3.6\text{V} = 243\text{Wh/kg}$$

Simply replacing graphite electrode with lithium metal anode, the theoretical weight of lithium metal needed (N/P = 2) is:

$$\text{Theoretical weight of lithium metal needed:} = \frac{285\text{mAh/g} \times 11.4\text{g}}{3860\text{mAh/g}} = 0.84\text{g}$$

Then the specific energy density of lithium metal battery could be

$$= \frac{285\text{mAh/g} \times 11.4\text{g}}{48.2 - 11.4 + 0.84} \times 3.6\text{V} = 310\text{Wh/kg},$$

there will be 28% increasing in specific energy density.

However, there are several critical problems arising from changing the graphite anode with lithium metal. The transformation of lithium electrode from fully dense metal to porous dead lithium during cycling will cause volume expansion and low coulombic efficiency. The new deposited lithium not only grows dendrite toward opposite electrode to lead to uncontrollable safety issue, but also

continuously react with electrolyte to form new solid electrolyte interphase (SEI) when deposition, which consuming lots of electrolyte and wrapping the lithium tightly, then form dead lithium when being stripped.

Lots of efforts have been made to suppress the uncontrollable dendritic lithium growth during the past few decades. All the works can be divided into four strategies:

1. Directly adding electrolyte additives to stabilize the SEI film. In most electrolytes, polar aprotic solvent such as ethers and carbonates are widely used, which is strongly reactive to lithium metal. Thus the component in the electrolyte originally determines the properties of the SEI film, as indicated by Aurbach.<sup>19</sup> An recent example by Choudhury *et al.*<sup>20</sup> showed that by adding additional 0.5 wt.% of LiF to 1M LiPF<sub>6</sub> in EC:DMC (50:50 volume ratio), the coulombic efficiency reach higher than 90% and the lifetime of cells increase to hundreds of hours (4mAh/cm<sup>2</sup>, 1C, 140 hours) owing to the better protection of lithium metal.

2. Forming robust artificial SEI layer before cell cycling. Recently, Jie<sup>21</sup> *et al.* showed that a surface fluorination process developed a chemically stable and mechanically strong interfacial LiF layer for suppressing the dendrite formation. Over 300 stable cycles were realized in carbonate electrolytes even at current densities of 5mA/cm<sup>2</sup>.

3. Replacing routine liquid electrolytes with solid-state inorganic or polymer electrolytes. The conventional liquid electrolyte not only has the problem of chemically and electrochemically instability, but also will cause several potential safety issues such as electrolyte leakage and flammability. While introducing solid state electrolyte can not only partially solve these problems but also can suppress the formation of dendritic lithium because of its high modulus. Li iron phosphate (LiFePO<sub>4</sub>)|Li<sub>7</sub>La<sub>3</sub>Zr<sub>2</sub>O<sub>12</sub> (LLZO)|Lithium cell has been reported exhibiting good cycling performance, about 146.2 mAh g<sup>-1</sup> capacity retention after 100 cycles at 14.62mAh g<sup>-1</sup>.<sup>22</sup>

4. Constructing host for lithium metal anode. Lithium undergoes infinite volume change during

stripping-plating thus decreasing the mechanical stability of SEI layer and causing safety issue due to the expansion of battery. Cheng et al.<sup>23</sup> use glass-fiber modified electrode to regulating lithium deposition and dissolution in order to render the dendrite growth and maintain up to 500 cycles. Although the work mentioned above have reported good cycling performance using specific strategies, one important factor being ignored is the thickness of the lithium foil. Recently, Albertus et al.<sup>24</sup> reported that using limited amount of lithium metal can conclusively identify the presence of electronic shorting. In addition, the measurement of coulombic efficiency will be more meaningful by using limited amount of lithium. Thus, it motivates this project to apply thin lithium metal in the proposed research

### 1.2.1 Interphase design rules for Li metal anode

The short cycle life of Li metal anode has been one of the major limitation for Li metal batteries. In organic liquid electrolyte system, the failure mechanism of Li metal anode could be summarized in **Scheme 1.1**. The failure of the Li metal anode results from the high porosity Li deposition integrated with accumulation of dead Li, which leads to the low diffusion coefficient of electrolyte in this region then causing the large concentration overpotential.<sup>25</sup> The high porosity Li deposition was due to the poor electrolyte which either generate SEI with poor mechanical properties or has slow SEI formation rate.<sup>26</sup>



**Scheme 1. 1** Failure mechanism of Li metal anode

Apart from the ex-situ strategies (e.g. artificial SEI), the high SEI formation rate could be achieved by adding the electrolyte additives which have higher reduction potential and lower activation energy of reduction reactions than the electrolyte components.<sup>26</sup>

The SEI properties usually were tuned by changing the solvent formulations in low concentration electrolyte, or using the high concentration electrolyte to form salt decomposition dominated SEI rather than solvent decomposition dominated SEI.<sup>27</sup>

The screening of electrolyte is always accompanying with the properties of solid electrolyte interphase between electrodes and electrolytes, no matter from the exfoliation problem of graphite anode causing by polypropylene carbonate solvent or the nature of unstoppable chemical reaction between Li metal and electrolyte components.

### **1.3 Conclusion and future directions**

Although Li metal batteries have been regarded as the most promising next-generation Li batteries, there are a lot of improvements need to be done (e.g. safety and cycle life) before its commercialization.

Electrolyte formulation optimization is the most important direction for stabilize the electrolyte/electrodes interphases.

## References

- (1) Goodenough, J. B. (2018). How we made the Li-ion rechargeable battery. *Nature Electronics*, 1(3), 204-204.)
- (2) Xu, K. (2004). Nonaqueous liquid electrolytes for lithium-based rechargeable batteries. *Chemical reviews*, 104(10), 4303-4418.
- (3) Graphite as anode and LiCoO<sub>2</sub> as cathode with carbonate electrolyte system). (Goodenough, J. B., & Park, K. S. (2013). The Li-ion rechargeable battery: a perspective. *Journal of the American Chemical Society*, 135(4), 1167-1176.
- (4) Zhang, X., Kostecki, R., Richardson, T. J., Pugh, J. K., & Ross Jr, P. N. (2001). Electrochemical and infrared studies of the reduction of organic carbonates. *Journal of The Electrochemical Society*, 148(12), A1341.
- (5) Egashira, M., Takahashi, H., Okada, S., & Yamaki, J. I. (2001). Measurement of the electrochemical oxidation of organic electrolytes used in lithium batteries by microelectrode. *Journal of power sources*, 92(1-2), 267-271.
- (6) Kim, Y., Park, K. S., Song, S. H., Han, J., & Goodenough, J. B. (2009). Access to M<sup>3+</sup>/M<sup>2+</sup> redox couples in layered LiMS<sub>2</sub> sulfides (M= Ti, V, Cr) as anodes for Li-ion battery. *Journal of the Electrochemical Society*, 156(8), A703.
- (7) Goodenough, J. B., & Kim, Y. (2010). Challenges for rechargeable Li batteries. *Chemistry of materials*, 22(3), 587-603.
- (8) Ding, Yu, Pei Pan, Lihui Chen, Zhengbing Fu, Jun Du, Liangui Guo, and Feng Wang. LiFePO<sub>4</sub> composites decorated with nitrogen-doped carbon as superior cathode materials for lithium-ion batteries. *Ionics* 23.12 (2017): 3295-3302.
- (9) Garche J, Brandt K, In: Li-Battery Safety. Elsevier; 2018 Chapter 3.3
- (10) Park, M., Zhang, X., Chung, M., Less, G. B., & Sastry, A. M. (2010). A review of conduction phenomena in Li-ion batteries. *Journal of power sources*, 195(24), 7904-7929.
- (11) Logan, E. R., & Dahn, J. R. (2020). Electrolyte design for fast-charging Li-ion batteries. *Trends in Chemistry*, 2(4), 354-366.
- (12) Aurbach, D., Teller, H., & Levi, E. (2002). Morphology/behavior relationship in reversible electrochemical lithium insertion into graphitic materials. *Journal of The Electrochemical Society*, 149(10), A1255.
- (13) Jasinski, R. *High Energy Batteries*; Plenum Press: New York, 1967.

- (14) A. V. Fraioly, W. Barber, A. M. Feldman, A. M. U.S. Patent 3,551,205, 1970.
- (15) I. Yoshimatsu, T. Hirai, J-I Yamaki, Lithium Electrode Morphology during Cycling in Lithium Cells Electrochemical Science and Technology J. Electrochem. Soc. 1988, 135, 2422.
- (16) L. A. Dominey, In Nonaqueous Electrochemistry, D. Aurbach, Ed. Marcel-Dekker: New York, 1999, Chapter 8.
- (17) Schmuch, R., Wagner, R., Hörpel, G., Placke, T., & Winter, M. (2018). Performance and cost of materials for lithium-based rechargeable automotive batteries. *Nature Energy*, 3(4), 267-278.
- (18) M. Hagen, D. Hanselmann, K. Ahlbrecht, R. Maça, D. Gerber, J. Tübke, Lithium–Sulfur Cells: The Gap between the State-of-the-Art and the Requirements for High Energy Battery Cells, *Adv. Energy Mater.* 2015, 5, 1401986
- (19) D. Aurbach, E. Zinigrad, Y. Cohen, H. Teller, A short review of failure mechanisms of lithium metal and lithiated graphite anodes in liquid electrolyte solutions, *Solid State Ionics* 148 (2002) 405– 416
- (20) S. Choudhury, L. A. Archer, Lithium Fluoride Additives for Stable Cycling of Lithium Batteries at High Current Densities, *Adv. Electron. Mater.* 2016, 2, 1500246
- (21) J. Zhao, L. Liao, F. Shi, T. Lei, G. Chen, A. Pei, J. Sun, K. Yan, G. Zhou, J. Xie, C. Liu, Y. Li, Z. Liang, Z. Bao, Y. Cui, Surface Fluorination of Reactive Battery Anode Materials for Enhanced Stability, *J. Am. Chem. Soc.* 2017, 139, 11550–11558
- (22) X. Yan, Z. Li, Z. Wen, W. Han, Li||Li<sub>7</sub>La<sub>3</sub>Zr<sub>2</sub>O<sub>12</sub>/LiFePO<sub>4</sub> All-Solid-State Battery with Ultrathin Nanoscale Solid Electrolyte, *J. Phys. Chem. C* 2017, 121, 1431–1435
- (23) X. Cheng , T. Hou , R. Zhang , H. Peng , C. Zhao , J. Huang , and Q. Zhang, Dendrite-Free Lithium Deposition Induced by Uniformly Distributed Lithium Ions for Efficient Lithium Metal Batteries, *Adv. Mater.* 2016, 28, 2888–2895
- (24) P. Albertus, S. Babinec, S. Litzelman, A. Newman, Status and challenges in enabling the lithium metal electrode for high-energy and low-cost rechargeable batteries, *Nature Energy*, 3, pages16–21 (2018)
- (25) Chen, K. H., Wood, K. N., Kazyak, E., LePage, W. S., Davis, A. L., Sanchez, A. J., & Dasgupta, N. P. (2017). Dead lithium: mass transport effects on voltage, capacity, and failure of lithium metal anodes. *Journal of Materials Chemistry A*, 5(23), 11671-11681.
- (26) He, M., Guo, R., Hobold, G. M., Gao, H., & Gallant, B. M. (2020). The intrinsic behavior of lithium fluoride in solid electrolyte interphases on lithium. *Proceedings of the National Academy of Sciences*, 117(1), 73-79.

- (27) Cao, X., Jia, H., Xu, W., & Zhang, J. G. (2021). Localized High-Concentration Electrolytes for Lithium Batteries. *Journal of the Electrochemical Society*, 168(1), 010522.

## Chapter 2: Properties of thin Li metal anode in carbonate electrolytes

### 2.1 Introduction

The increasing demand for high-capacity lithium-ion (Li-ion) batteries has revived the development of Li metal as an anode material due to its high capacity and low electrochemical potential. To date, using metallic Li in practical Li-ion batteries is still elusive mainly due to its short life span and grave safety concerns. Conventional wisdom attributes the safety hazards of the Li anode to Li dendrite formation and growth. However, this cursory reasoning may mask subtle but critical occurrences during the Li deposition-stripping. For instance, the formation of metal dendritic structures typically implies deposition under mass transfer limitation with local current higher than a certain threshold. However, numerous investigations show that Li anodes still fail by internal short under fairly low current. Therefore, the short cycle life and internal shorting of Li anodes should not be simply attributed to dendrite formation. In this work, we aim to elucidate the failure (internal short) mechanism of Li||Li symmetric cells, which have been widely adopted in Li metal anode research. Moreover, despite the tremendous amount of strategies being studied to improve Li metal anodes (such as electrolyte additives<sup>1-5</sup>, high-concentration electrolytes<sup>6-11</sup>, protective coating<sup>12-18</sup>, porous host structures for Li<sup>19-26</sup>, and solid-state electrolytes<sup>27-32</sup>), many reported experimental parameters, including the thickness of the Li electrode, areal capacity, areal current, and the electrolyte/capacity ratio significantly deviate from realistic use conditions. As a result, the relevance of the resultant performances may be questionable. Liu and coworkers demonstrated that under a realistic current of  $1.27 \text{ mA cm}^{-2}$ , the cycle life of Li anodes drastically declined from more than 60

cycles to 20 cycles when their thickness decreased from 250  $\mu\text{m}$  to 50  $\mu\text{m}$ .<sup>33</sup> Albertus and coworkers further pointed out that the volume of electrolyte used in the batteries is a parameter crucial to the determination of the cycle life of Li anodes and the cell-level energy density.<sup>34</sup> Therefore, we study here the relationship between cycle stability and experimental parameters in liquid electrolytes using thin Li foil, practical capacity and current, and a controlled electrolyte/capacity ratio. The deposition-stripping efficiency is also studied under these realistic parameters along with the surface chemical properties of the Li electrode in carbonate electrolytes, which are based on either lithium hexafluorophosphate ( $\text{LiPF}_6$ ) or lithium bis(fluorosulfonyl)imide ( $\text{LiFSI}$ ).

## **2.2 Experimental methods**

### **2.2.1 Preparation of thin Li electrodes**

A chunk of clean Li was obtained from cutting off the outside layer of a Li rod (99.8%, Strem Chemicals) with clean stainless steel blades. The obtained Li chunk was sandwiched between two pieces of laminated aluminum film (MTI Corporation) with the polyamide side facing the lithium chunk. The protected Li chunk was pressed with a mechanical roller (MTI Corporation) to yield the Li foil with a thickness of 50  $\mu\text{m}$ . The Li foil was subsequently pressed onto a copper foil (99.96%, Lyon Industries) with the protection of laminated aluminum film on top, with the polyamide side facing the Li surface. The Cu substrate was pre-treated in flow gas composed of 95% argon and 5%  $\text{H}_2$  at 300  $^\circ\text{C}$  for 12 hours in a tube furnace. All the procedures were performed inside an argon-filled glovebox, as illustrated in **Figure 2.1**.

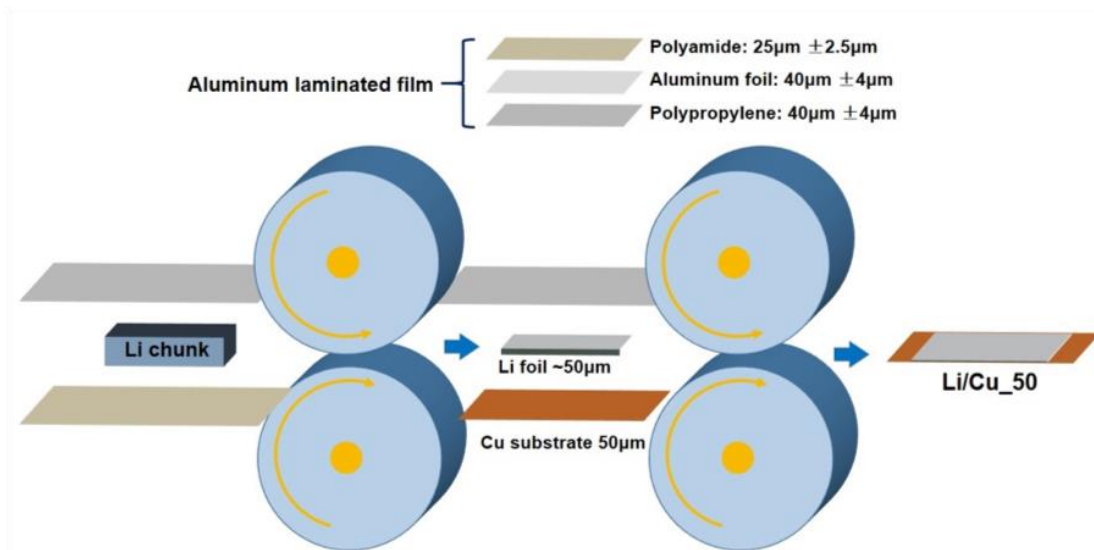


**Figure 2. 1** Schematics of the preparation for thin Li electrodes by mechanical rolling process.

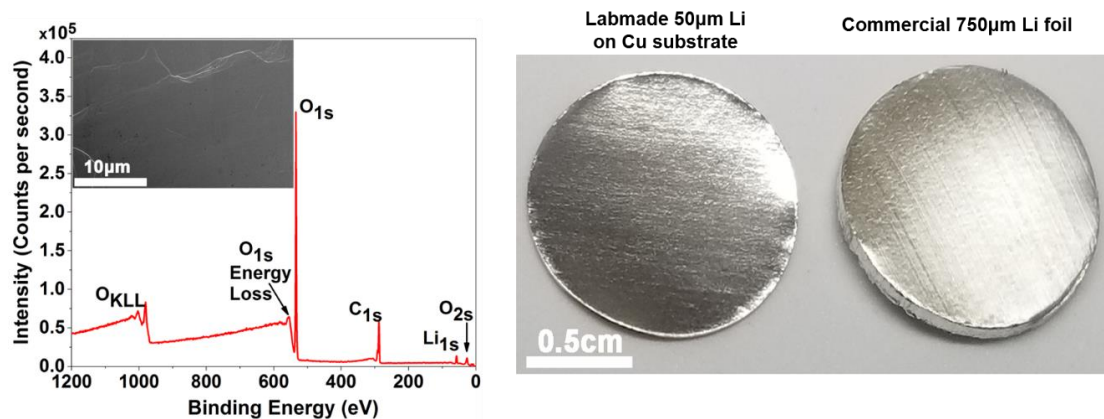


**Figure 2. 2** (Left) XPS survey spectrum of the lab-made 50µm Li electrode with SEM image of the Li surface as the inset and (Right) Digital images of the lab-made Li electrode and the commercial Li foil.

### 2.2.2 Li||Li symmetric coin cells cycling

CR 2016 type coin cells were used to measure the cycle stability. Two 50 $\mu$ m lithium electrodes were used with a single piece of Celgard<sup>®</sup> 3501 separator. The solvent of all electrolytes is a mixture of ethylene carbonate (EC, anhydrous, 99%, Sigma-Aldrich) and diethyl carbonate (DEC, anhydrous,  $\geq$  99%, Sigma-Aldrich) with 1:1 volume ratio. The electrolyte of 1 M LiPF<sub>6</sub> in EC/DEC was purchased from Sigma-Aldrich and used as received. The 1 M and 5 M LiFSI (99%, Oakwood Chemical) electrolytes were prepared in-house. The solvents were re-distilled prior to use.

### 2.2.3 Three-electrode GITT measurement

The galvanostatic intermittent titration technique (GITT) experiments were performed using both two-electrode Li||Li symmetric coin cells and the three-electrode coin cells. The construction of three-electrode coin cells, illustrated in **Figure 2.3**, was modified from the work of Juarez-Robles et al.<sup>1</sup> The GITT experiments were introduced after a certain number of normal cycles of 15-second current-pulse followed by 3-minute rest. The cycling between current-pulse and rest continued until the designated capacity was reached.

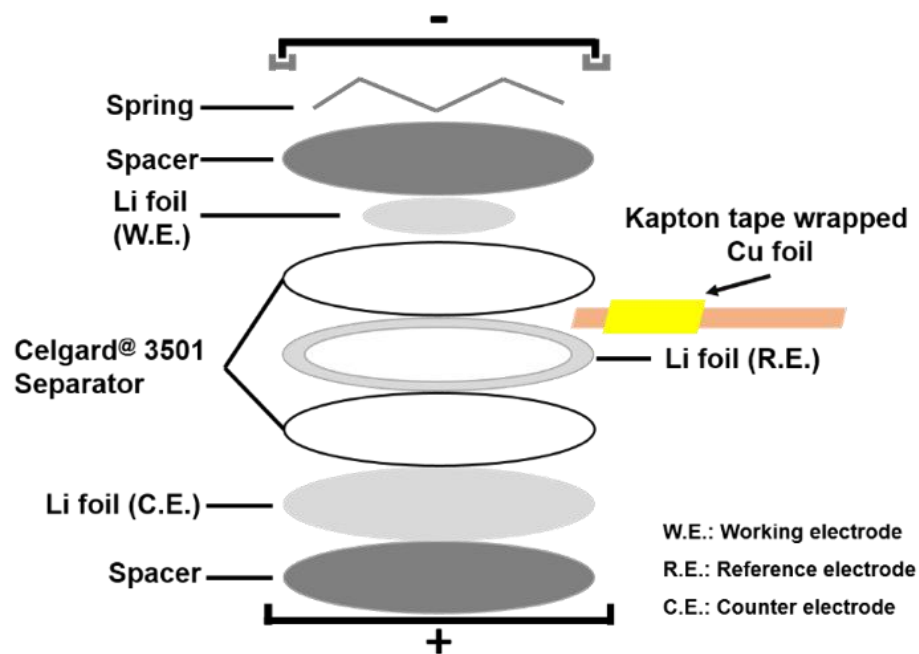


**Figure 2. 3** The configuration of the three-electrode coin cell system for GITT measurement.

### 2.2.4 Electrochemical Impedance Spectroscopy (EIS)

The EIS measurements were conducted using the Gamry potentiostat Interface 1000, scanning over the frequency range from  $10^6$  Hz to 0.1 Hz with 2 mV amplitude. After a set number of cycles (1 cycle, 6 cycles and 11 cycles), the Li||Li symmetric cells were stopped from further cycling, rested for 2 hours, and evaluated using EIS measurement. The galvanostatic cycling was resumed after the EIS measurement.

### 2.2.5 Demonstrating the cause of soft-short

The symmetric Li||Li coin cells were carefully disassembled after the soft-short occurred. The two Li electrodes were retrieved and reassembled in a new coin cell with a new separator and replenished electrolyte, after which cycling was resumed. In other

experiments, the retrieved Li/separator/Li assembly was enclosed in a new coin cell with replenished electrolyte followed by resumed cycling. As shown in **Figure 2.4**, the replenished electrolyte is not enough to resume normal Li||Li cycling.

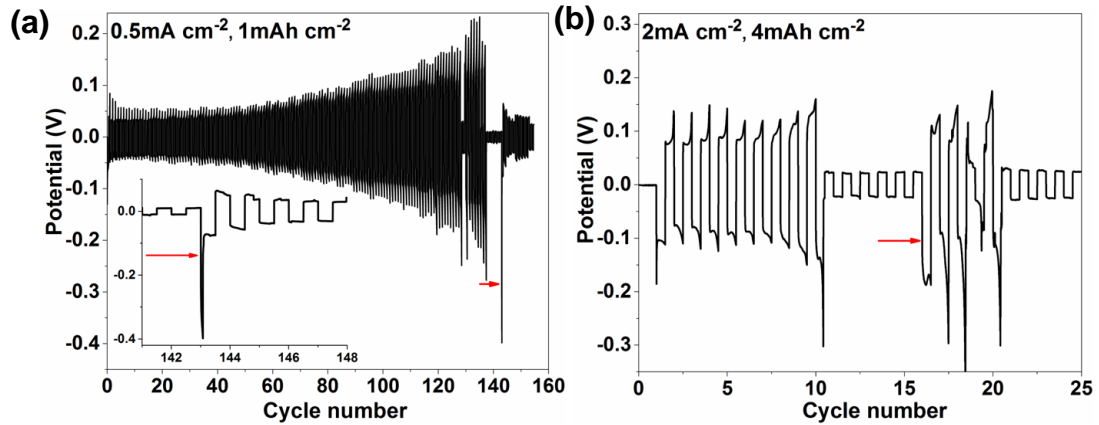


**Figure 2.4** Symmetric Li||Li cells cycling curves with (a) 0.5 mA cm<sup>-2</sup>, 1 mAh cm<sup>-2</sup> and (b) 2 mA cm<sup>-2</sup>, 4 mAh cm<sup>-2</sup> with electrolyte replenished after soft-short occurred.

To further demonstrate the cause of the soft-short, two separators were used in some symmetric Li||Li cells. After soft-short occurred, the coin cells were disassembled and the two separators were retrieved. As shown in **Figure 2.5**, dead Li (dark color area in (a) and (b)) was found on the inner side of both separators (the side at which the two separators were in contact). **Figure 2.5c** displays the SEM image of the Li breaching the separator.

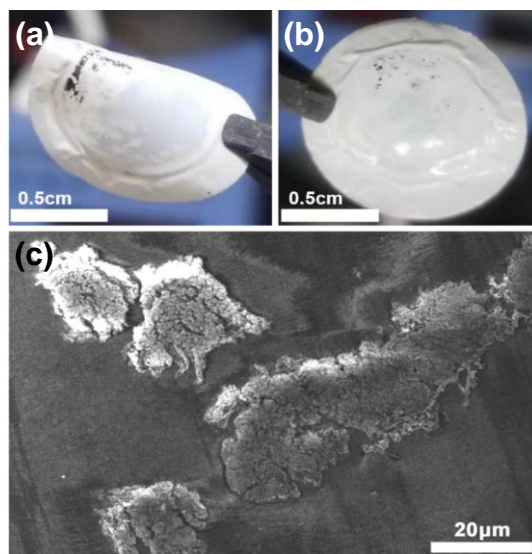


**Figure 2. 5** (a-b) Digital images of the inner side of the two separators. (c) SEM image of the inner side of the separator showing Li breaching it.

### 2.2.6 SEM Characterizations

The structure and thickness of the Li electrode in the symmetric cells were characterized using scanning electron microscope (SEM, Nova Nano S450, 20 kV). The Li electrodes were immersed in different electrolyte for 2 days prior to SEM and EDS analysis. The samples were retrieved in an argon-filled glove box and washed with dimethyl carbonate thoroughly to remove the residual electrolyte. Prior to the SEM, the samples were dried at room temperature for 24 hours inside the argon-filled glove box. The samples were transported to the SEM facility inside a stainless-steel tube with KF-flange sealing. The samples were loaded in the SEM using a glove-bag with argon purging gas. The elemental mapping of the samples was collected using an Energy Dispersive X-ray Spectroscopy (EDX) spectrometer coupled with the SEM.

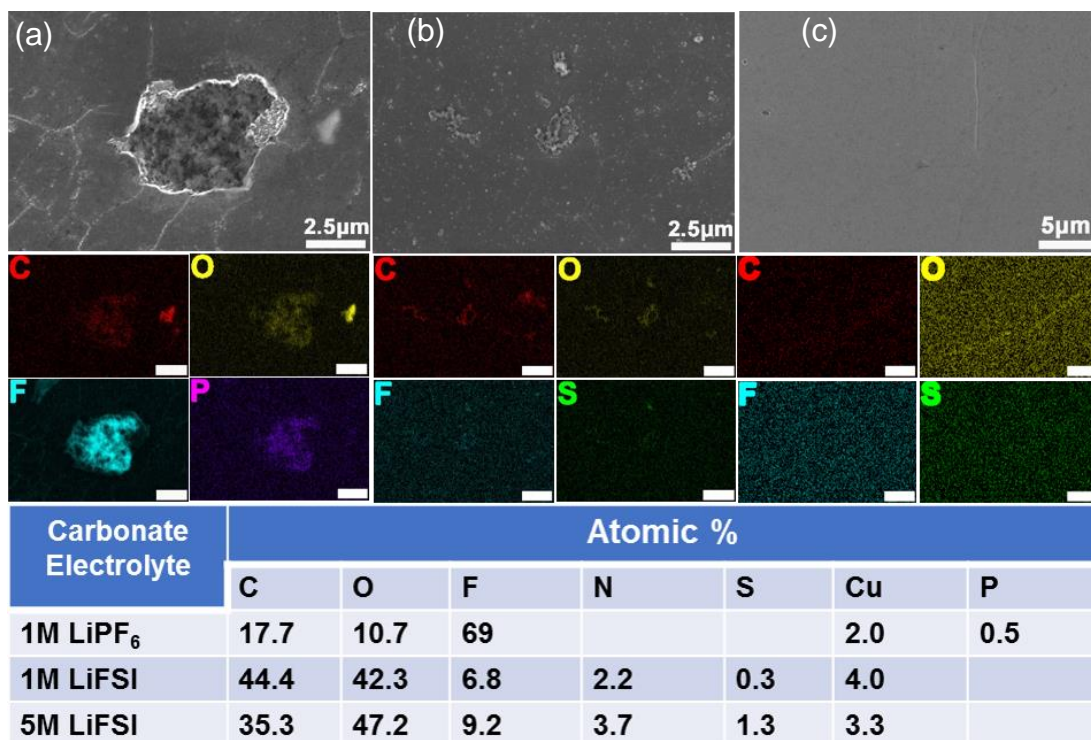


**Figure 2. 6** SEM images of the Li electrode surface, EDX elemental mapping (scale bar 2.5 μm), and elemental composition after 2 days soaking in electrolyte of (a) 1 M LiPF<sub>6</sub>, (b) 1 M LiFSI, and (c) 5 M LiFSI.

### 2.2.7 Average Coulombic Efficiency Measurement

CR 2016 type coin cells were used to measure the average coulombic efficiency: a lab-made 50 μm Li foil was first weighed and then pressed to the Cu substrate as the working electrode. Another identically made Li electrode was used as the counter electrode without weighing. Galvanostatic stripping was first applied to the working electrode, followed by deposition to complete one cycle. After a set number of cycles, any remaining Li on the working electrode was completely stripped using a 0.5 mA cm<sup>-2</sup> current until the stripping cutoff potential (1 V) was reached. The average CE can be calculated from the following equation:<sup>2</sup>

$$CE_{\text{Average}} = \frac{(T_s \times J + n \times C_c) \times A}{m_{\text{Li}} \times 3.86 + n \times C_c \times A}$$

where  $n$  is the cycle number;  $C_c$  is the cycling capacity;  $T_s$  is the time of the complete stripping of the working electrolyte;  $J$  is the areal current for the complete stripping ( $0.5 \text{ mA cm}^{-2}$ ),  $A$  is the area for working electrode ( $1.266 \text{ cm}^2$ ), and  $m_{\text{Li}}$  is the original mass of the Li on the working electrode. 3.86 represents the theoretical capacity of Li at  $3.86 \text{ Ah g}^{-1}$ .

The above method was calibrated by directly stripping the Li from the pristine working electrode, and then using the equation above to calculate the CE, which should be 100%.

**Figure 2.7** shows the calibration curve (stripping the pristine working electrode with  $0.5 \text{ mA cm}^{-2}$  in 1M LiFSI salt). The calculated CE is 99.2% due to the consumption of Li by side reactions with the electrolytes.

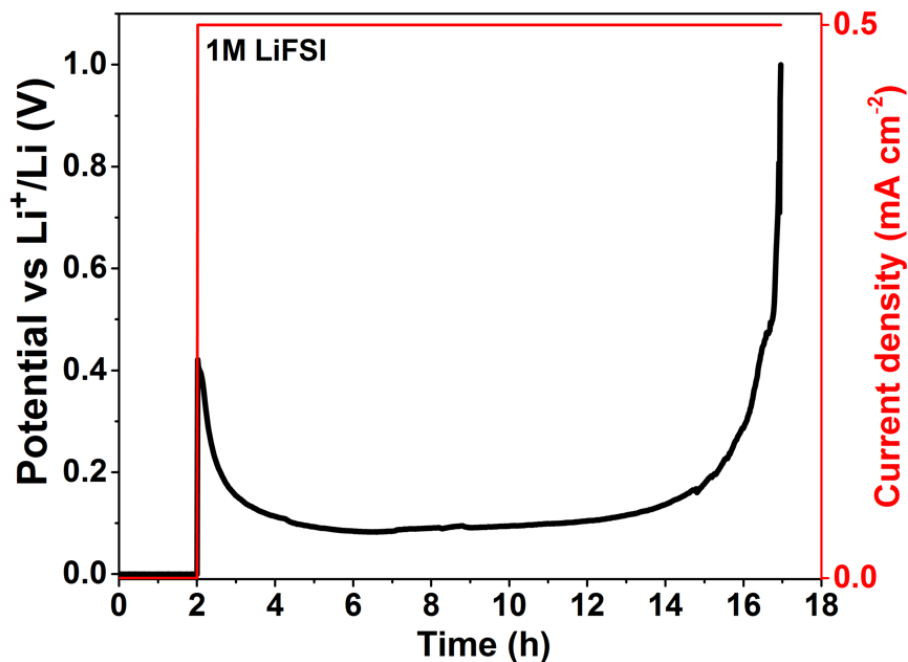


**Figure 2. 7** Calibration curve of columbic efficiency measurement. The inset is the digital image of the working electrode after Li was completely stripped from it.

### 2.2.8 EIS Measurement during GITT Li Deposition-Stripping

The GITT Li deposition-stripping was performed with a 10-minute current pulse ( $0.5\text{mA cm}^{-2}$ ) followed by a 2-hour rest until  $1\text{ mAh cm}^{-2}$  was achieved (i.e., total 12 pulses) as shown in the top panel in **Figure 2.16**. The EIS measurement was performed after rest for 1 hour over the frequency range from  $10^6$  to  $0.1\text{ Hz}$  with  $2\text{ mV}$  amplitude. Charge transfer resistance ( $R_{ct}$ ) was obtained by fitting the EIS results with an equivalent circuit.

### 2.2.9 XPS Characterizations

The Li electrodes were immersed in different electrolyte for 2 days prior to X-ray photoelectron spectroscopy (XPS) analysis. XPS data were collected using Kratos AXIS Supra (Al  $K\alpha=1486.7$  eV) at UC Irvine Materials Research Institute (IMRI). The samples were prepared following the same procedure for SEM samples. The samples were transported to the XPS facility inside a stainless steel tube with KF flange sealing filled with argon. Finally, the samples were loaded in the sample chamber in the glove box integrated with Kratos AXIS Supra for XPS analysis. All peaks of XPS data were calibrated with the reference peak of C 1s at 284.6 eV (the adventitious carbon).

### References

### 2.3 Results and discussion

Thin Li electrodes (50  $\mu\text{m}$ ) coated on a copper (Cu) current collector were produced in-house from bulk Li metal using a mechanical roller. The preparation details can be found in the **Figure 2.1**. **Figure 2.8a** shows the scanning electron microscopic (SEM) image of the cross-section of the Li electrode, illustrating the thickness measurement. The surface morphology of the Li electrode was characterized using SEM. The surface composition was analyzed using X-ray photoelectron spectroscopy (XPS) revealing Li, oxygen, and carbon content, the latter two of which can be traced to environmental exposure (**Figure 2.2**). Li||Li symmetric cells in 2016-type coin cells using Celgard 3501 separator were constructed for cycle life measurement. Three different electrolytes were used in the experiments: 1 M LiPF<sub>6</sub>, 1 M LiFSI, and 5 M LiFSI, each in a mixture of ethylene carbonate (EC) and diethyl carbonate (DEC) with a 1:1 volume ratio. The water content in all

electrolytes was less than 10 ppm, as measured by Karl Fischer titration. Precisely 30  $\mu\text{L}$  of electrolyte was used in each cell in our initial measurement. The end of cycle life is defined at the first sudden decrease of Li deposition-stripping overpotential during the cycling of Li||Li symmetric cells, which is consistent with existing reports.<sup>37</sup> **Figure 2.8b** displays a typical Li||Li cell cycling with 0.5 mA  $\text{cm}^{-2}$  current and 1 mAh  $\text{cm}^{-2}$  capacity: the deposition-stripping overpotential continues to increase during cycling until the sudden drop at the 130<sup>th</sup> cycle.

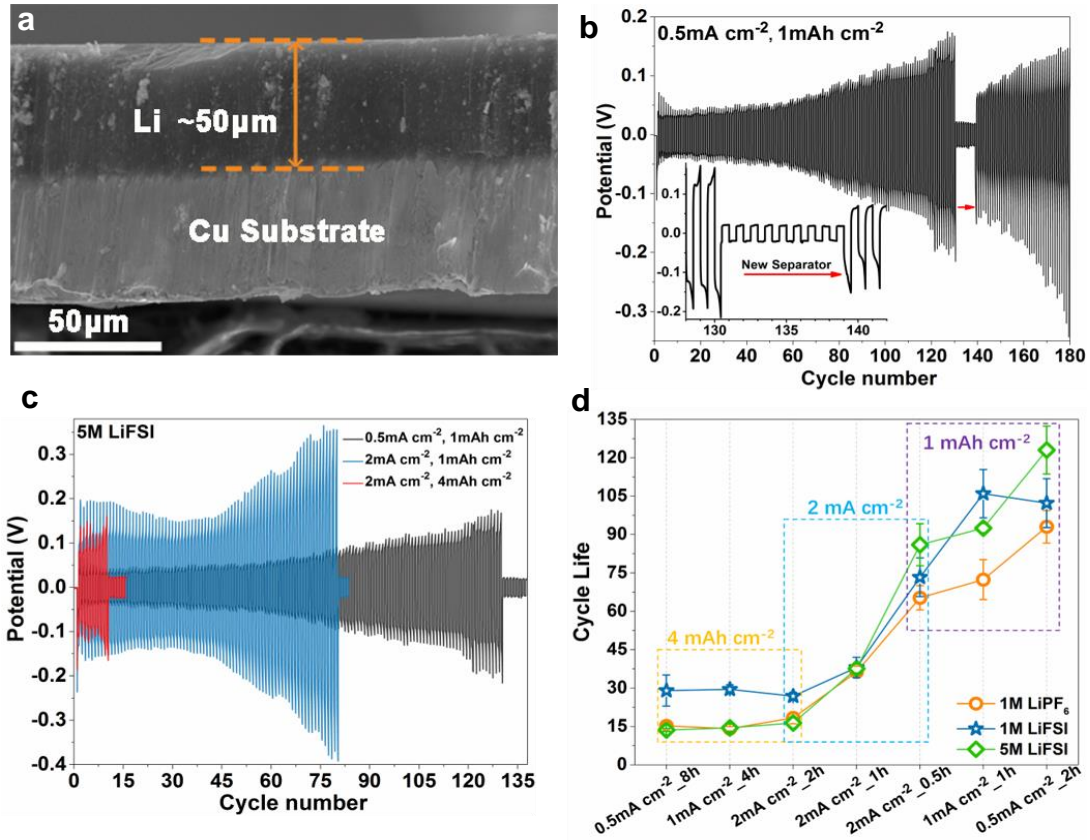


**Figure 2. 8** (a) SEM image of the cross-section of the thin Li electrode on Cu substrate; (b) cycling curve of a Li||Li symmetric cell in 5M LiFSI electrolyte showing internal short and continuous cycling after replacing the separator; (c) representative cycling curves and (d) cycle lives of the Li||Li symmetric cells using different electrolytes and different cycling parameters.

The increasing overpotential is mainly due to the stripping of Li from the bulk Li through the dead Li and continuously deteriorating interphase,<sup>38-40</sup> an explanation confirmed by our experiments in three-electrode cells with the galvanostatic intermittent titration technique (GITT, **Figure 2.9**). **Figure 2.9a** shows the GITT experiment with  $0.5 \text{ mA cm}^{-2}$  current and  $1 \text{ mAh cm}^{-2}$  capacity; **Figure 2.9b** shows the GITT experiment with  $2 \text{ mA cm}^{-2}$  current and  $4 \text{ mAh cm}^{-2}$  capacity. From the three-electrode cycling and GITT data, the first deposition process initially shows a spike of overpotential, which is clearly due to the deposition of Li on the passivated pristine Li surface. However, the initial stripping overpotential is low, which indicates that the Li stripping starts from the deposited Li, which has porous structure causing low overpotential. Towards the end of the stripping step, the overpotential rapidly rises up, which is due to the stripping of Li from the bulk Li. This observation also indicates that the coulombic efficiency of the deposition-stripping is less than 100%; a portion of deposited Li is not accessible to be stripped due to electrolyte decomposition and dead Li formation. The overpotential of the two-electrode cells is consistent with the superposition of the overpotential from both of the electrodes (i.e. deposition overpotential plus stripping overpotential). The overpotential continues increasing during cycling, and it is clear from the three-electrode cycling data between the 21<sup>st</sup> cycle and the 61<sup>st</sup> cycle in **Figure 2.9** that the increase is mainly from the overpotential of Li stripping. This is due to the increasingly bulk of the Li and increased concentration polarization.

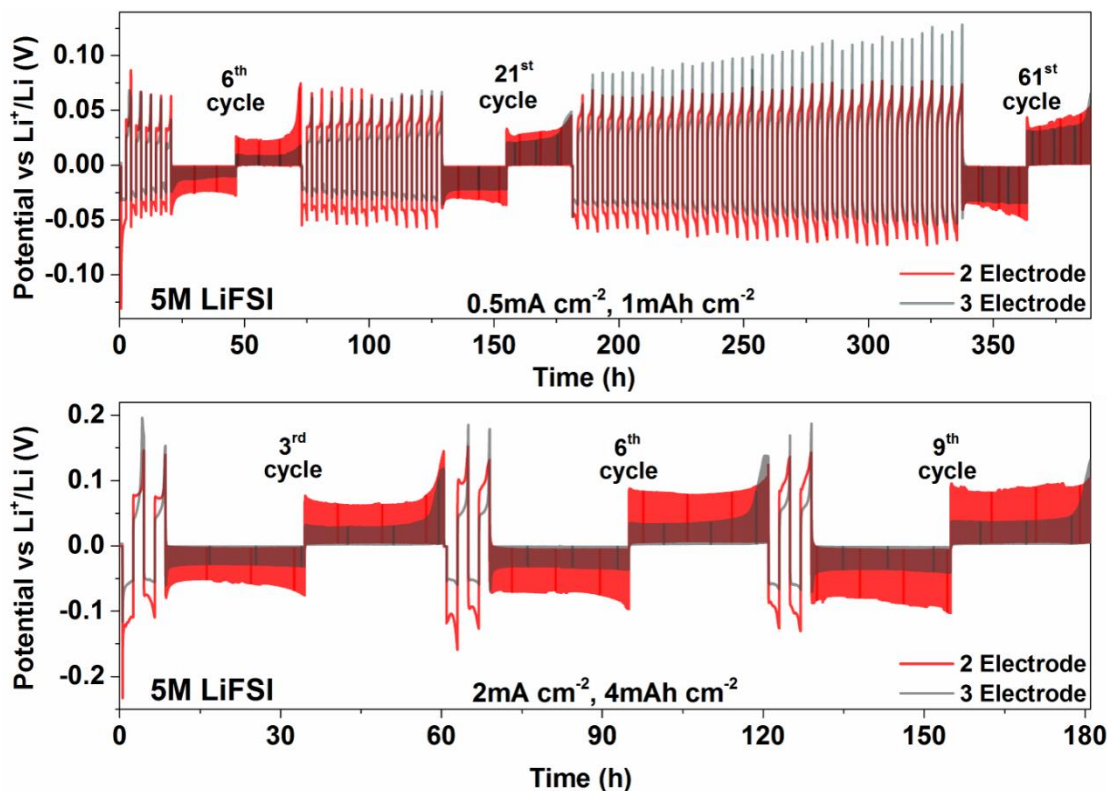


**Figure 2.9** Constant-current Li plating-stripping cycling with intermittent GITT measurement with (top)  $0.5 \text{ mA cm}^{-2}$  and  $1 \text{ mAh cm}^{-2}$  and (bottom)  $2 \text{ mA cm}^{-2}$  and  $4 \text{ mAh cm}^{-2}$  in the 5 M LiFSI electrolyte.

The sudden drop in overpotential reflects an instant decrease of impedance caused by the internal short of the Li||Li cell. The impedance change, measured with electrochemical impedance spectroscopy (EIS, **Figure 2.10**), clearly demonstrates a drastic decrease of charge transfer resistance after the overpotential drop.

**Figures 2.10a** and **2.10b** are the galvanostatic cycling of two Li||Li symmetric cells under the same condition ( $2 \text{ mA cm}^{-2}$  and  $4 \text{ mAh cm}^{-2}$ ). Cell #1 was still in good condition after 11 cycles, while a sudden potential drop occurred during the 10<sup>th</sup> cycle in Cell #2. The corresponding EIS measurement results reveal the change of impedance in the two cells as shown in **Figures 2.10c** and **2.10d**: in Cell #1, the electrolyte resistance is constant

throughout the 11 cycles. The charge transfer resistance significantly decreases after the 1<sup>st</sup> cycle during the increased interface surface area. More importantly, the internal resistance between the 6<sup>th</sup> and 11<sup>th</sup> cycles remains very consistent. On the other hand, in Cell #2, the internal resistances between the 6<sup>th</sup> cycle and the 11<sup>th</sup> cycle, immediately after the sudden potential drop, are distinctly different. The electrolyte resistance decreases from ~13 to ~8 ohm, and more significantly, the charge transfer resistance is also reduced from ~30 ohm to 9 ohm. Both observations indicate a short-short between two SEI coated Li electrodes.

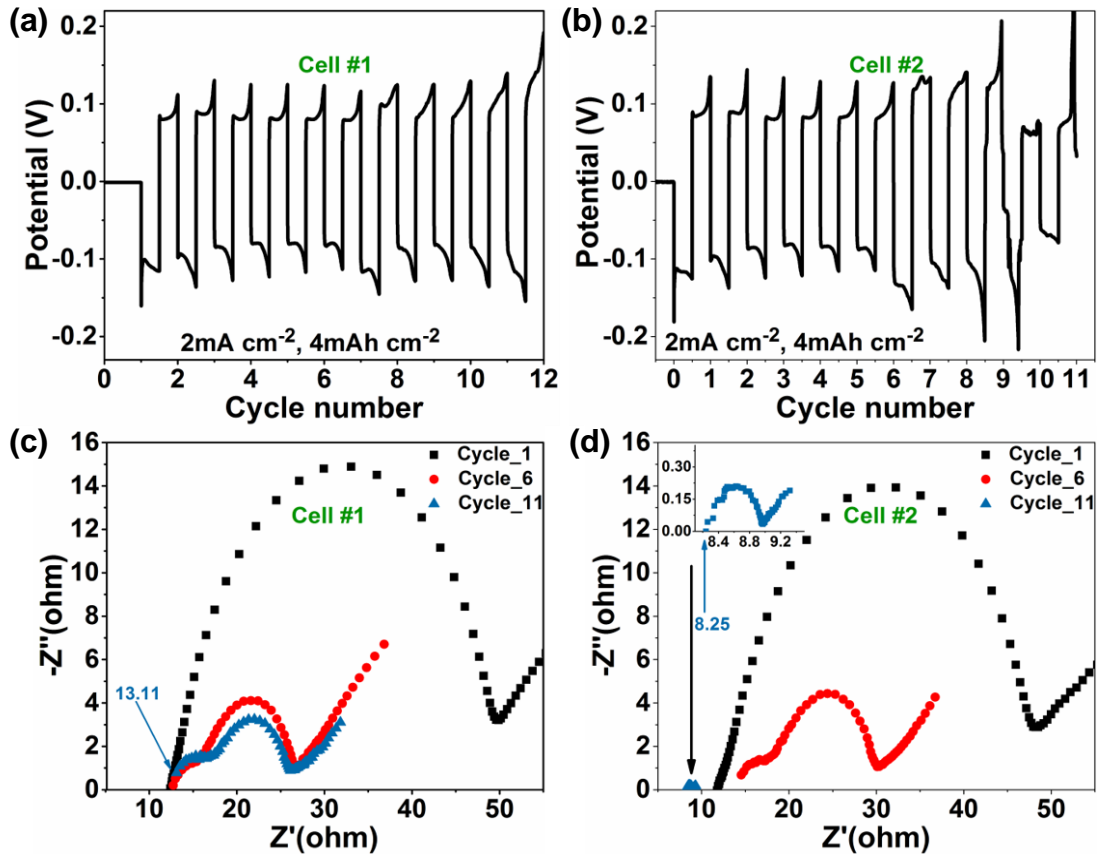


**Figure 2. 10** (a-b) Galvanostatic Li deposition-stripping curves and (c-d) EIS Nyquist plots of the symmetric Li||Li cells after certain cycles.

It is also worth noting that the overpotential does not drop to zero, which would occur in the case of pure metal-metal contact. Therefore, we refer to this type of internal short as a soft-short,<sup>34</sup> which is caused by the contact of Li covered by the solid electrolyte interphase (SEI) layer through a breach of the separator. As evidence, the separator in the cell used in Figure 1b was replaced and the cell was subjected to continuous cycling. It is clear from this experiment that normal Li deposition-stripping can be resumed. Further evidence of soft-short is described in **Figures 2.4** and **2.5**.

The symmetric Li||Li cells were cycled in all three electrolytes with a range of areal capacity from 1 to 4 mAh cm<sup>-2</sup> and areal current from 0.5 to 2 mA cm<sup>-2</sup>. **Figure 2.8c** shows the representative cycling curves under various capacity and current combinations in 5 M LiFSI electrolyte. Clearly both areal current and areal capacity strongly affect the cycle life: the higher the current and capacity are, the shorter the cycle life becomes. (This statement is valid when adequate electrolyte is used in the cell. However, when under a low electrolyte/capacity ratio, the cycle life seems to have much weaker correlation to the areal capacity as shown in Figure 2.) Particularly, the Li||Li cells last fewer than 20 cycles with 4 mAh cm<sup>-2</sup> areal capacity and 2 mA cm<sup>-2</sup> areal current. The correlation between cycle life and cycling parameters in all three electrolytes is summarized in **Figure 2.8d**, in which all data points were averaged from at least five repeated experiments. The first observation is that the cycle life (i.e., soft-short) has no strong correlation with the type and concentration of Li salt, although 1 M LiFSI electrolyte shows slight advantage under high areal capacity at 4 mAh cm<sup>-2</sup>. On the other hand, cycle life shows strong correlation with the areal capacity (depth of deposition-stripping): at a high capacity of 4 mAh cm<sup>-2</sup>, the cycle life is generally

short and seems unaffected by the areal current (rate of deposition-stripping). At a constant areal current at  $2 \text{ mA cm}^{-2}$ , the cycle life clearly increases with decreased areal capacity. When the areal capacity is kept as low as  $1 \text{ mAh cm}^{-2}$ , areal current appears to affect cycle life to a certain extent, as the longest cycle lives are found at the lowest current at  $0.5 \text{ mA cm}^{-2}$ . These results unambiguously demonstrate the necessity of using realistic parameters to measure the cycle life of Li||Li symmetric cells when using liquid electrolytes or electrolytes with liquid components.

The results above were obtained with a fixed  $30 \text{ }\mu\text{L}$  electrolyte, which translates to electrolyte/capacity ratios of 5, 12, and  $24 \text{ mL Ah}^{-1}$  at 4, 2, and  $1 \text{ mAh cm}^{-2}$ , respectively (the surface area of the Li electrode is  $1.266 \text{ cm}^2$ ). We found that the electrolyte/capacity ratio can profoundly affect the cycle life of the Li||Li symmetric cells. **Figure 2.11a** displays the representative cycling curves in  $5 \text{ M LiFSI}$  electrolyte with  $1 \text{ mAh cm}^{-2}$  areal capacity using three electrolyte/capacity ratios:  $47 \text{ mL Ah}^{-1}$  ( $60 \text{ }\mu\text{L}$ ),  $24 \text{ mL Ah}^{-1}$  ( $30 \text{ }\mu\text{L}$ ), and  $8 \text{ mL Ah}^{-1}$  ( $10 \text{ }\mu\text{L}$ ). The cycle life of the Li electrode clearly decreases with decreased electrolyte/capacity ratio. To obtain a comprehensive understanding on the effects of the electrolyte/capacity ratio, we remeasured the cycle life of the Li||Li cells using  $1 \text{ M LiPF}_6$  and  $5 \text{ M LiFSI}$  electrolytes, with a constant electrolyte/capacity ratio at  $6 \text{ mL Ah}^{-1}$  for comparison to the observations made with constant electrolyte volume of  $30 \text{ }\mu\text{L}$  as displayed in **Figure 2.11b** and **2.11c**. It is interesting to see that the cycle life of Li electrode seems to be independent of areal capacity with the  $6 \text{ mL Ah}^{-1}$  electrolyte/capacity ratio. This observation indicates that with adequate electrolyte, the cycle life of Li||Li symmetric cells (where soft-short occurs) is correlated with the depth of Li deposition-stripping (areal

capacity). However, the electrolyte/capacity ratio dictates cycle life when the amount of electrolyte is limited.

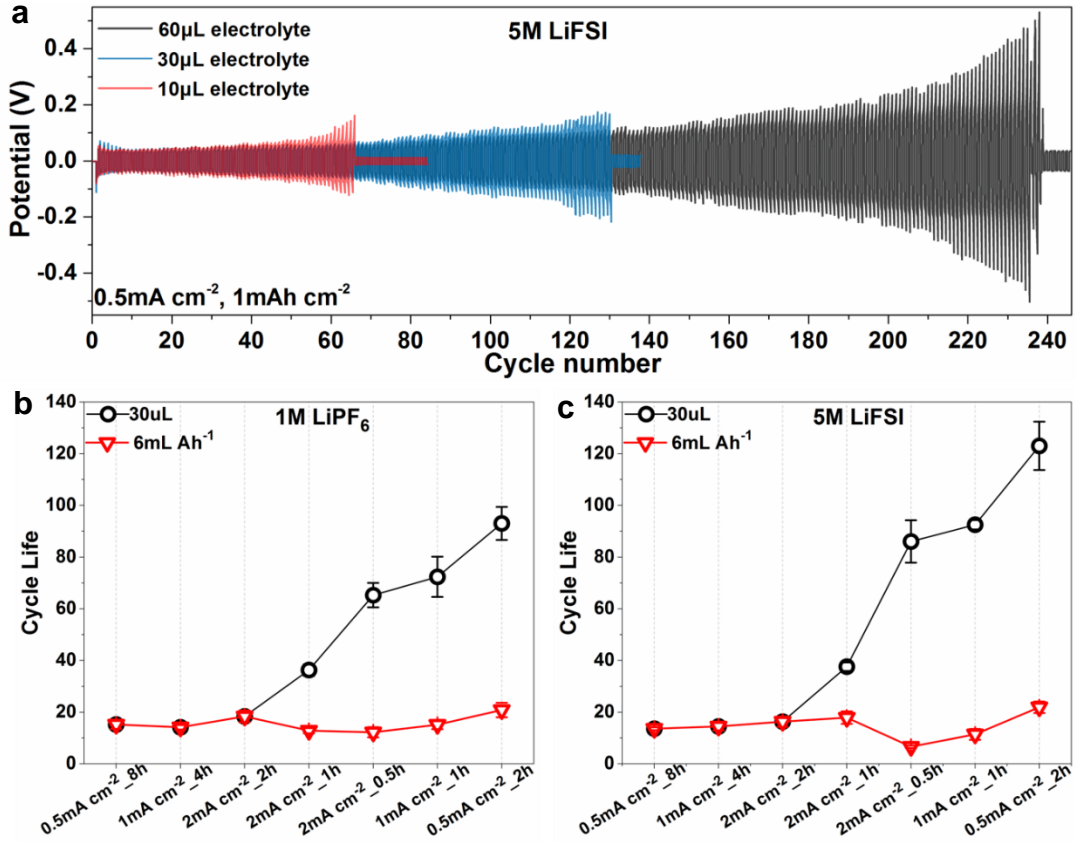


**Figure 2. 11** Effect of electrolyte/capacity ratio on the cycle life of Li||Li symmetric cells. (a) Representative cycling curves of Li||Li symmetric cells in 5 M LiFSI electrolyte using different electrolyte/capacity ratio. Cycle lives of Li||Li symmetric cells in (b) 1 M LiPF<sub>6</sub> and (c) 5 M LiFSI electrolytes under fixed amount of electrolyte versus fixed electrolyte/capacity ratio.

To probe the direct cause of soft-short and its correlation to the electrolyte/capacity ratio, the deposited Li in 5 M LiFSI electrolyte was characterized using SEM after different cycles using  $1\text{ mAh cm}^{-2}$  capacity and  $4\text{ mAh cm}^{-2}$  capacity at 0.5 C (giving a current of  $0.5\text{ mA cm}^{-2}$  and  $2\text{ mA cm}^{-2}$ , respectively). The SEM characterization confirms the porous structure of the deposited Li layer. Furthermore, it reveals that the thickness of the

deposited Li is much higher than the theoretic values as displayed in **Figures 2.12a** and **2.12b**. At the 10<sup>th</sup> cycle, the thickness of the deposited Li under 1 mAh cm<sup>-2</sup> and 4 mAh cm<sup>-2</sup> is approximately 27 μm and 140 μm while the theoretical thicknesses at those capacities are 5 μm and 20 μm, respectively. As **Figure 2.12c** shows, the thickness of the deposited Li layer in the first cycle is negatively correlated with the corresponding cycle life under all cycling parameters. This evidences that the drastic volume change of the Li electrode during cycling and the resultant mechanical strain on the separator is the cause of the separator breaching and the cell soft-shortening.

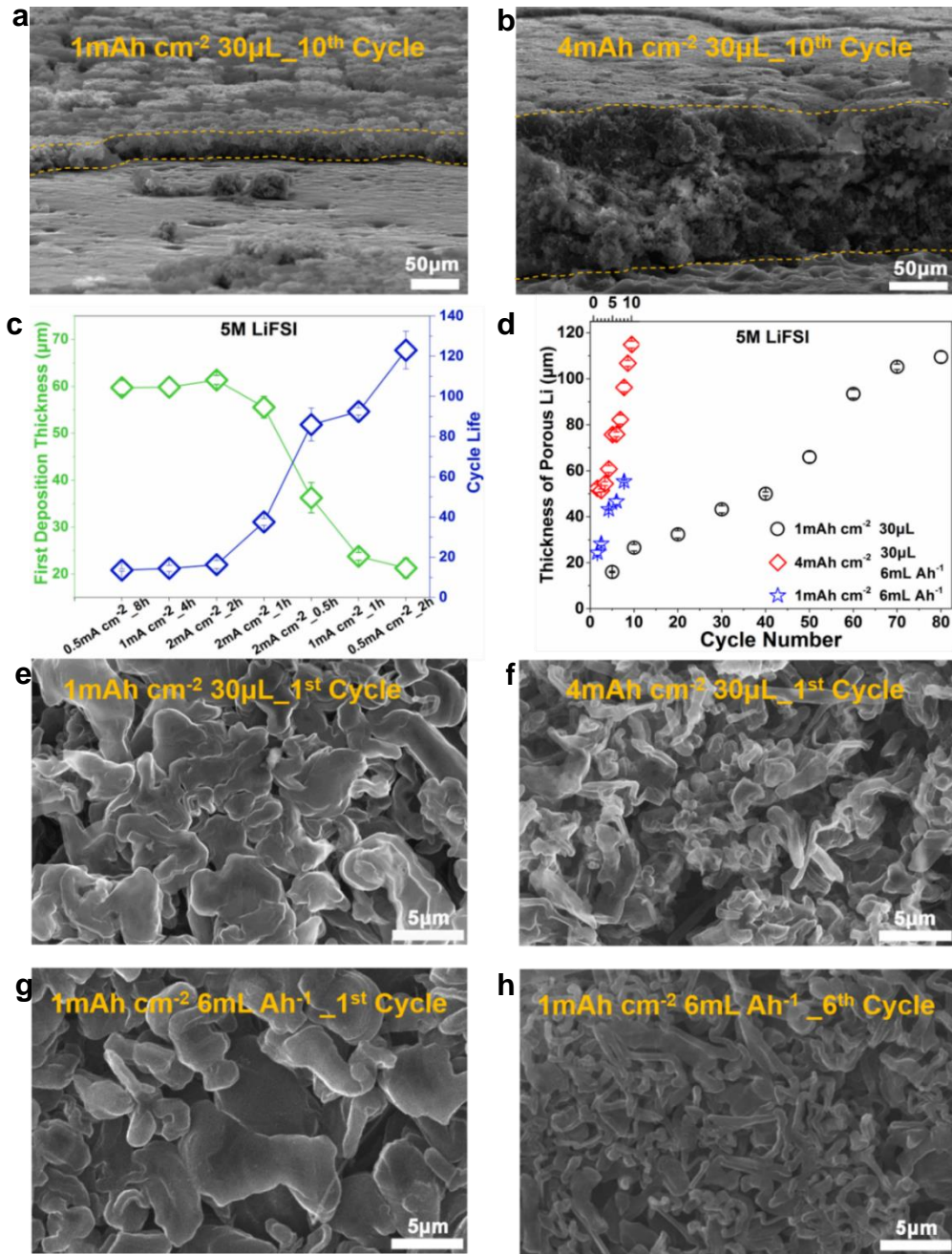


**Figure 2.** 12 SEM images illustrating the thickness of the deposited Li after 10 cycles under (a)  $1\text{mA cm}^{-2}$  and (b)  $4\text{mA cm}^{-2}$  at  $0.5\text{ C}$  using  $30\mu\text{L}$   $5\text{ M LiFSI}$  electrolyte. (c) Relationship between thickness of the 1st Li deposition and cycle life in  $5\text{ M LiFSI}$  electrolyte with different cycling parameters. (d) The thickness of deposited Li as the function of cycle number in  $5\text{ M LiFSI}$  electrolyte. (e-h) Representative SEM images of deposited Li in  $5\text{ M LiFSI}$  electrolyte.

This conclusion is reinforced by the observation that the thickness of the deposited Li layer continues increasing during cycling. The SEM images illustrating the increase of thickness are in **Figures 2.13** and **2.14**.

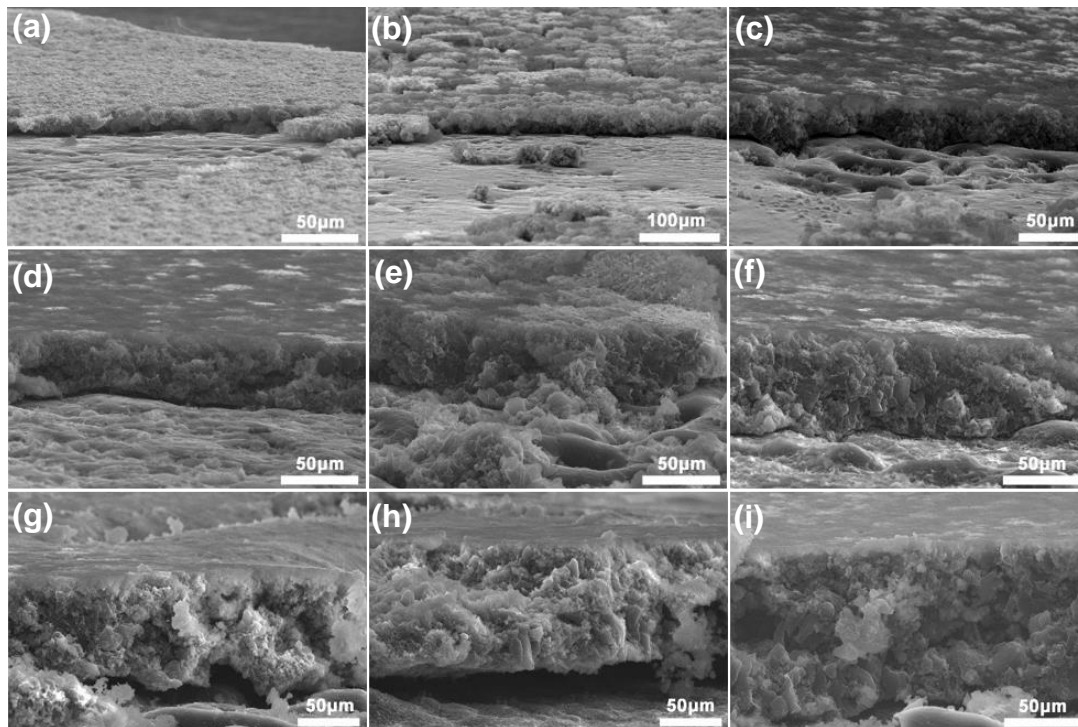


**Figure 2. 13** SEM images of the thickness measurement of the deposited Li layer in 5 M LiFSI electrolyte after (a) 5 cycles, (b) 10 cycles, (c) 20 cycles, (d) 30 cycles, (e) 40 cycles, (f) 50 cycles, (g) 60 cycles, (h) 70 cycles, and (i) 80 cycles. The areal current density is  $0.5 \text{ mA cm}^{-2}$  and the areal capacity is  $1 \text{ mAh cm}^{-2}$ .

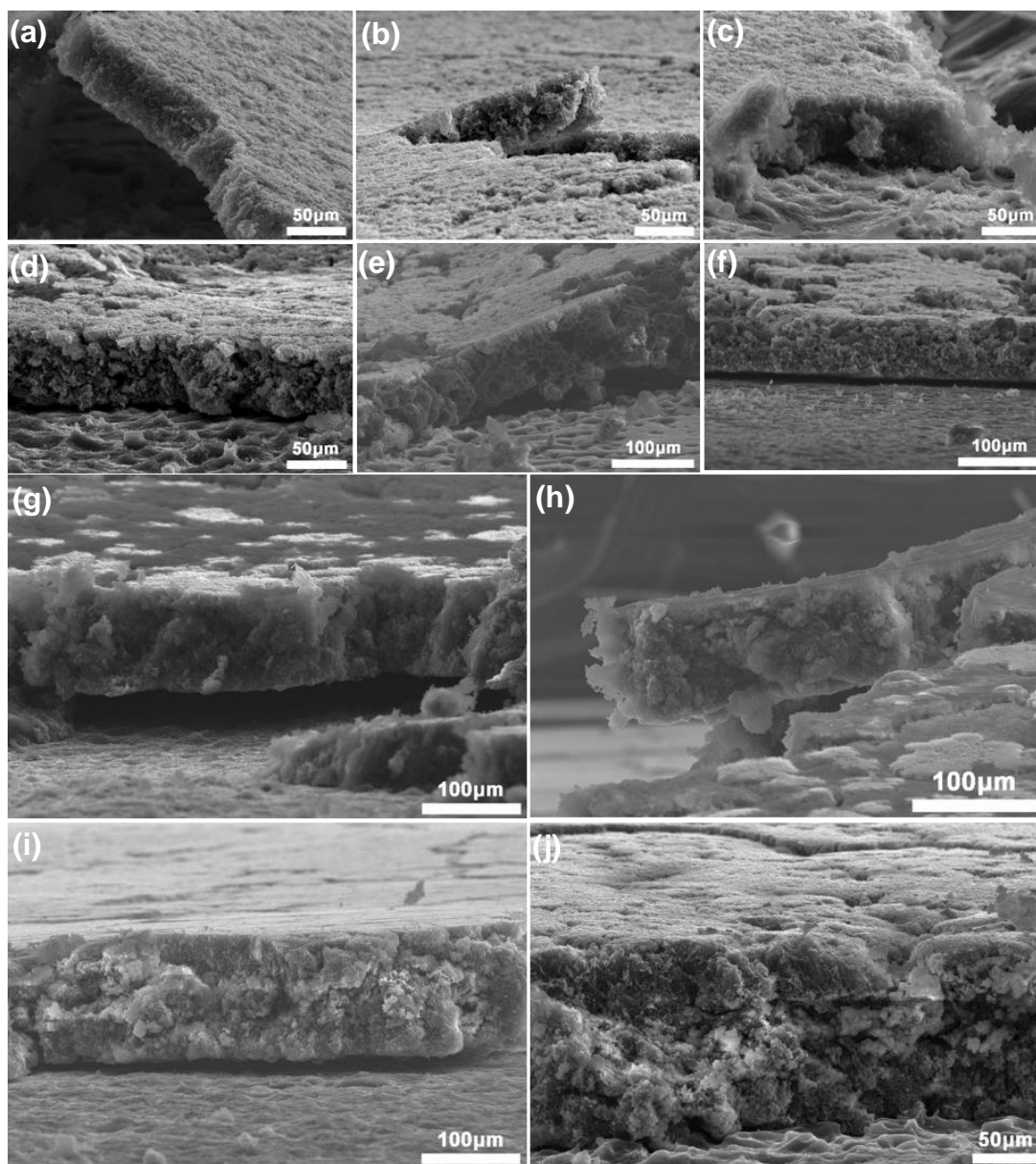


**Figure 2.14** SEM images of the thickness measurement of the deposited Li layer in 5 M LiFSI electrolyte after (a) 1 cycle, (b) 2 cycles, (c) 3 cycles, (d) 4 cycles, (e) 5 cycles, (f) 6 cycles, (g) 7 cycles, (h) 8 cycles, (i) 9 cycles, and (j) 10 cycles. The areal current is  $2 \text{ mA cm}^{-2}$ , and the areal capacity is  $4 \text{ mAh cm}^{-2}$ .

**Figure 2.12d** plots the thickness of the deposited Li layer as the function of cycle number under  $4 \text{ mAh cm}^{-2}$  and  $1 \text{ mAh cm}^{-2}$  areal capacity using either fixed  $30 \text{ } \mu\text{L}$  electrolyte or  $6 \text{ mL Ah}^{-1}$  electrolyte/capacity ratio ( $4 \text{ mAh cm}^{-2}$  with  $30 \text{ } \mu\text{L}$  electrolyte fulfills both

conditions). One can observe that the thickness of deposited Li under 4 mAh cm<sup>-2</sup> and 1 mAh cm<sup>-2</sup> areal capacity (red diamonds versus blue stars in Figure 3d) undergoes a similar growth rate given the same electrolyte/capacity ratio at 6 mL Ah<sup>-1</sup>. Meanwhile, the comparison between the thickness growth under 1 mAh cm<sup>-2</sup> with 30 μL electrolyte (24 mL Ah<sup>-1</sup>) and 6 mL Ah<sup>-1</sup> electrolyte/capacity ratio (blue stars versus black circles in Figure 3d) clearly demonstrates that an adequate amount of electrolyte leads to much slower growth rates under the same areal capacity. The top-view SEM images in **Figures 2.12e-2.12h** show that both in-depth deposition and low electrolyte/capacity ratio result in more porous deposition of Li (Figures 3e and 3f), and that the Li deposition becomes more and more porous as cycling continues, which is consistent with the observed increase of thickness (Figures 3g and 3h). Overall, these results can complement the conventional understanding of Li dendrite formation and its contribution to internal shorting. The classically defined dendrite structure was not observed under any conditions in our study; Instead, we observed drastic volumetric expansion of the Li electrode due to the porous deposition of Li and continuous side reactions, which include the chemical and electrochemical reductions of EC/DEC solvents and the PF<sub>6</sub><sup>-</sup>/FSI<sup>-</sup> anions. Therefore, we can conclude that repeated and increasing mechanical strain on the separator imposed by the growing volume of the Li electrode ultimately results in the breach of said separator and subsequent internal shorting of the battery.

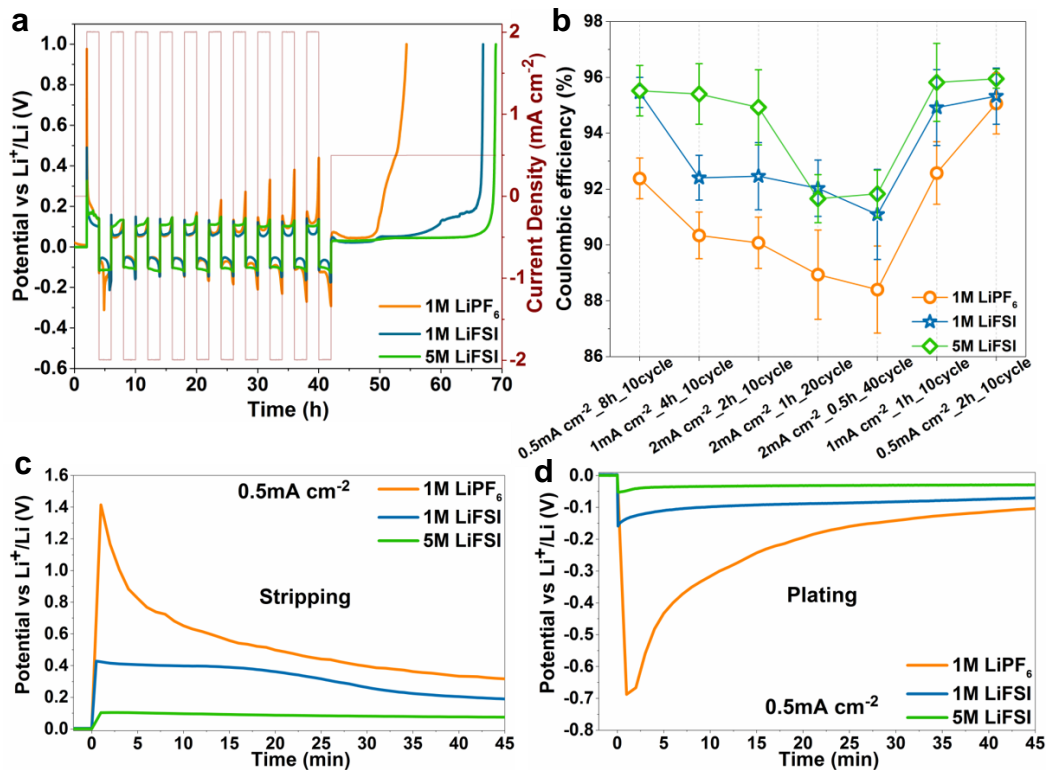


**Figure 2.15** (a) The representative voltage and current profiles in the measurement of average coulombic efficiency. (b) Average coulombic efficiency of Li deposition-stripping in different electrolytes under different cycling parameters. Electrochemical potential of galvanostatic (c) stripping and (d) deposition of Li.

Coulombic efficiency (CE) is another important parameter of a Li metal anode, since it is a strong indicator of the interfacial stability. In this study we measured the average CE based on an established method<sup>41</sup> with slight modifications as detailed in the Supporting Information. Briefly, a thin layer of Li with known mass (i.e. total capacity) mechanically coated on a Cu substrate was used as the measured electrode instead of Li electrochemically deposited on Cu to improve the accuracy of the average CE. **Figure 2.15a** displays a typical applied current protocol and the potential response to calculate the average CE over 10 cycles. The average CE under various cycling parameters in all three electrolytes are shown in **Figure 2.15b**. The most striking observation is that the LiFSI electrolytes are superior

to the  $\text{LiPF}_6$  electrolyte in terms of CE regardless of cycling condition, and that the 5 M LiFSI electrolyte is better than the 1 M. It also clearly demonstrates that the average CE is closely related to the measurement conditions: in general, higher accumulated capacity (capacity multiplying cycle number) results in lower CE. Given the same accumulated capacity, a higher cycle number and/or a higher cycling current (rate) results in lower average CE.

As stated above, CE is an indicator of the Li/electrolyte interfacial stability, which is reflected in the overpotential of Li deposition and stripping. **Figure 2.15c** and **2.15d** show the potential profiles of galvanostatic stripping and deposition of Li in three-electrode cells using  $0.5 \text{ mA cm}^{-2}$  areal current. The 5 M LiFSI electrolyte demonstrates the lowest stripping and deposition overpotential, followed by 1 M LiFSI. The 1 M  $\text{LiPF}_6$  electrolyte delivers the highest overpotential for both stripping and deposition with large overshoot. The EIS measurement during the GITT Li deposition-stripping process demonstrates the charge transfer resistance in the three electrolytes in the consistent order:  $R_{5\text{M LiFSI}} < R_{1\text{M LiFSI}} < R_{1\text{M LiPF}_6}$  (**Figure 2.16**). During the Li deposition, the  $R_{\text{ct}}$  shows the following trend:  $R_{\text{ct}}(1\text{M LiPF}_6) > R_{\text{ct}}(1\text{M LiFSI}) > R_{\text{ct}}(5\text{M LiFSI})$  as shown in the bottom panel in **Figure 2.16**. Furthermore, the  $R_{\text{ct}}$  in 1 M  $\text{LiPF}_6$  is much higher than those in the LiFSI electrolytes. During the Li stripping, the initial  $R_{\text{ct}}$  in all three electrolytes are similar, which is consistent with the fact that Li is first stripped from the previously deposited. Nearing the middle of the stripping process, the  $R_{\text{ct}}$  in 1 M  $\text{LiPF}_6$  is the first to increase, followed by 1 M LiFSI. The  $R_{\text{ct}}$  in 5 M LiFSI only moderately increases during the Li stripping. The rising  $R_{\text{ct}}$  during Li stripping is consistent with the rising overpotential, which is mainly

due to the stripping bulk Li. Therefore, this observation indicates the worst CE in 1 M  $\text{LiPF}_6$  (i.e., first to reach stripping bulk Li with the highest  $R_{ct}$ ), followed by 1 M LiFSI and then 5 M LiFSI.

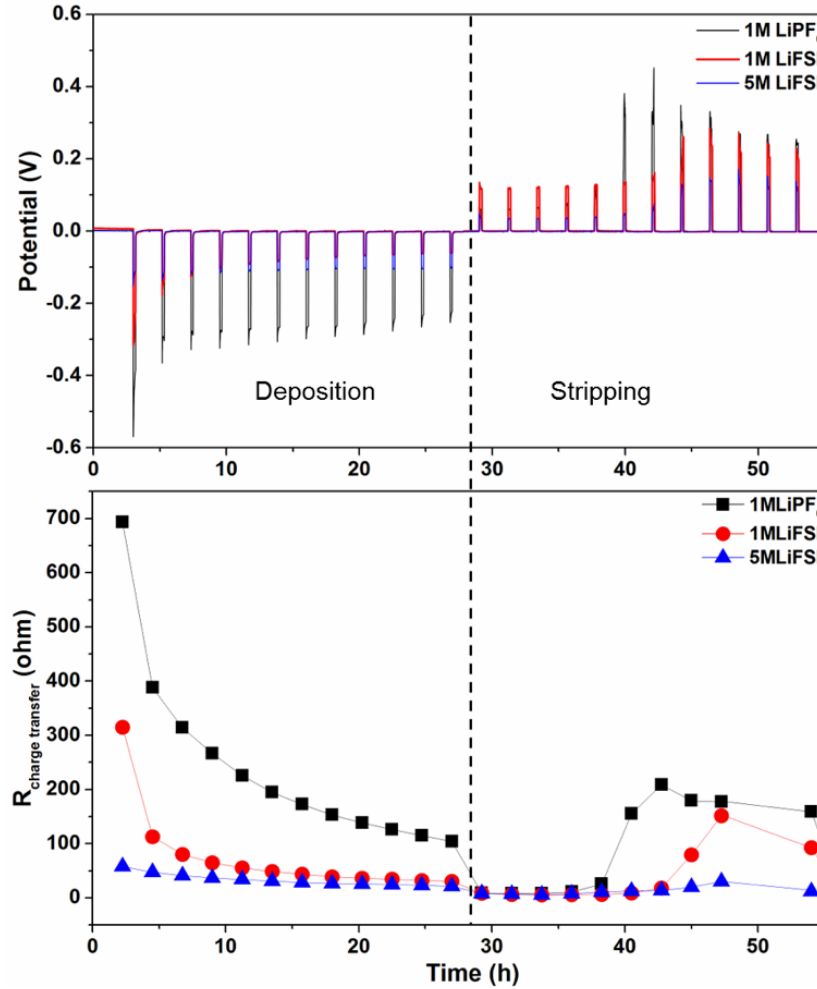


**Figure 2. 16** (Top) GITT Li deposition-stripping curves in Li||Li symmetric cells in three electrolytes and (bottom) the corresponding charge transfer resistance change.

These Li working electrodes were produced using identical processes. Therefore, the different overpotentials and charge transfer resistances clearly originate from the passivation layer on the Li electrode formed by contact with the electrolyte.

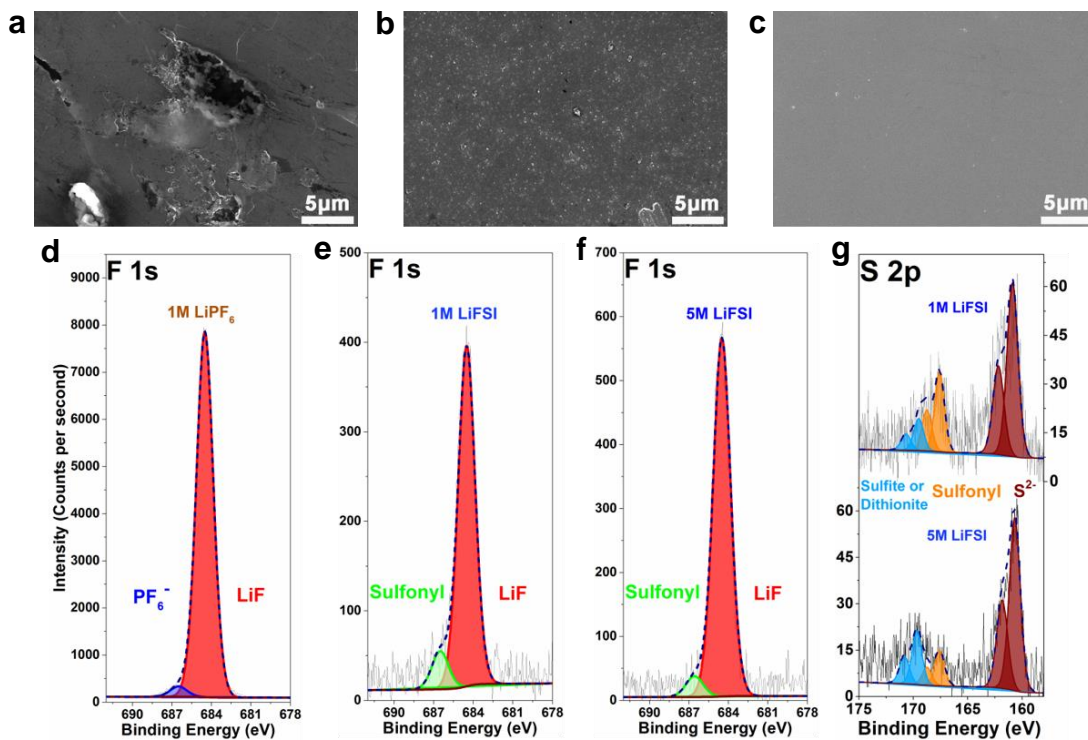


**Figure 2.17** Chemical stability of Li electrode in different electrolytes: SEM images of Li electrode surface after soaking in (a) 1 M LiPF<sub>6</sub>, (b) 1 M LiFSI, and (c) 5 M LiFSI electrolyte; XPS F 1s spectra of Li electrodes surface after soaking in (d) 1 M LiPF<sub>6</sub>, (e) 1 M LiFSI, and (f) 5 M LiFSI; (g) XPS S 2p spectra of Li electrodes surface after soaking in the LiFSI electrolytes.

**Figures 2.17a to 2.17c** display representative SEM images of the Li electrode surface after immersion in 1 M LiPF<sub>6</sub>, 1 M LiFSI, and 5 M LiFSI electrolytes for two days. And the corresponding EDS analysis result can be found in **Figure 2.6**. Clearly, the Li surface in 1 M LiPF<sub>6</sub> is severely pitted; the extent of pitting in the 1 M LiFSI is much less severe, while the Li surface in 5 M LiFSI does not show any indication of pitting. The elemental analysis via energy dispersive X-ray spectroscopy reveals that besides Li, the Li surface layer also contains carbon, oxygen, fluorine, phosphorus (in LiPF<sub>6</sub> electrolyte), and sulfur (in LiFSI electrolytes) elements (details found in the Supporting Information). **Figures 2.17d to 2.17f** are XPS F 1s spectra of the passivation layer formed in the three electrolytes. The Li surface in 1 M LiPF<sub>6</sub> has substantial fluoride content that can be attributed to lithium

fluoride (LiF), which is produced from the decomposition of  $\text{PF}_6^-$  anion.<sup>42</sup> We also believe that the presence of trace amounts of water in the electrolyte additionally intensifies the formation of LiF via the reactions between HF and potential surface species, including Li oxide, hydroxide, and carbonate. On the other hand, the intensity of LiF content on the Li surface in the LiFSI electrolytes, formed from the chemical reduction of FSI anion by Li metal,<sup>43,44</sup> is lower by more than one order of magnitude. The XPS S 2p spectra in **Figure 2.17g** reveal the sulfur-containing species on the Li surface in the two LiFSI electrolytes. The S 2p peaks at 167.8 eV (S 2p<sub>3/2</sub>) represent the sulfonyl residue of the FSI anion, and the S 2p peaks at the higher binding energy of 169.7 eV (S 2p<sub>3/2</sub>) can be attributed to the sulfite ( $\text{SO}_3^{2-}$ ) and/or dithionite ( $\text{S}_2\text{O}_4^{2-}$ ) groups from the chemical reduction of FSI anion by Li metal.<sup>42,45</sup> Still, the most prominent peaks are the ones at 160.7 eV (S 2p<sub>3/2</sub>) attributed to Li sulfide ( $\text{Li}_2\text{S}$ ),<sup>46,47</sup> which also originate from the chemical reduction of FSI anion.<sup>43-45</sup> The overall Li surface composition analysis from XPS can be found in the Supporting Information. The XPS results clearly indicate that the high overpotential of deposition and stripping of Li in 1 M  $\text{LiPF}_6$  electrolyte is due to the passivating LiF content on the surface, which also contributes to the lower CE. On the other hand, lower LiF content on the Li surface in the LiFSI electrolytes results in lower overpotential. The quantitative analysis of the sulfide content in the Li surface layer (**Figure 2.18**) in the LiFSI electrolytes seems consistent with the relative magnitude of the deposition-stripping overpotential.

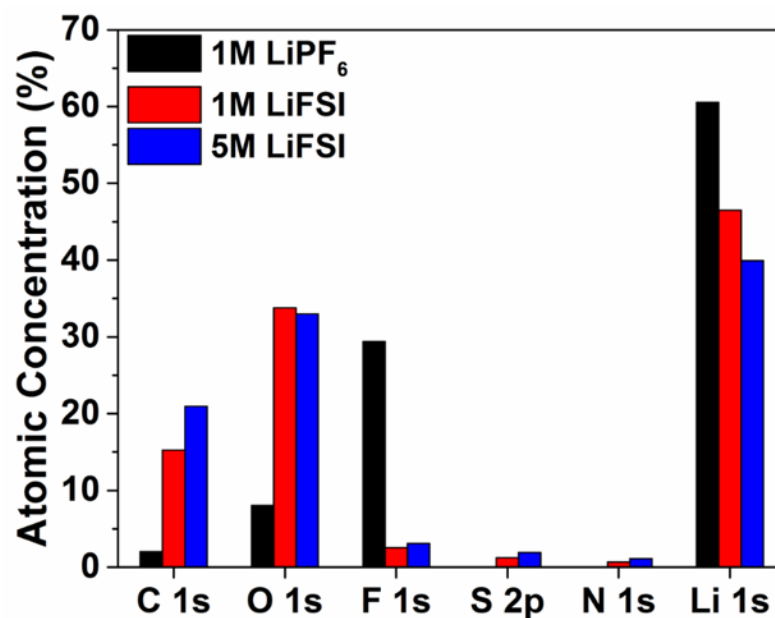


**Figure 2. 18** Atomic concentration of Li electrode surface after soaking in different electrolyte for 2 days from XPS analysis.

Given the combination of average CE measurement, Li deposition-stripping overpotential, and the surface SEM and XPS analyses, it is unambiguous that high-concentration LiFSI electrolyte improves Li/electrolyte interface stability, which is consistent with the previous findings,<sup>6-8,10</sup> although its effect to the improvement of cycle life (particularly under high areal capacity) is not distinct.

## 2.4 Conclusions

In this study, we examined the cycle life of thin Li electrode in carbonate electrolytes under the effects of varied areal capacity, current, type and concentration of Li salt, and the electrolyte/capacity ratio. The failure mechanism of the Li||Li symmetric cell was determined to be soft-shortening induced by the continuous Li volume expansion due to porous deposition. The rate of Li electrode volume expansion is correlated with the electrolyte/capacity ratio; the porous Li deposition grows faster under leaner electrolyte conditions. With limited electrolyte, the cycle life of a thin Li electrode is dictated by the cycling parameter, showing no strong correlation with the type and concentration of electrolytes. On the other hand, the average CE is clearly affected by the electrolyte; the Li deposition-stripping in the LiPF<sub>6</sub> electrolyte demonstrated the highest overpotential and the lowest CE compared to the LiFSI electrolytes. The surface chemical analysis indicates that the LiF-rich surface layer formed in the LiPF<sub>6</sub> electrolyte may be the cause for this. The Li electrodes in the LiFSI electrolytes, particularly in the high concentration electrolyte, show much lower overpotential and improved CE, which can be attributed to a more stable interface. This study provides realistic performances of thin Li electrodes in liquid electrolytes with practical parameters, which are conditions that should serve as the baseline for future investigations.

## References

- (1) Cheng, X. B.; Zhang, R.; Zhao, C. Z.; Zhang, Q. Toward Safe Lithium Metal Anode in Rechargeable Batteries: A Review. *Chem. Rev.* **2017**, *117* (15), 10403-10473.
- (2) Choudhury, S.; Archer, L. A. Lithium Fluoride Additives for Stable Cycling of Lithium Batteries at High Current Densities. *Adv. Electron. Mater.* **2016**, *2* (2), 1500246.
- (3) Zheng, J. M.; Engelhard, M. H.; Mei, D. H.; Jiao, S. H.; Polzin, B. J.; Zhang, J. G.; Xu, W. Electrolyte Additive Enabled Fast Charging and Stable Cycling Lithium Metal Batteries. *Nat. Energy.* **2017**, *2* (3), 17012.
- (4) Ota, H.; Shima, K.; Ue, M.; Yamaki, J. Effect of Vinylene Carbonate as Additive to Electrolyte for Lithium Metal Anode. *Electrochim. Acta.* **2004**, *49* (4), 565-572.
- (5) Guo, J.; Wen, Z. Y.; Wu, M. F.; Jin, J.; Liu, Y. Vinylene Carbonate-LiNO<sub>3</sub>: A Hybrid Additive in Carbonic Ester Electrolytes for SEI Modification on Li Metal Anode. *Electrochem. Commun.* **2015**, *51*, 59-63.
- (6) Fan, X. L.; Chen, L.; Ji, X.; Deng, T.; Hou, S. Y.; Chen, J.; Zheng, J.; Wang, F.; Jiang, J. J.; Xu, K.; Wang, C. S. Highly Fluorinated Interphases Enable High-Voltage Li-Metal Batteries. *Chem-Us* **2018**, *4* (1), 174-185.
- (7) Chen, S. R.; Zheng, J. M.; Mei, D. H.; Han, K. S.; Engelhard, M. H.; Zhao, W. G.; Xu, W.; Liu, J.; Zhang, J. G. High-Voltage Lithium-Metal Batteries Enabled by Localized High-Concentration Electrolytes. *Adv. Mater.* **2018**, *30* (21), 1706102.
- (8) Wang, J. H.; Yamada, Y.; Sodeyama, K.; Chiang, C. H.; Tateyama, Y.; Yamada, A. Superconcentrated Electrolytes for a High-Voltage Lithium-Ion Battery. *Nat. Commun.* **2016**, *7*, 12032.
- (9) Suo, L. M.; Hu, Y. S.; Li, H.; Armand, M.; Chen, L. Q. A New Class of Solvent-in-Salt Electrolyte for High-Energy Rechargeable Metallic Lithium Batteries. *Nat. Commun.* **2013**, *4*, 1481.
- (10) Qian, J. F.; Henderson, W. A.; Xu, W.; Bhattacharya, P.; Engelhard, M.; Borodin, O.; Zhang, J. G. High Rate and Stable Cycling of Lithium Metal Anode. *Nat. Commun.* **2015**, *6*, 6362.
- (11) Ren, X. D.; Chen, S. R.; Lee, H.; Mei, D. H.; Engelhard, M. H.; Burton, S. D.; Zhao, W. G.; Zheng, J. M.; Li, Q. Y.; Ding, M. S.; Schroeder, M.; Alvarado, J.; Xu, K.; Meng, Y. S.; Liu, J.; Zhang, J. G.; Xu, W. Localized High-Concentration Sulfone Electrolytes for High-Efficiency Lithium-Metal Batteries. *Chem-Us* **2018**, *4* (8), 1877-1892.

- (12) Tu, Z. Y.; Choudhury, S.; Zachman, M. J.; Wei, S. Y.; Zhang, K. H.; Kourkoutis, L. F.; Archer, L. A. Designing Artificial Solid-Electrolyte Interphases for Single-Ion and High-Efficiency Transport in Batteries. *Joule* **2017**, *1* (2), 394-406.
- (13) Zhao, J.; Liao, L.; Shi, F. F.; Lei, T.; Chen, G. X.; Pei, A.; Sun, J.; Yan, K.; Zhou, G. M.; Xie, J.; Liu, C.; Li, Y. Z.; Liang, Z.; Bao, Z. N.; Cui, Y. Surface Fluorination of Reactive Battery Anode Materials for Enhanced Stability. *J. Am. Chem. Soc.* **2017**, *139* (33), 11550-11558.
- (14) Li, N. W.; Shi, Y.; Yin, Y. X.; Zeng, X. X.; Li, J. Y.; Li, C. J.; Wan, L. J.; Wen, R.; Guo, Y. G. A Flexible Solid Electrolyte Interphase Layer for Long-Life Lithium Metal Anodes. *Angew. Chem., Int. Ed.* **2018**, *57* (6), 1505-1509.
- (15) Lopez, J.; Pei, A.; Oh, J. Y.; Wang, G. J. N.; Cui, Y.; Bao, Z. A. Effects of Polymer Coatings on Electrodeposited Lithium Metal. *J. Am. Chem. Soc.* **2018**, *140* (37), 11735-11744.
- (16) You, J. H.; Zhang, S. J.; Deng, L.; Li, M. Z.; Zheng, X. M.; Li, J. T.; Zhou, Y.; Huang, L.; Sun, S. G. Suppressing Li Dendrite by A Protective Biopolymeric Film from Tamarind Seed Polysaccharide for High-Performance Li Metal Anode. *Electrochim. Acta.* **2019**, *299*, 636-644.
- (17) Xu, R.; Zhang, X. Q.; Cheng, X. B.; Peng, H. J.; Zhao, C. Z.; Yan, C.; Huang, J. Q. Artificial Soft-Rigid Protective Layer for Dendrite-Free Lithium Metal Anode. *Adv. Funct. Mater.* **2018**, *28* (8), 1705838.
- (18) Zhu, B.; Jin, Y.; Hu, X. Z.; Zheng, Q. H.; Zhang, S.; Wang, Q. J.; Zhu, J. Poly(dimethylsiloxane) Thin Film as A Stable Interfacial Layer for High-Performance Lithium-Metal Battery Anodes. *Adv. Mater.* **2017**, *29* (2), 1603755.
- (19) Lin, D. C.; Liu, Y. Y.; Liang, Z.; Lee, H. W.; Sun, J.; Wang, H. T.; Yan, K.; Xie, J.; Cui, Y. Layered Reduced Graphene Oxide with Nanoscale Interlayer Gaps as A Stable Host for Lithium Metal Anodes. *Nat. Nanotechnol.* **2016**, *11* (7), 626-632.
- (20) Wang, H. S.; Li, Y. Z.; Li, Y. B.; Liu, Y. Y.; Lin, D. C.; Zhu, C.; Chen, G. X.; Yang, A. K.; Yan, K.; Chen, H.; Zhu, Y. Y.; Li, J.; Xie, J.; Xu, J. W.; Zhang, Z. W.; Vila, R.; Pei, A.; Wang, K. C.; Cui, Y. Wrinkled Graphene Cages as Hosts for High-Capacity Li Metal Anodes Shown by Cryogenic Electron Microscopy. *Nano Lett.* **2019**, *19* (2), 1326-1335.
- (21) Niu, C. J.; Pan, H. L.; Xu, W.; Xiao, J.; Zhang, J. G.; Luo, L. L.; Wang, C. M.; Mei, D. H.; Meng, J. S.; Wang, X. P.; Liu, Z.; Mai, L. Q.; Liu, J. Self-Smoothing Anode for Achieving High-Energy Lithium Metal Batteries under Realistic Conditions. *Nat. Nanotechnol.* **2019**, *14* (6), 594-601.

- (22) Tang, C. J.; Liu, Y. N.; Xu, C.; Zhu, J. X.; Wei, X. J.; Zhou, L.; He, L.; Yang, W.; Mai, L. Q. Ultrafine Nickel-Nanoparticle-Enabled SiO<sub>2</sub> Hierarchical Hollow Spheres for High-Performance Lithium Storage. *Adv. Funct. Mater.* **2018**, *28* (3), 1704561.
- (23) Cheng, X. B.; Hou, T. Z.; Zhang, R.; Peng, H. J.; Zhao, C. Z.; Huang, J. Q.; Zhang, Q. Dendrite-Free Lithium Deposition Induced by Uniformly Distributed Lithium Ions for Efficient Lithium Metal Batteries. *Adv. Mater.* **2016**, *28* (15), 2888-2895.
- (24) Li, Q.; Zhu, S. P.; Lu, Y. Y. 3D Porous Cu Current Collector/Li-Metal Composite Anode for Stable Lithium-Metal Batteries. *Adv. Funct. Mater.* **2017**, *27* (18), 1606422.
- (25) Chi, S. S.; Liu, Y. C.; Song, W. L.; Fan, L. Z.; Zhang, Q. Prestoring Lithium into Stable 3D Nickel Foam Host as Dendrite-Free Lithium Metal Anode. *Adv. Funct. Mater.* **2017**, *27* (24), 1700348.
- (26) Wang, H. S.; Lin, D. C.; Xie, J.; Liu, Y. Y.; Chen, H.; Li, Y. B.; Xu, J. W.; Zhou, G. M.; Zhang, Z. W.; Pei, A.; Zhu, Y. Y.; Liu, K.; Wang, K. C.; Cui, Y. An Interconnected Channel-Like Framework as Host for Lithium Metal Composite Anodes. *Adv. Energy Mater.* **2019**, *9* (7), 1802720.
- (27) Han, F. D.; Yue, J.; Chen, C.; Zhao, N.; Fan, X. L.; Ma, Z. H.; Gao, T.; Wang, F.; Guo, X. X.; Wang, C. S. Interphase Engineering Enabled All-Ceramic Lithium Battery. *Joule* **2018**, *2* (3), 497-508.
- (28) Zhao, Q.; Liu, X. T.; Stalin, S.; Khan, K.; Archer, L. A. Solid-State Polymer Electrolytes with in-Built Fast Interfacial Transport for Secondary Lithium Batteries. *Nat. Energy* **2019**, *4* (5), 365-373.
- (29) Zhou, J. Q.; Qian, T.; Liu, J.; Wang, M. F.; Zhang, L.; Yan, C. L. High-Safety All-Solid-State Lithium-Metal Battery with High-Ionic-Conductivity Thermoresponsive Solid Polymer Electrolyte. *Nano Lett.* **2019**, *19* (5), 3066-3073.
- (30) Croce, F.; Appetecchi, G. B.; Persi, L.; Scrosati, B. Nanocomposite Polymer Electrolytes for Lithium Batteries. *Nature* **1998**, *394* (6692), 456-458.
- (31) Wang, C. W.; Gong, Y. H.; Liu, B. Y.; Fu, K.; Yao, Y. G.; Hitz, E.; Li, Y. J.; Dai, J. Q.; Xu, S. M.; Luo, W.; Wachsman, E. D.; Hu, L. B. Conformal, Nanoscale ZnO Surface Modification of Garnet-Based Solid-State Electrolyte for Lithium Metal Anodes. *Nano Lett.* **2017**, *17* (1), 565-571.

- (32) Han, X. G.; Gong, Y. H.; Fu, K.; He, X. F.; Hitz, G. T.; Dai, J. Q.; Pearse, A.; Liu, B. Y.; Wang, H.; Rublo, G.; Mo, Y. F.; Thangadurai, V.; Wachsman, E. D.; Hu, L. B. Negating Interfacial Impedance in Garnet-Based Solid-State Li Metal Batteries. *Nat. Mater.* **2017**, *16* (5), 572-579.
- (33) Liu, J.; Bao, Z. N.; Cui, Y.; Dufek, E. J.; Goodenough, J. B.; Khalifah, P.; Li, Q. Y.; Liaw, B. Y.; Liu, P.; Manthiram, A.; Meng, Y. S.; Subramanian, V. R.; Toney, M. F.; Viswanathan, V. V.; Whittingham, M. S.; Xiao, J.; Xu, W.; Yang, J. H.; Yang, X. Q.; Zhang, J. G. Pathways for Practical High-Energy Long-Cycling Lithium Metal Batteries. *Nat. Energy* **2019**, *4* (3), 180-186.
- (34) Albertus, P.; Babinec, S.; Litzelman, S.; Newman, A. Status and Challenges in Enabling the Lithium Metal Electrode for High-Energy and Low-Cost Rechargeable Batteries. *Nat. Energy* **2018**, *3* (1), 16-21.
- (35) Juarez-Robles, D.; Chen, C-F.; Barsukov, Y.; Mukherjee, P. P. Impedance Evolution Characteristics in Lithium-Ion Batteries. *J. Electrochem. Soc.* **2017** *164*(4), A837-A847.
- (36) Aurbach, D.; Gofer, Y.; Langzam, J. The Correlation between Surface-Chemistry, Surface-Morphology, and Cycling Efficiency of Lithium Electrodes in a Few Polar Aprotic Systems. *J. Electrochem. Soc.* **1989**, *136* (11), 3198-3205.
- (37) Rosso, M.; Brissot, C.; Teysot, A.; Dolle, M.; Sannier, L.; Tarascon, J. M.; Bouchet, R.; Lascaud, S. Dendrite Short-Circuit and Fuse Effect on Li/Polymer/Li Cells. *Electrochim. Acta* **2006**, *51* (25), 5334-5340.
- (38) Chen, K. H.; Wood, K. N.; Kazyak, E.; LePage, W. S.; Davis, A. L.; Sanchez, A. J.; Dasgupta, N. P. Dead Lithium: Mass Transport Effects on Voltage, Capacity, and Failure of Lithium Metal Anodes. *J. Mater. Chem. A* **2017**, *5* (23), 11671-11681.
- (39) Aurbach, D.; Zinigrad, E.; Teller, H.; Dan, P. Factors which Limit the Cycle Life of Rechargeable Lithium (Metal) Batteries. *J. Electrochem. Soc.* **2000**, *147* (4), 1274-1279.
- (40) Wood, K. N.; Kazyak, E.; Chadwick, A. F.; Chen, K. H.; Zhang, J. G.; Thornton, K.; Dasgupta, N. P. Dendrites and Pits: Untangling the Complex Behavior of Lithium Metal Anodes through Operando Video Microscopy. *ACS Central Sci.* **2016**, *2* (11), 790-801.
- (41) Aurbach, D.; Gofer, Y.; Langzam, J. The Correlation between Surface-Chemistry, Surface-Morphology, and Cycling Efficiency of Lithium Electrodes in a Few Polar Aprotic Systems. *J. Electrochem. Soc.* **1989**, *136* (11), 3198-3205.

- (42) Aurbach, D.; Weissman, I.; Schechter, A.; Cohen, H. X-ray photoelectron spectroscopy studies of lithium surfaces prepared in several important electrolyte solutions. A Comparison with Previous Studies by Fourier Transform Infrared Spectroscopy. *Langmuir* **1996**, *12* (16), 3991-4007.
- (43) Wang, M. Q.; Huai, L. Y.; Hu, G. H.; Yang, S. S.; Ren, F. H.; Wang, S. W.; Zhang, Z. G.; Chen, Z. L.; Peng, Z.; Shen, C.; Wang, D. Y. Effect of LiFSI Concentrations to Form Thickness- and Modulus-Controlled SEI Layers on Lithium Metal Anodes. *J. Phys. Chem. C* **2018**, *122* (18), 9825-9834.
- (44) Fan, X. L.; Ji, X.; Han, F. D.; Yue, J.; Chen, J.; Chen, L.; Deng, T.; Jiang, J. J.; Wang, C. S. Fluorinated Solid Electrolyte Interphase Enables Highly Reversible Solid-state Li Metal Battery. *Sci. Adv.* **2018**, *4* (12), 9245.
- (45) Jay, R.; Tomich, A. W.; Zhang, J.; Zhao, Y. F.; De Gorostiza, A.; Lavallo, V.; Guo, J. C. Comparative Study of Mg(CB11H12)(2) and Mg(TFSI)(2) at the Magnesium/Electrolyte Interface. *Acs Appl. Mater. Interfaces* **2019**, *11* (12), 11414-11420.
- (46) Fu, C. Y.; Wong, B. M.; Bozhilov, K. N.; Guo, J. C. Solid State Lithiation-Delithiation of Sulphur in Sub-Nano Confinement: A New Concept for Designing Lithium-Sulphur Batteries. *Chem. Sci.* **2016**, *7* (2), 1224-1232.
- (47) Fu, C. Y.; Li, G. H.; Zhang, J.; Cornejo, B.; Piao, S. S.; Bozhilov, K. N.; Haddon, R. C.; Guo, J. C. Electrochemical Lithiation of Covalently Bonded Sulfur in Vulcanized Polyisoprene. *Acs Energy Lett.* **2016**, *1* (1), 115-120

## **Chapter 3: Identification of failure mechanism study of Li metal batteries**

### **3.1 Introduction**

In order to better enable the electric vehicles-low cost and long range, the study on next generation high energy density Li metal batteries has been stimulated, as the traditional Li-ion batteries can not fulfill the requirements for long range and low cost electric vehicles.<sup>1</sup> The short cycle life and safety issue hindered the commercialization of Li metal batteries. In order to improve the performance of Li metal batteries, the failure mechanism should be clearly understood.

The well accepted failure mechanism of Li metal anode were mainly including: electrolyte depletion,<sup>2-4</sup> loss of Li inventory,<sup>5</sup> and the increased concentration overpotential.<sup>6</sup>

The cell component of the Li metal batteries consists Li metal electrode, Li transition metal oxide cathode, and organic electrolyte. In order to identify the failure mechanism of the Li metal batteries, the thorough analysis on these three parts should be considered.

Li||Li symmetric cell is not a good experiment set up to evaluate the failure mechanism for Li metal batteries since the normal testing protocol for Li metal batteries involve the slow deposition rate and fast stripping rate for Li metal anode part, while the Li||Li symmetric cell can not deconvolute the effect of the counter electrode. In order to identify the failure mechanism of Li metal batteries, the experiment set up should based on the Li metal batteries.

## **3.2 Experimental methods**

### **3.2.1 Materials**

The electrolyte containing 1M LiPF<sub>6</sub> in the mixture of EC/DEC =50:50 (V/V), battery grade was purchased from Sigma-Aldrich. The single crystal LiNi<sub>0.6</sub>Mn<sub>0.2</sub>Co<sub>0.2</sub>O<sub>2</sub> (NMC622) was purchased from Targray Technology International Inc..

### **3.2.2 Electrodes preparation for coin-cells and pouch cells**

The lab-made thin Li foil (50 μm in thickness) was prepared using a previously reported method.<sup>7</sup> The cathode slurry was prepared by mixing 90 wt.% NMC622, 5 wt.% carbon black (Supper C65), and 5 wt.% polyvinylidene fluoride (PVDF, Sigma-Aldrich, Mw~534,000) in N-Methyl-2-pyrrolidone (NMP, Anhydrous, 99.5%, Sigma-Aldrich) through centrifugal mixer (Thinky, AR-100) for 15 mins. All the materials in the slurry preparation except NMP were dried under vacuum at 70°C for 24 hours prior to use. NMP were dried with the 3Å molecular sieves prior to use. The weight ratio of liquid to solid in the slurry was 1.65. The slurry was coated with an automatic tape casting coater (MTI corporation) onto an aluminum current collector (16μm, Gelon LIB Group) with the film applicator set to 300 μm to make 3 mAh cm<sup>-2</sup> NMC622 cathode. The coated electrodes were transferred into the glovebox and dried at room temperature for 12 hours. Then the electrodes were dried under vacuum inside glovebox at 120°C for 12 hours prior to use. The thickness of electrodes were controlled by calendaring process through mechanic roller.

### **3.2.3 Cell assembly and electrochemical experiments**

CR-2016 type coin cells (Gelon LIB Group) were used in the measurements of the Li||NMC622 cell cycling performance. Celgard-2400 was used as the separator. The amount of electrolyte in the pouch cells was kept at 3 g Ah<sup>-1</sup>. The cycling experiments were performed with Neware battery testers. All the Li||NMC622 cells were tested under galvanostatically charging to 4.3 V and then hold the voltage at 4.3 V until the current dropped less than C/30. After that, galvanostatically discharging the cell until voltage less than 2.5 V. The C rate for formation cycles were kept C/20 for charging and discharging. After formation cycles, using C/10 for charging and C/3 for discharging. And all the constant voltage holding until the current less than C/30.

### 3.3 Results and discussion

The Li metal battery was consists of: Li metal anode with thickness of 50  $\mu\text{m}$  on Cu current collector, the standard electrolyte using 1M  $\text{LiPF}_6$  in EC/DEC (50:50, volume ratio) with electrolyte amount to capacity ratio of  $3\text{g Ah}^{-1}$ , NMC622 cathode with area loading of  $\sim 3\text{mAh cm}^{-2}$ .

**Table 3. 1** Cell parameters and testing conditionals for the Li||NMC622 cell.

	<b>Parameter</b>	<b>Value</b>
	Discharge capacity	180 $\text{mAh g}^{-1}$
	Active material loading	90%
	Area capacity (each side)	3.0 $\text{mAh cm}^{-2}$
	Electrode thickness (each side)	90 $\mu\text{m}$
Li anode	Thickness (each side)	50 $\mu\text{m}$
Electrolyte	E/C ratio	3.0 $\text{g Ah}^{-1}$
Testing Conditions	Formation current	C/20
	Constant voltage current limit	C/30
	Cycling charging current	C/10
	Cycling discharging current	C/3

After cell dead (capacity drops till near zero), the cell then do the following steps as shown

in **Figure 3.1**:

1. Resume the cycling under the current of C/20 for 3 cycles;
2. Disassemble the cell, replace the cycled Li metal anode with a new Li metal anode then cycling under the current of C/20 for 1cycle;
3. Disassemble the cell, change back the cycled Li metal anode, add additional electrolyte then cycling under the current of C/20 for 3 cycles then cycling under C/10 for charging and C/3 for discharging
4. Disassemble the cell, replace the cycled Li metal anode with a new Li metal anode and add additional electrolyte, then then cycling under the current of C/20 for 3 cycles then cycling under C/10 for charging and C/3 for discharging

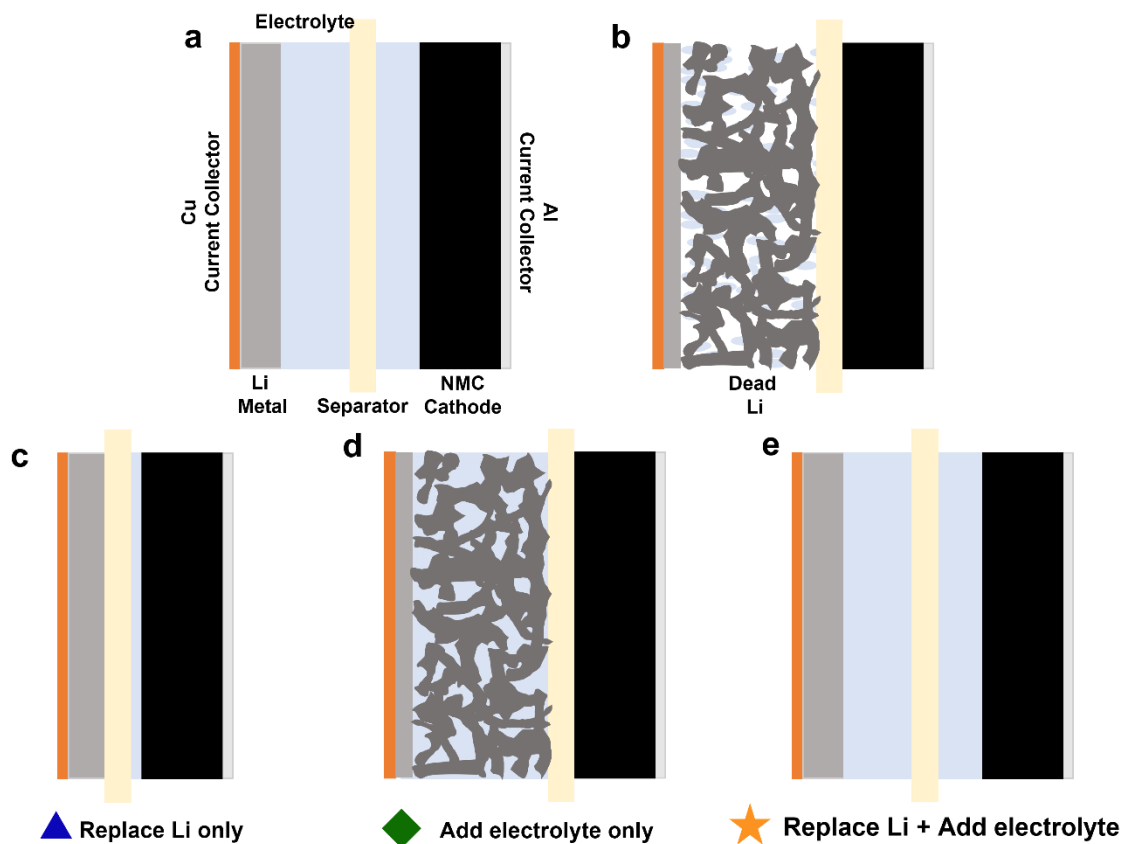


**Figure 3. 1** Schematic diagram illustration of the experimental design for identification of failure mechanism for Li metal batteries.

The cycling performance of the Li||NMC622 cell was demonstrated in **Figure 3.2**. The original cell was dead after cycling for ~45 cycles. When resume the cycling under the current of  $C/20$ , the discharging capacity increased from near zero to  $1.5 \text{ mAh cm}^{-2}$  and then dropped for the following cycles, which interpret the large concentration overpotential generated in the cell. By only replacing a new Li metal anode (no additional electrolyte), the cell still able to cycling, which indicated the electrolyte was not fully depleted. Then if using the old cycled Li metal anode with additional electrolyte, the discharging capacity increased to near the original capacity. However, the capacity still dropped for the following cycles, which indicated the electrolyte amount was one of the cause for the large

overpotential. Lastly, the cell using the new Li metal anode with additional electrolyte, the discharging capacity was stable for the eight cycles, which indicated the major cause for the large overpotential was originated from Li metal anode.

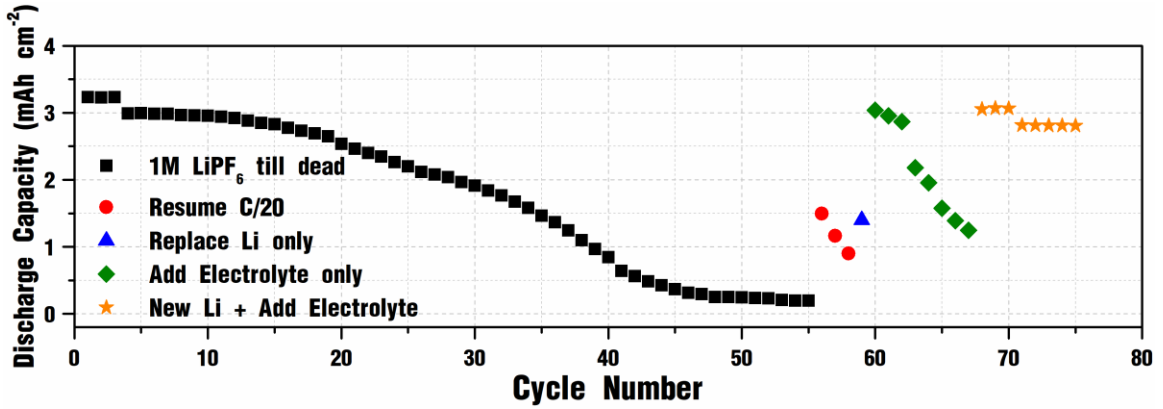


**Figure 3. 2** Cycling performance of Li metal batteries.

The Li source remaining for the Li metal anode has also been evaluated by stripping the cycled Li metal anode (till 1V in Li||Li symmetric cell) as shown in **Figure 3.3**. The Li metal consumption rate could be calculated by the following equations:

$$k_{Li} = \frac{Q_{Con}}{Q_{Discharging}}$$

$$Q_{Con} = Q_{original} - Q_{remaining} = m_{Li} \times 3.86 - I_{Strip} \times T_{Strip}$$

$$Q_{Discharging} = \sum_{1,2,..i} Q_{Discharging}^i$$

where  $k_{Li}$  is the Li consumption rate,  $Q_{Con}$  is the total capacity of Li consumed during cycling,  $Q_{original}$  is the original Li source capacity,  $m_{Li}$  is the original weight of Li metal foil ( $\sim 50 \mu\text{m}$ ), 3.86 is the specific capacity of Li metal ( $\sim 3.86 \text{ mAh g}^{-1}$ ),  $I_{Strip}$  is the stripping current for the Li||Li symmetric cell,  $T_{Strip}$  is the total stripping time after the stripping

voltage reaches 1V,  $Q_{Discharging}$  is the cell total discharging capacity during the cycling,  $Q_{Discharging}^i$  is the cell discharging capacity of the  $i^{\text{th}}$  cycle.

Take an example of the Li||NMC622 cell with the weighted Li metal foil of 5.32mg. The total discharging capacity is 0.1165Ah, the total stripping time is 31.9h under the stripping current of 0.3mAh  $\text{cm}^{-2}$  (5/8 inch in diameter for Li metal electrode). The calculated Li consumption rate is 1.389%, which means there will be Li consumed (1.389% of the total discharging capacity on average) from original Li source in each cycle.

**Table 3. 2** Summary of the discharge capacity by changing parts after cell dead

<b>Change parts after dead</b>	<b>Capacity increase</b>	<b>Indication</b>
Original cell	Drop to 0 after 45 cycles	Cell dead
Resume at C/20	Increase to 1.5 mAh $\text{cm}^{-2}$ , but dropped for the following cycles	Large concentration overpotential
Replace Li only (no additional electrolyte)	Increase to 1.5 mAh $\text{cm}^{-2}$	Electrolyte not fully depleted
Add electrolyte only (change back to the cycled Li)	Increase to 3 mAh $\text{cm}^{-2}$ , but dropped for the following cycles	Electrolyte amount is the major cause for large overpotential
New Li and additional electrolyte	Increase to 3 mAh $\text{cm}^{-2}$ and stable for the following cycles	large overpotential comes from Li metal anode

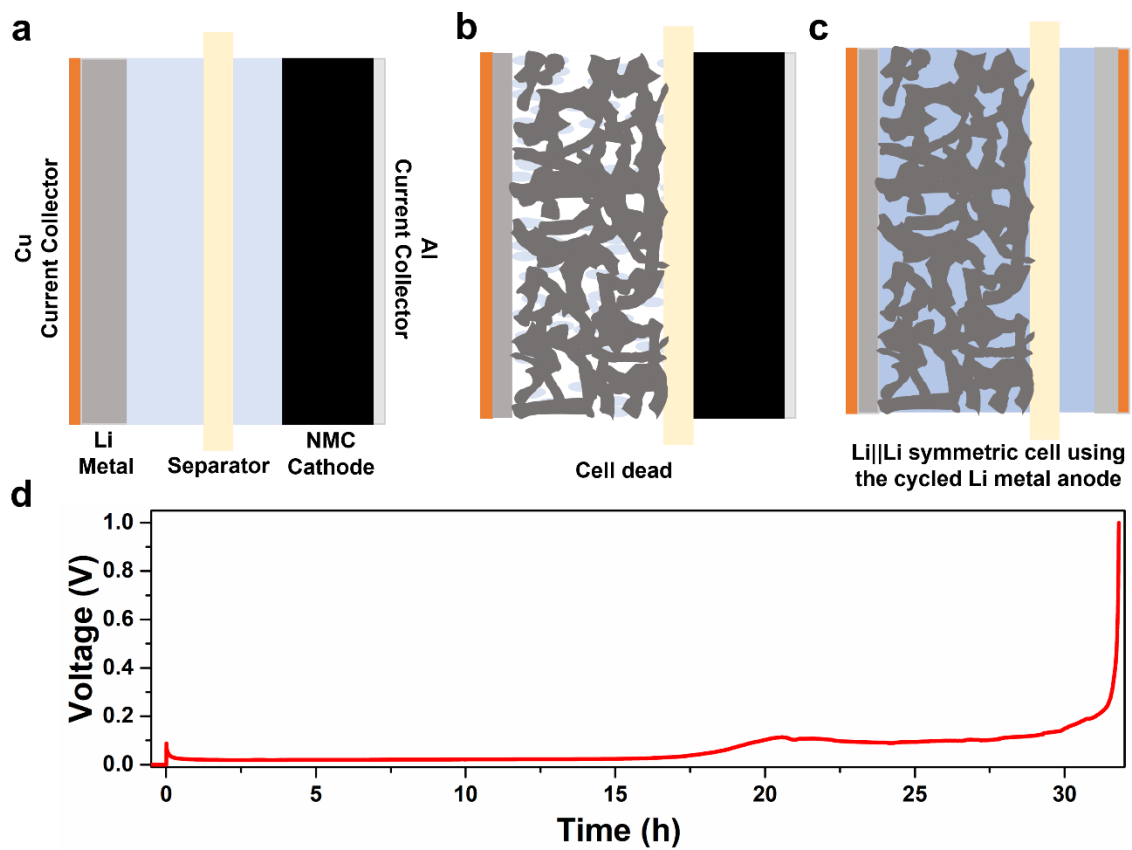


**Figure 3. 3** Illustration of the remaining Li source evaluation by Li||Li symmetric cell. d) Example of voltage profile for the Li stripping in Li||Li symmetric cell using the cycled Li metal anode under the current of  $0.3 \text{ mA cm}^{-2}$ .

### 3.4 Conclusion

In conclusion, the cell components including Li metal anode, electrolyte and Li transition metal oxide cathode should be thoroughly evaluated for studying the failure mechanism of Li metal battery. In this specific example of the ( $\sim 50 \mu\text{m}$ )Li||NMC622 ( $3\text{mAh cm}^{-2}$  loading) with electrolyte to capacity ratio of  $3\text{g Ah}^{-1}$ , the cell failure was mainly originated from Li metal anode and electrolyte. In addition, the electrolyte in the highly porous Li (accumulated dead Li and the deposited Li) was the cause for the large overpotential. The capacity loss from NMC622 cathode is negligible for this specific example. The electrolyte is not fully depleted and the Li metal anode still have large amount of Li source which is contradictory against the literature. (add reference) The concentration overpotential increasing is more dominant for the total overpotential increase rather than the SEI and charge transfer increase in Li metal anode. The concentration overpotential increasing is mainly due to the high tortuosity in the porous Li (accumulated dead Li and deposited Li) and the decreasing of the effective diffusion coefficient. (Add reference)

## References

- (1) Office of Technology Transitions, Battery500 Consortium to Spark EV Innovations: Pacific Northwest National Laboratory-led, 5-year \$50M effort seeks to almost triple energy stored in electric car batteries, <https://www.energy.gov/technologytransitions/articles/battery500-consortium-spark-ev-innovations-pacific-northwest-national> (accessed: July 2016).
- (2) Aurbach, D., Zinigrad, E., Teller, H., & Dan, P. (2000). Factors which limit the cycle life of rechargeable lithium (metal) batteries. *Journal of The Electrochemical Society*, 147(4), 1274.
- (3) Chen, S., Niu, C., Lee, H., Li, Q., Yu, L., Xu, W., ... & Liu, J. (2019). Critical parameters for evaluating coin cells and pouch cells of rechargeable Li-metal batteries. *Joule*, 3(4), 1094-1105.
- (4) Aurbach, D., Zinigrad, E., Cohen, Y., & Teller, H. (2002). A short review of failure mechanisms of lithium metal and lithiated graphite anodes in liquid electrolyte solutions. *Solid state ionics*, 148(3-4), 405-416.
- (5) Niu, C., Lee, H., Chen, S., Li, Q., Du, J., Xu, W., ... & Liu, J. (2019). High-energy lithium metal pouch cells with limited anode swelling and long stable cycles. *Nature Energy*, 4(7), 551-559.
- (6) Chen, K. H., Wood, K. N., Kazyak, E., LePage, W. S., Davis, A. L., Sanchez, A. J., & Dasgupta, N. P. (2017). Dead lithium: mass transport effects on voltage, capacity, and failure of lithium metal anodes. *Journal of Materials Chemistry A*, 5(23), 11671-11681.
- (7) Zhang, J., Shi, J., Wen, X., Zhao, Y., & Guo, J. (2020). Properties of thin lithium metal electrodes in carbonate electrolytes with realistic parameters. *ACS Applied Materials & Interfaces*, 12(29), 32863-32870.

## Chapter 4: Regulating Lithium Deposition via Electropolymerization of Acrylonitrile in Rechargeable Lithium Metal Batteries

### 4.1 Introduction

The resurrection of Li metal anode has been seen in recent years due to the demand for lithium-ion batteries to achieve 500 Wh kg<sup>-1</sup> specific energy<sup>1,2</sup>. It is recognized that Li deposition in liquid electrolytes is always accompanied by chemical and electrochemical decomposition of the anions and solvents. The decomposition products instantaneously passivate the Li surface, which results to intrinsic porous structure (i.e., mossy Li) with significant volume expansion. These continuous parasitic reactions also lead to low coulombic efficiency (CE) of Li metal anode, fast electrolyte depletion, and formation of dead Li<sup>3</sup>. A strategy to improve Li metal anode is to implement a stable artificial solid electrolyte interphase (SEI) that alleviates electrolyte decomposition and enables uniform interfacial current. The artificial SEIs can be prepared via ex situ methods as reported in the synthesis of lithium fluoride (LiF)<sup>4-9</sup>, lithium nitride (Li<sub>3</sub>N)<sup>10-13</sup>, polyethylene oxide<sup>14-17</sup>, and Al<sub>2</sub>O<sub>3</sub>/polyvinylidene fluoride-hexafluoropropylene SEIs<sup>18-20</sup>. These ex-situ methods often involve complex processes and strict environment control that could be impractical. Furthermore, if the ex situ implemented SEI were compromised during the Li deposition-stripping, such as LiF layer rupture under continuous structure change<sup>21</sup> or anodic decomposition of Li<sub>3</sub>N<sup>22</sup>, there would be no means to repair. Therefore, in situ formation of artificial SEI via electrolyte additives can be a superior strategy. The in situ formation of inorganic-rich SEI such as LiF is typically achieved via cathodic decomposition of fluorinated co-solvents<sup>23-26</sup>, while organic-rich SEI can be obtained via

electropolymerization of organic compounds such as the ones containing vinyl group<sup>27-31</sup>. In this study, we investigate acrylonitrile (AN) as an SEI-forming additive for Li metal anode via electropolymerization. Polyacrylonitrile (PAN) was known as an excellent candidate for polymer electrolytes due to the coordination between the nitrile group (C≡N) and Li cation<sup>32-34</sup>. Our focus is to understand the effect of the PAN SEI on the Li anode deposition-stripping and the subsequent performance of full cells using the LiNi<sub>0.6</sub>Mn<sub>0.2</sub>Co<sub>0.2</sub>O<sub>2</sub> (NMC622) cathode.

## **4.2 Experimental Methods**

### **4.2.1 Materials**

The solvent of the electrolyte is a mixture of ethylene carbonate (EC, anhydrous, 99%, Sigma-Aldrich) and diethyl carbonate (DEC, anhydrous, ≥99%, Sigma-Aldrich) with 1:1 volume ratio. 3Å molecular sieves (Sigma-Aldrich), after vacuum drying at 300°C for 24 hours inside an argon-filled glovebox, were used to remove the water residue from the solvents. LiFSI (99%, Oakwood Chemical) was dried under vacuum at 80°C inside the argon-filled glovebox for 24 h prior to use. Acrylonitrile (≥99%, Sigma Aldrich) was re-distilled then dried with 3Å molecular sieves prior to use. LiNi<sub>0.6</sub>Mn<sub>0.2</sub>Co<sub>0.2</sub>O<sub>2</sub> (NMC622) was purchased from Targary Technology International Inc..

### **4.2.2 Cell assembly and electrochemical experiments**

The thin Li foil (50 μm in thickness) was prepared using a previously reported method<sup>3</sup>. The double-side Li metal anode was prepared by sandwiching a copper foil with two 50-μm Li metal foil, and pressed with a mechanical roller. The cathode slurry was prepared

by mixing 90 wt.% NMC622, 5 wt.% carbon black (Supper C65), and 5 wt.% polyvinylidene fluoride (PVDF, Sigma-Aldrich, Mw~534,000) in N-Methyl-2-pyrrolidone (NMP, Anhydrous, 99.5%) by ball milling (Fritsch, Pulverisette 23) for 15 mins inside the argon-filled glovebox. All the materials in the slurry preparation except NMP were dried under vacuum at 70°C for 24 hours prior to use. NMP were dried with the 3Å molecular sieves prior to use. The weight ratio of liquid to solid in the slurry was 1.58. The slurry was coated with an automatic tape casting coater (MTI corporation) onto an aluminum current collector with the film applicator set to 300 μm to make 3 mAh cm<sup>-2</sup> NMC622 cathode. The coated electrodes were transferred into the glovebox and dried under vacuum at 120°C for 12 hours prior to use. Single-sided and double-sided cathodes were prepared for coin cells and pouch cells, respectively.

CR-2016 type coin cells were used in the measurements of the Li||Li symmetric cell cycle stability. Celgard-3501 was used as the separator. All Li||Li symmetric cells contained 30 μL electrolyte. Pouch cell were assembled inside an argon-filled glovebox. The amount of electrolyte in the pouch cells was kept at 4 g Ah<sup>-1</sup>. A lab-made pouch cell test holder (**Figure 4.1**) was used during cycling.

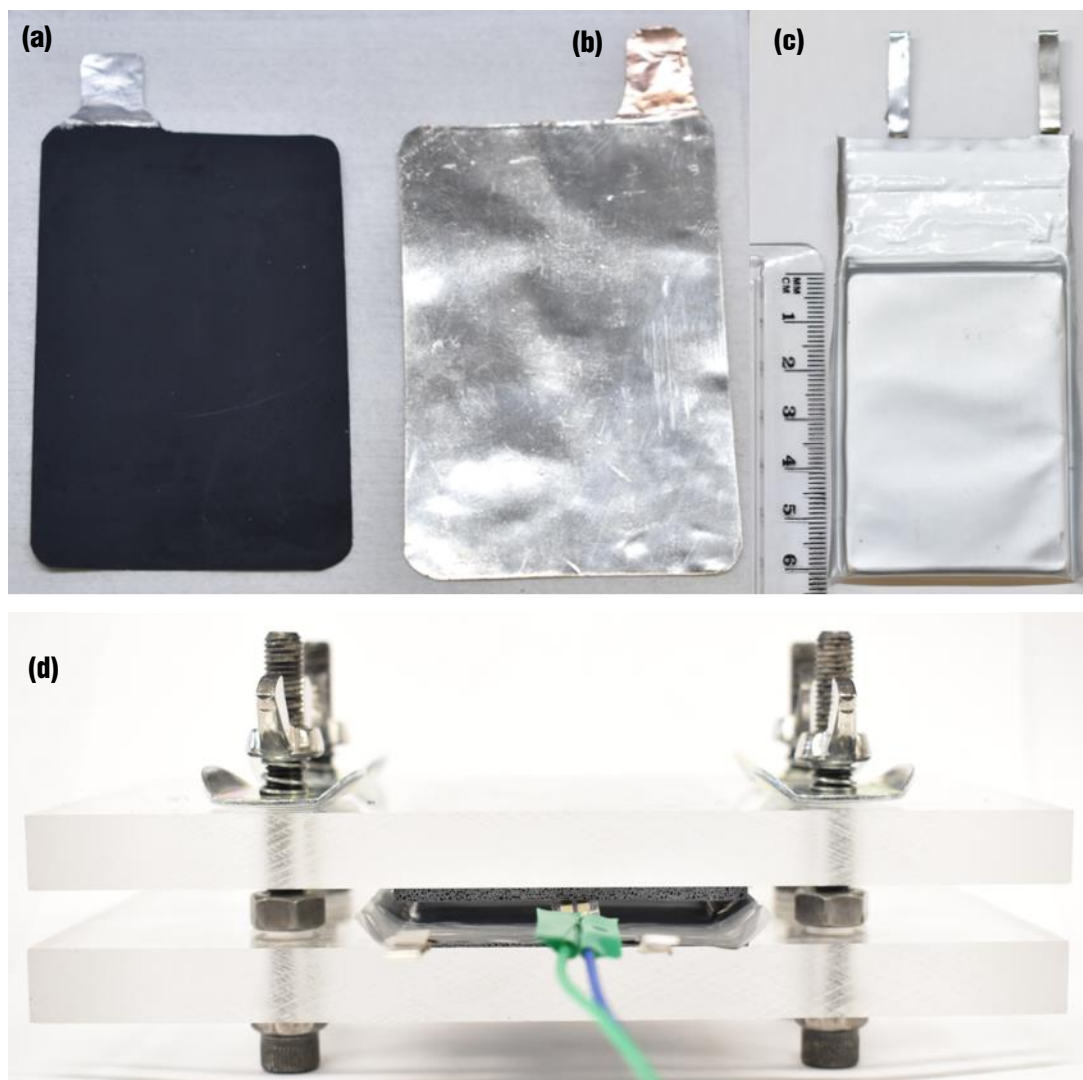


**Figure 4. 1** Optical images of (a) NMC622 electrode (3.8 cm × 5.9 cm), (b) Li metal anode (4.0 cm × 6.0 cm), (c) assembled pouch cell, and (d) testing holder for Li||NMC622 pouch cells.

The cycling experiments were performed with either Arbin or Neware battery testers. Linear sweep was carried out in a three-electrode cell (Gamry) with a Gamry potentiostat (Reference 1000). Two pieces of Li foil (99.9%, Alfa Aesar) were used as the counter and reference electrode, and a glassy carbon plate (Alfa Aesar) was used as the working electrode.

### 4.2.3 Coulombic efficiency measurement

CR-2016 type coin cells were used to measure the average coulombic efficiency: a lab-made Li foil with the thickness around 50  $\mu\text{m}$  was first weighed and then pressed to a Cu substrate as the working electrode. Another identically made Li electrode was used as the counter electrode without weighing. Galvanostatic stripping was first applied to the working electrode under certain current for a certain period of time, followed by deposition with the same current and same period of time to complete one cycle. After a set number of cycles, any remaining Li on the working electrode was completely stripped using a 0.5  $\text{mA cm}^{-2}$  current until the stripping cutoff potential (1 V) was reached. Representative voltage and current profiles in the measurement of average CE is shown in **Figure 4.2**. The average CE can be calculated from the following equation:<sup>3</sup>

$$CE_{Average} = \frac{(T_s \times J + n \times C_C) \times A}{m_{Li} \times Q + n \times C_C \times A} \quad (1)$$

where  $n$  is the cycle number;  $C_C$  is the cycling capacity (e.g., 2  $\text{mAh cm}^{-2}$  with  $1 \text{mA cm}^{-2}$  cycling for 1h);  $T_s$  (hour) is the time to complete the stripping of the working electrolyte;  $J$  is the current to complete stripping ( $0.5 \text{mA cm}^{-2}$ ),  $A$  is the area of the working electrode ( $1.266 \text{cm}^2$ ), and  $m_{Li}$  is the original mass (in mg) of the Li on the working electrode.  $Q$  is the theoretical capacity of Li ( $3.86 \text{mAh mg}^{-1}$ ).

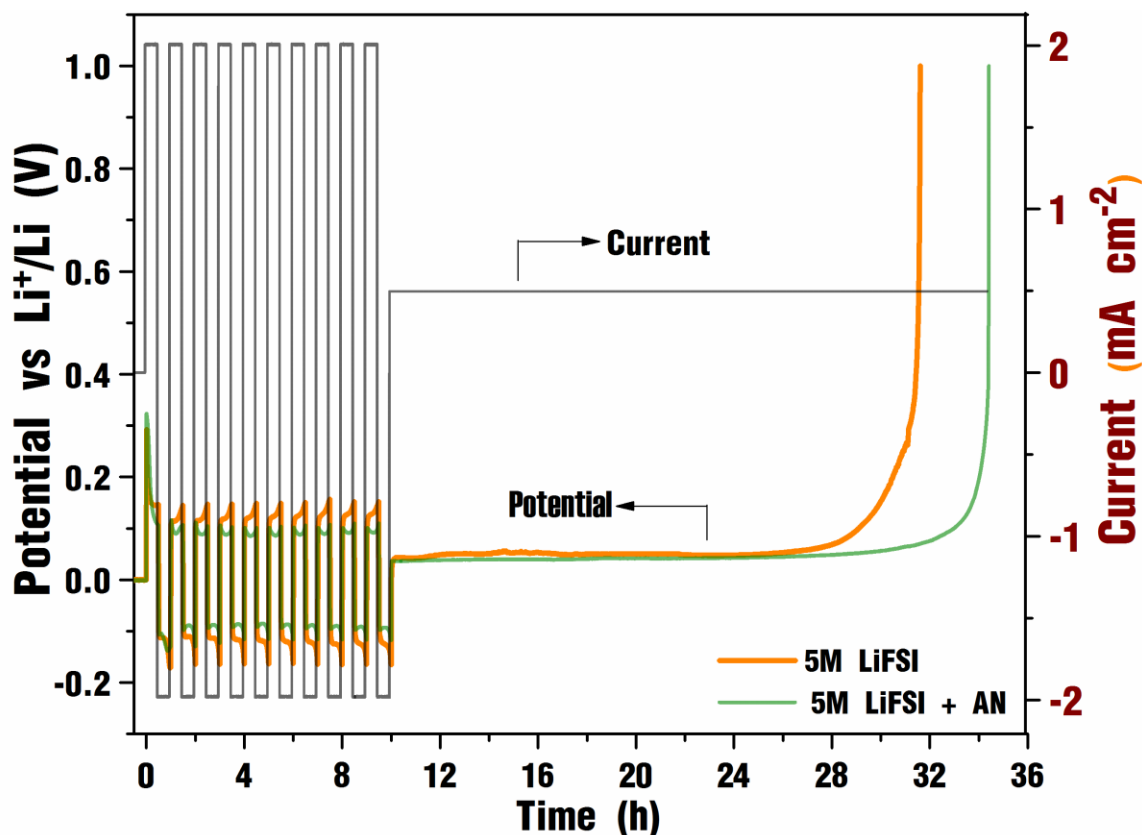


**Figure 4. 2** Representative voltage and current profiles in the measurement of average CE.

CE of Li deposition-stripping in Li||Cu cells was also measured using CR-2016 type coin cells with  $1 \text{ mAh cm}^{-2}$  areal capacity. A Cu foil and a Li foil ( $750 \text{ }\mu\text{m}$ ) was used as the working electrode and the counter electrode, respectively. The electrolyte amount in the Li||Cu cells was controlled at  $15 \text{ }\mu\text{L}$  for each cell. Two areal currents were used including  $0.5 \text{ mA cm}^{-2}$  and  $1 \text{ mA cm}^{-2}$ . The stripping potential limit was set at  $1 \text{ V vs. Li}^+/\text{Li}$ .

#### 4.2.4 Characterization methods

The surface morphology and the thickness of the electrode were characterized using scanning electron microscope (SEM, Nova Nano S450,  $10 \text{ kV}$ ). The samples were retrieved in an argon-filled glovebox and washed with dimethyl carbonate thoroughly to remove the

residual electrolyte. Prior to the SEM characterization, the samples were dried at room temperature for 24 hours inside the argon-filled glovebox. The samples were then transported to the SEM facility inside a stainless-steel tube with KF-flange sealing. The samples were loaded in the SEM using a glove-bag with argon purging gas without exposing to ambient environment. The elemental mapping of the samples was collected using an Energy Dispersive X-ray (EDX) spectrometer coupled with the SEM. X-ray photoelectron spectroscopy (XPS) data were collected using Kratos AXIS Supra (Al  $K\alpha=1486.7$  eV) at UC Irvine Materials Research Institute (IMRI). The samples were prepared following the same procedure for SEM samples. The samples were transported to the XPS facility inside a stainless-steel tube with KF flange sealing filled with argon. Finally, the samples were loaded in the sample chamber in the glovebox integrated with Kratos AXIS Supra for XPS analysis. All peaks of XPS data were calibrated with the reference peak of C 1s at 284.6 eV (the adventitious carbon). The relative sensitivity factor for C 1s, O 1s, F 1s, S 2p, N 1s, and Li 1s were given as 0.278, 0.736, 1, 0.723, 0.477 and 0.025, respectively. The relative atomic ratio was calculated from the following equation:

$$RA_i = \frac{A_i/S_i}{\sum A_i/S_i} \times 100\% \quad (2)$$

where  $RA_i$  is the relative atomic ratio of component  $i$ ,  $A_i$  is the area of the deconvoluted peak of component  $i$ , and  $S_i$  is the relative sensitivity factor for component  $i$ .

#### 4.2.5 Computational Method

Classical molecular dynamics (MD) simulation is used to calculate the solvation structure via Large-scale Atomic/Molecular Massively Parallel Simulator (LAMMPS).[35] The compositions of bulk electrolytes are exactly the same as experiment setup with 267 LiFSI molecules in a  $50 \times 50 \times 50 \text{ \AA}^3$  cubic simulation box. The initial configuration is obtained by PACKMOL (as shown in **Figure 4.3**)<sup>36</sup>.

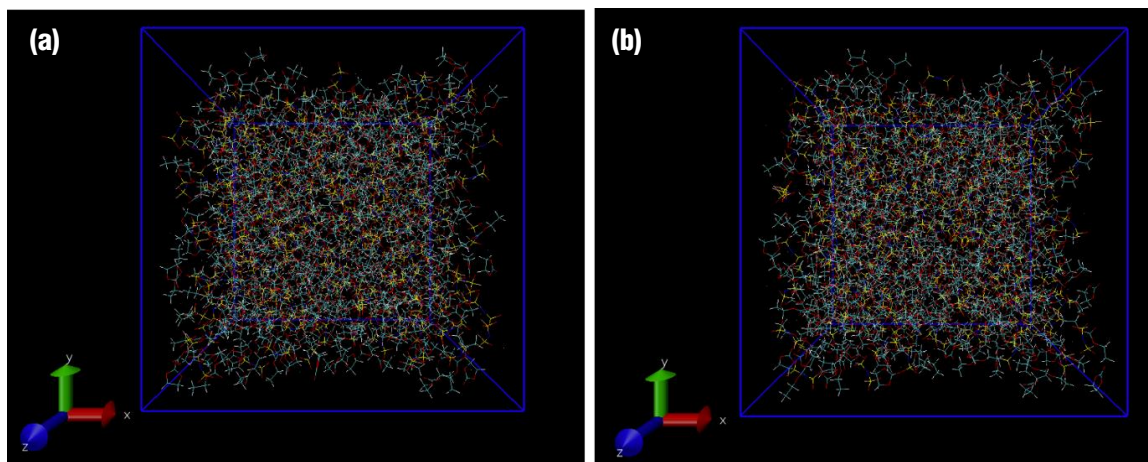


**Figure 4. 3** The initial molecular dynamics simulation cell of (a) LiFSI in EC/DEC and (b) LiFSI in EC/DEC with AN.

The Optimized Potentials for Liquid Simulations All Atom(OPLS-AA) force field was used for EC and DEC. The force field parameters for Li cation is from Jensen and Jorgensen<sup>37</sup>, for FSI anion is from Shimizu et. al.<sup>38</sup>. Lorentz-Berthelot mixing rule was used for van der Waals (vdW) interactions between different type of atoms. For the electrostatic potential, the atomic partial charges were derived from first principles calculation at the Hartree-Fock/aug-cc-pvdz level via the restrained electrostatic potential (RESP) method available from NWChem<sup>39,40</sup>. Particle-particle particle-mesh (PPPM)

method was used to describe the long-range electrostatic interactions with the grid size of 1 Å<sup>41</sup>. The cutoff distance for vdW and real-space electrostatic interactions is set as 15 Å. Periodic boundary conditions are applied to all three dimensions. In order to avoid the local confined configuration at room temperature, an annealing procedure is used before the system is equilibrated<sup>42</sup>. All the systems were first equilibrated in the isothermal-isobaric (NPT) ensemble with the Nose-Hoover thermo/barostat at 298 K and 1 atm for 2 ns. Then, the annealing process was performed for all systems in the canonical (NVT) ensemble with the Nose-Hoover thermostat. All the systems were heated from 298 K to 450 K for 1 ns, equilibrated at 400 K for 1ns and annealed from 450 K to 298 K for 1 ns. All the systems were equilibrated for 5 ns in the NVT ensemble at 298 K, and the solvation structure is directly taken from the final snapshot of the equilibrated system. The time constant of all molecular dynamics simulations is set as 1 ps .

To calculate the reduction potential, the solvation structure was further optimized with density functional theory (DFT) via NWChem. The DFT calculation was performed at the level of Perdew-Burke-Ernzerhof(PBE)/6-31+G(d,p) for its excellent combination of efficiency and accuracy compared to higher-level methods<sup>43</sup>. The solvent effect is accounted for by applying the Conductor-like Screening Model (COSMO) with the dielectric constant of 46.2925 for the organic electrolyte<sup>44</sup>. The vertical reduction potential related to Li||Li<sup>+</sup> can be calculated from

$$E_{red} = \frac{-\left(\Delta G_{reduction} + \Delta G_{solv}^0(\text{reduced}) - \Delta G_{solv}^0(\text{initial})\right)}{F} - 1.4 \text{ V} \quad (3)$$

where  $\Delta G_{reduction}$  is the Gibbs energy of the reduction in the gas phase at 298.15 K,  $\Delta G_{solv}^0$  is the Gibbs energy of solvation, and  $F$  is the Faraday constant.

### 4.3 Results and Discussion

Our previous study suggests that 5 M lithium bis(fluorosulfonyl)imide (LiFSI) in the mixture of ethylene carbonate (EC) and diethyl carbonate (DEC) with a 1:1 volume ratio is a good baseline electrolyte to deliver reasonable cycle stability and CE of Li anode [3]. Therefore, this electrolyte is selected for this study. **Figure. 4.4a** displays the cathodic linear sweep on a glassy carbon working electrode in the electrolyte with and without AN (AN is 0.5 wt.% in all electrolytes). A distinct reduction peak at 0.9 V vs. Li<sup>+</sup>/Li is observed in the electrolyte with AN, which can be attributed to the electropolymerization of AN. The cathodic current at 0 V in the electrolyte with AN is significantly lower than that in the electrolyte without AN, which is another indication of the formation of an interfacial layer. The galvanostatic Li deposition curve in the electrolyte with AN (**Figure. 4.4b**) demonstrates a higher initial overpotential, which also indicates the formation of a SEI on the Li surface. The theoretical study provides further evidence of electropolymerization of AN: **Figure. 4.4c** displays the representative Li<sup>+</sup> solvation structures with and without AN ([Li(EC)<sub>3</sub>AN]FSI vs. [Li(EC)<sub>3</sub>]FSI), obtained from the molecular dynamics simulation. According to the density functional theory (DFT) calculations, the cathodic decomposition potentials of the Li<sup>+</sup> solvation in the presence of AN is 1.73 V vs. Li<sup>+</sup>/Li, which is 0.585 V higher than that without AN. **Figure. 4.4d** shows the DFT predictions for the cathodic stability of three Li<sup>+</sup>-solvent pairs (Li<sup>+</sup>-AN, Li<sup>+</sup>-EC, and Li<sup>+</sup>-DEC) and the Li<sup>+</sup>-FSI<sup>-</sup> pair in

the electrolyte.  $\text{Li}^+$ -AN has the highest reduction potential vs.  $\text{Li}^+/\text{Li}$ . These computational results suggest that AN can be electropolymerized prior to the decomposition of the electrolyte. In addition, the bond dissociation energy (BDE) for  $\text{C}\equiv\text{N}$  and  $\text{C}=\text{C}$  bonds in AN in both gas phase and solution phase (the  $[\text{Li}(\text{EC})_3\text{AN}]\text{FSI}$  configuration in **Figure 4.4c**) is also calculated in **Table 4.1**.

**Table 4. 1** Bond dissociation energy in gas and solution phase for  $\text{C}\equiv\text{N}$  and  $\text{C}=\text{C}$  in AN.

Bond	Gas phase ( $\text{kJ mol}^{-1}$ )	Solution Phase ( $\text{kJ mol}^{-1}$ )
$\text{C}\equiv\text{N}$	482.41	472.76
$\text{C}=\text{C}$	388.03	383.52

The theoretical calculation shows that the BDE of the  $\text{C}\equiv\text{N}$  triple bond is much higher than that of the  $\text{C}=\text{C}$  double bond. Therefore, the  $\text{C}\equiv\text{N}$  group should be intact during the electropolymerization of PAN.

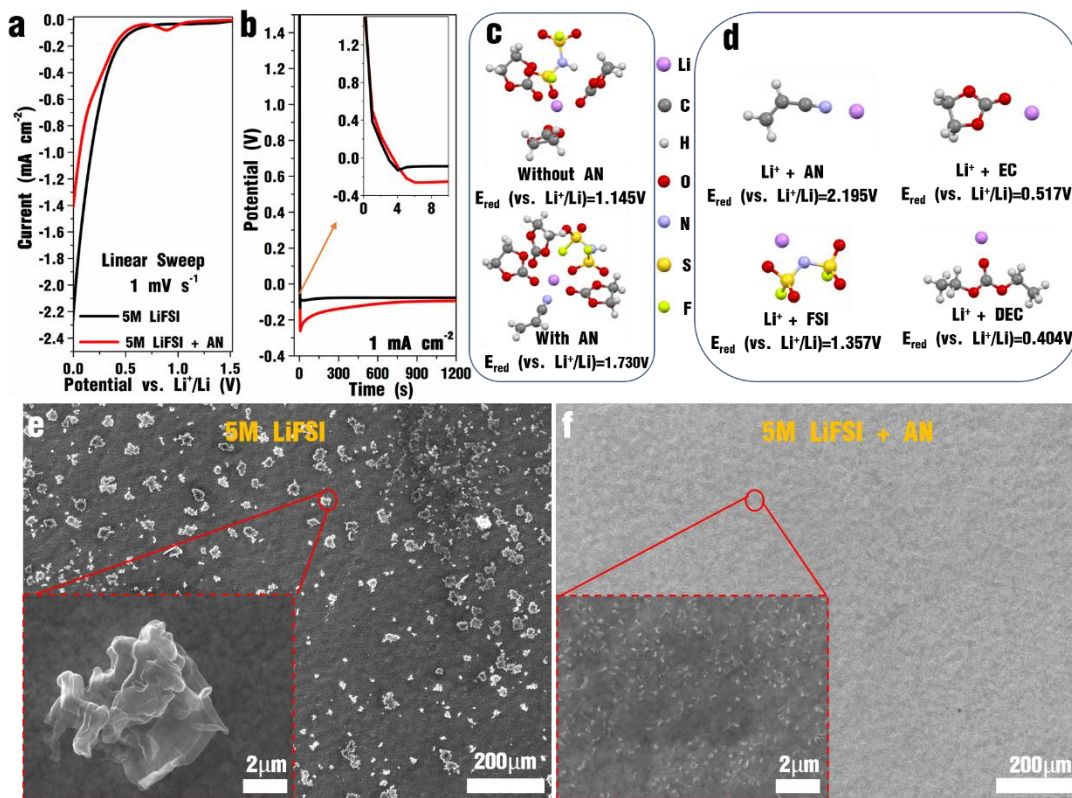


**Figure 4.** (a) Cathodic linear sweep at  $1 \text{ mV s}^{-1}$  scan rate and (b) galvanostatic Li deposition curves at  $1 \text{ mA cm}^{-2}$  in 5 M LiFSI electrolytes without and with AN additive; (c) Calculated reduction potential of the representative  $\text{Li}^+$  solvation structures; (d) Calculated reduction potential of  $\text{Li}^+$ -AN,  $\text{Li}^+$ -EC,  $\text{Li}^+$ -DEC, and  $\text{Li}^+$ -FSI pairs; SEM images of Li deposited on Cu galvanostatically ( $0.05 \text{ mA cm}^{-2}$ ) for 20 minutes in 5 M LiFSI electrolytes (e) without and (f) with AN additive.

To illustrate the effect of the electropolymerized polyacrylonitrile (PAN) SEI on the nucleation of Li deposition, galvanostatic Li deposition under  $0.05 \text{ mA cm}^{-2}$  (low current to minimize concentration polarization) was performed for 20 mins (short deposition to avoid extensive Li growth), and the morphology of the Li nucleation was observed with scanning electron microscope (SEM). As displayed in **Figure. 4.4 e**, the Li nuclei from the electrolyte without AN are bulky, with the size on the order of micrometers and nucleation sites randomly distributed on the substrate. In stark contrast, the Li nuclei from the

electrolyte with AN are much smaller and more uniform as shown in **Figure. 4.4f**. This observation is a strong indication that the in-situ formation of PAN-SEI results to more uniform interfacial current.

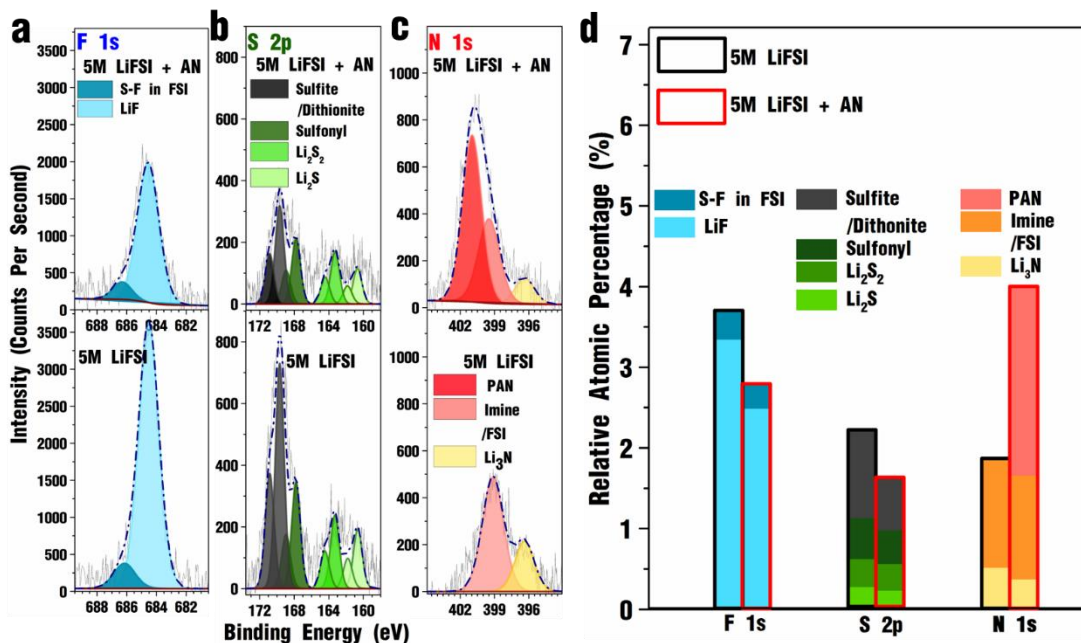


**Figure 4.5** (a) F 1s, (b) S 2p, (c) N 1s XPS spectra, and (d) the atomic percentage of F, S and N after chronopotentiometry at 0.5 V vs. Li<sup>+</sup>/Li in the electrolytes with and without AN additive.

The surface composition of the electropolymerized PAN was analyzed with the X-ray photoelectron spectroscopy (XPS). The reductive chronopotentiometry at 0.5 V vs. Li<sup>+</sup>/Li, which is below the electropolymerization potential of AN identified in **Figure. 4.4a**, was performed for 1 hour in both electrolytes on Cu working electrodes. **Figure. 4.5a** to **5c** display the F 1s, S 2p, and N 1s XPS spectra after the chronopotentiometry. The top panels are the spectra from the electrolyte with AN and the bottom panels are from the electrolyte without AN. The C 1s, and O 1s spectra can be found in **Figure 4.6**.

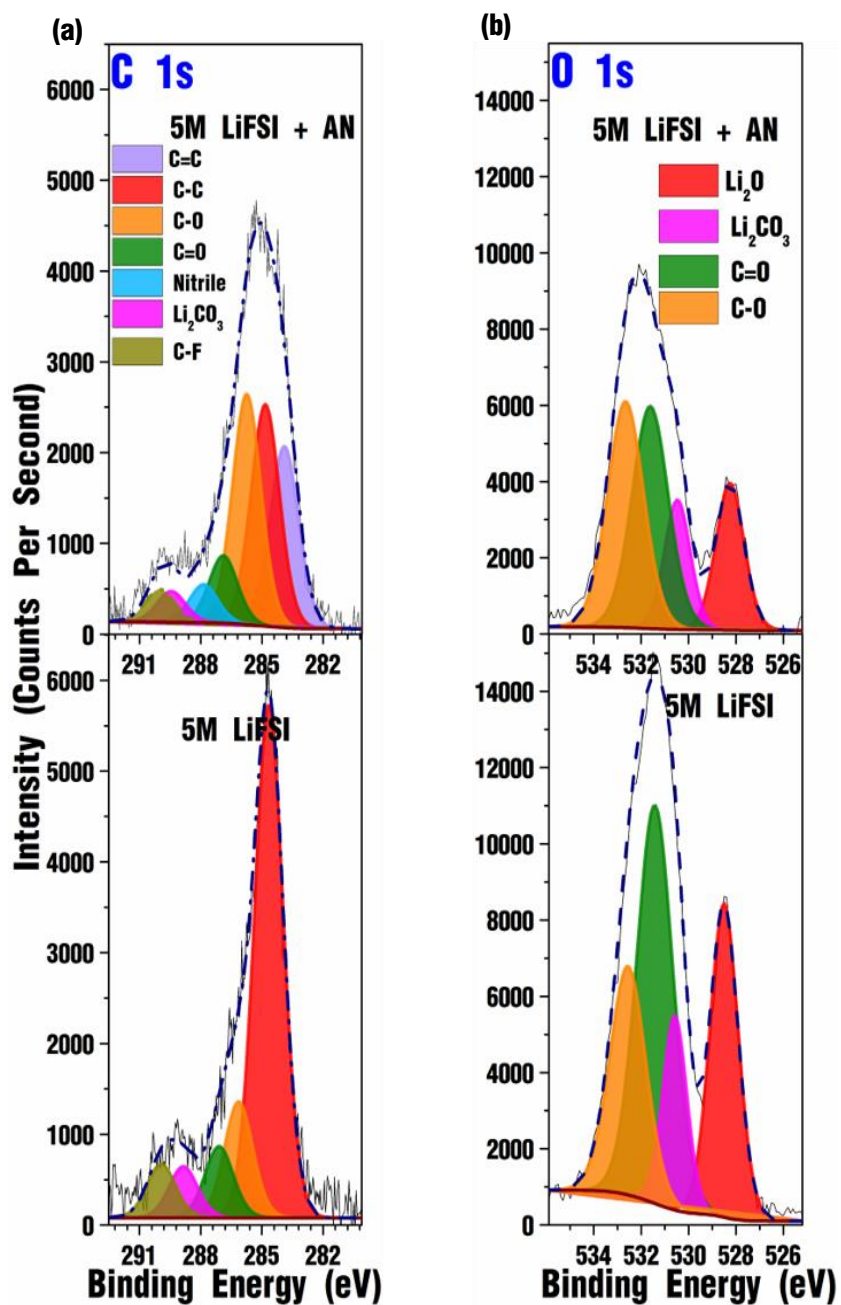


**Figure 4. 6** (a) C 1s and (b) O 1s XPS spectra after chronopotentiometry at 0.5 V vs. Li<sup>+</sup>/Li in the electrolytes with and without AN additive.

The F 1s spectra indicate the F-containing reduction product from both electrolytes is mainly lithium fluoride (LiF) indexed by the peak at 684.5 eV<sup>3</sup>. The S 2p spectra show

reduction products including lithium sulfide ( $\text{Li}_2\text{S}$ ), lithium disulfide ( $\text{Li}_2\text{S}_2$ )<sup>45</sup>, and dithionite or sulfite (169.7 eV)<sup>46</sup> from the decomposition of FSI anions. In the N 1s spectra, in addition to  $\text{Li}_3\text{N}$  (396.5 eV)<sup>47</sup> and the imine compounds (399.2 eV) from the FSI decomposition, the spectrum from the electrolyte with AN shows a distinct peak at 400.8 eV, which is attributed to the  $\text{C}\equiv\text{N}$  group in PAN<sup>48</sup>. As indicated by the atomic ratios of F, S, and N shown in **Figure. 4.5d**, the side products from electrolyte decomposition with AN additive are much less than those from the electrolyte without AN.

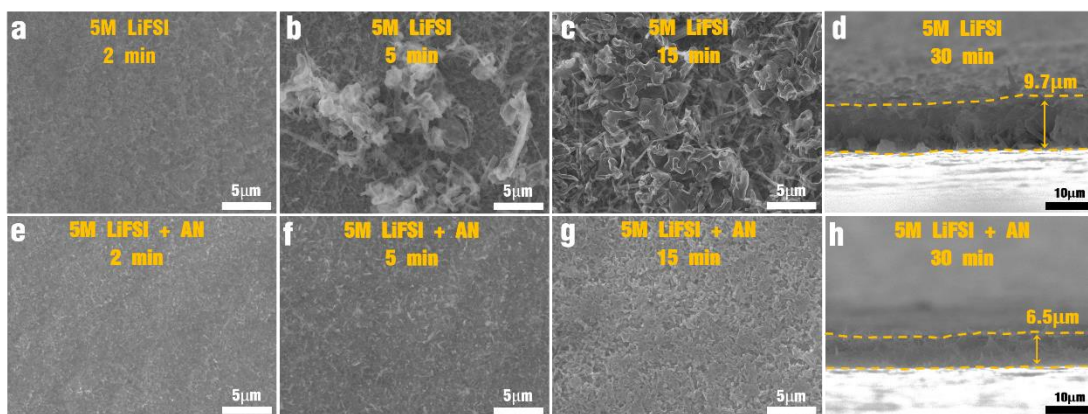


**Figure 4. 7** Top-view SEM images of galvanostatic ( $1\text{mA cm}^{-2}$ ) Li deposition in 5 M LiFSI electrolyte (a-c) without and (e-g) with AN additive after 2 min (a, e), 5min (b, f), and 15min (c, g); Cross-section SEM images showing the thickness of Li deposition in 5 M LiFSI electrolyte (d) without and (h) with AN additive under  $1\text{mA cm}^{-2}$  after 30 min.

The structure and morphology of Li deposition under constant current ( $1\text{ mA cm}^{-2}$ ) as a function of time was characterized with SEM as shown in **Figure. 4.7**. After 2-min deposition (**Figure. 4.7a** and **7e**), the Li deposition from the electrolyte with AN shows distinctly more uniform morphology, which is consistent with the Li nucleation behaviors observed in **Figure. 4.4e** and **4.4f**. After 5-min and 15-min deposition (**Figure.4.7b-3.7c** and **4.7f-4.7g**), the difference in the Li structure becomes more distinct: the Li deposited

from the electrolyte without AN is porous and composed of whiskers; on the other hand, the Li deposited from the electrolyte with AN demonstrates dense and uniform structure, which is validated by the cross-section images in **Figure 4.7d** and **4.7h**: The thickness of the Li deposition after 30 mins in the electrolyte with AN is measured as 6.5  $\mu\text{m}$ , almost 50% thinner than the Li deposited in the electrolyte without AN additive (9.7  $\mu\text{m}$ ). The energy-dispersive X-ray spectroscopy (**Figure 4.8**) confirms the higher N content in the surface of Li deposited from the electrolyte with AN additive.

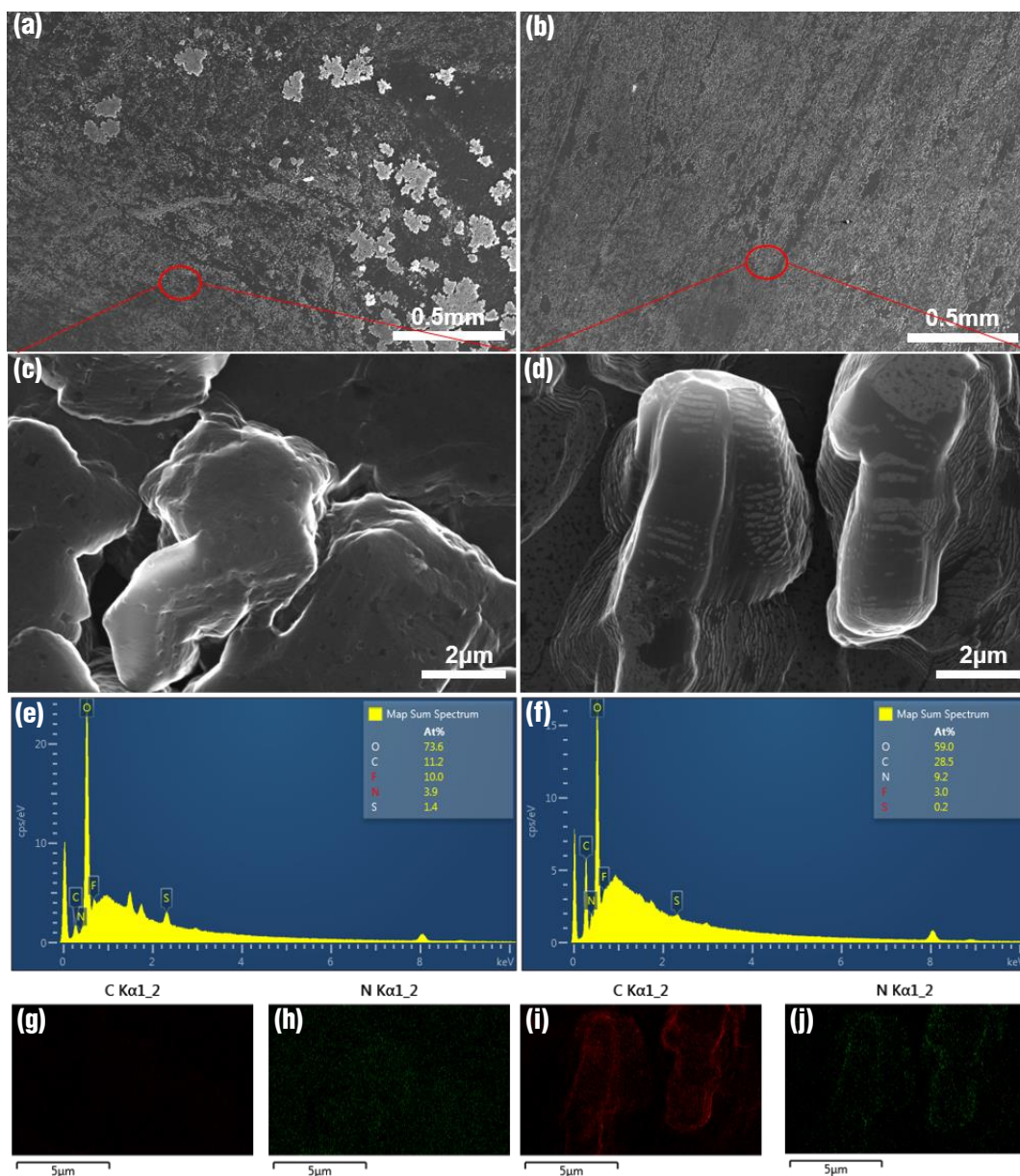


**Figure 4. 8** SEM images of deposited Li anode under constant voltage at -50 mV vs.  $\text{Li}^+/\text{Li}$  for 1 hour in electrolyte with (b, d) and without (a, c) AN additive. The corresponding EDX spectra and elemental mapping of deposited Li anode under constant voltage at -50 mV for 1 hour in electrolyte with (e, g, h) and without (f, I, j) AN additive.

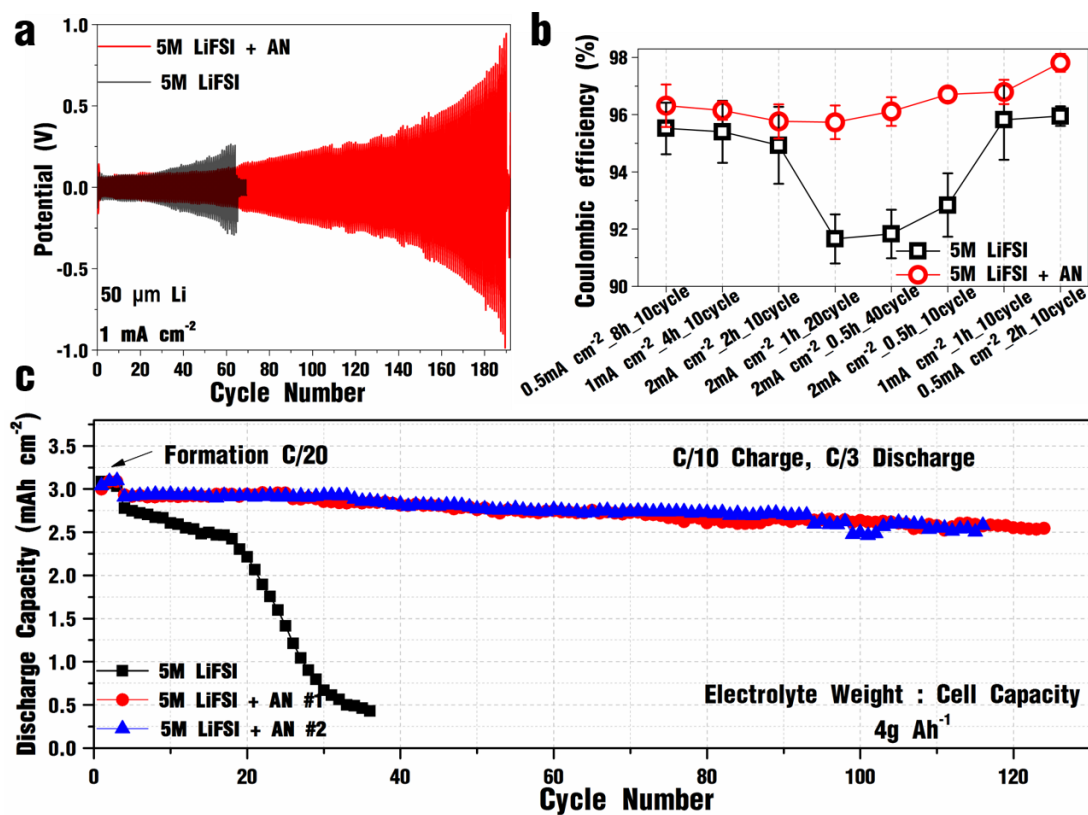


**Figure 4.9** (a) Representative cycling curves of Li||Li symmetric cells in lean electrolyte (30  $\mu\text{L}$ ) under  $1\text{mA cm}^{-2}$  current and  $1\text{mAh cm}^{-2}$  areal capacity; (b) Average CE of Li deposition-stripping in 5 M LiFSI electrolyte with and without AN additive under various cycling conditions (e.g., 0.5  $\text{mA cm}^{-2}$ \_8h\_10cycle means 10 cycles using 0.5  $\text{mA cm}^{-2}$  with 8-h deposition and 8-h stripping); (c) Cycling performance of 0.4 Ah Li||NMC622 pouch cell (50- $\mu\text{m}$  Li anode and 3  $\text{mAh cm}^{-2}$  cathode areal capacity) in lean electrolyte at C/10 charging and C/3 discharging rate.

The uniform and dense Li deposition enabled by AN additive can significantly improve the cycle stability and CE of Li anode. **Figure. 4.9a** shows the comparison of cycling curves of Li||Li symmetric cell with and without AN additive. Thin Li anode (50  $\mu\text{m}$ ) and 30  $\mu\text{L}$  electrolyte was used in the symmetric cells that were cycled at  $1\text{mA cm}^{-2}$  with  $1\text{mAh cm}^{-2}$  areal capacity. The cycle life (end of life defined by the sudden potential drop, i.e., soft short) of the Li||Li symmetric cell with AN additive was almost three times longer than that of the symmetric cell without AN. In addition, the average CE of Li deposition-stripping

shown in **Figure 4.9b** under various cycling parameters (current, deposition/stripping time, and number of cycles) with AN is consistently higher than that without AN. The CEs of Li deposition-stripping as the function of cycle number in Li||Cu cells with 1 mAh cm<sup>-2</sup> areal capacity (0.5 mA cm<sup>-2</sup> and 1 mA cm<sup>-2</sup>) also indicate the superior performance of AN-added electrolyte (**Figure 4.10**).

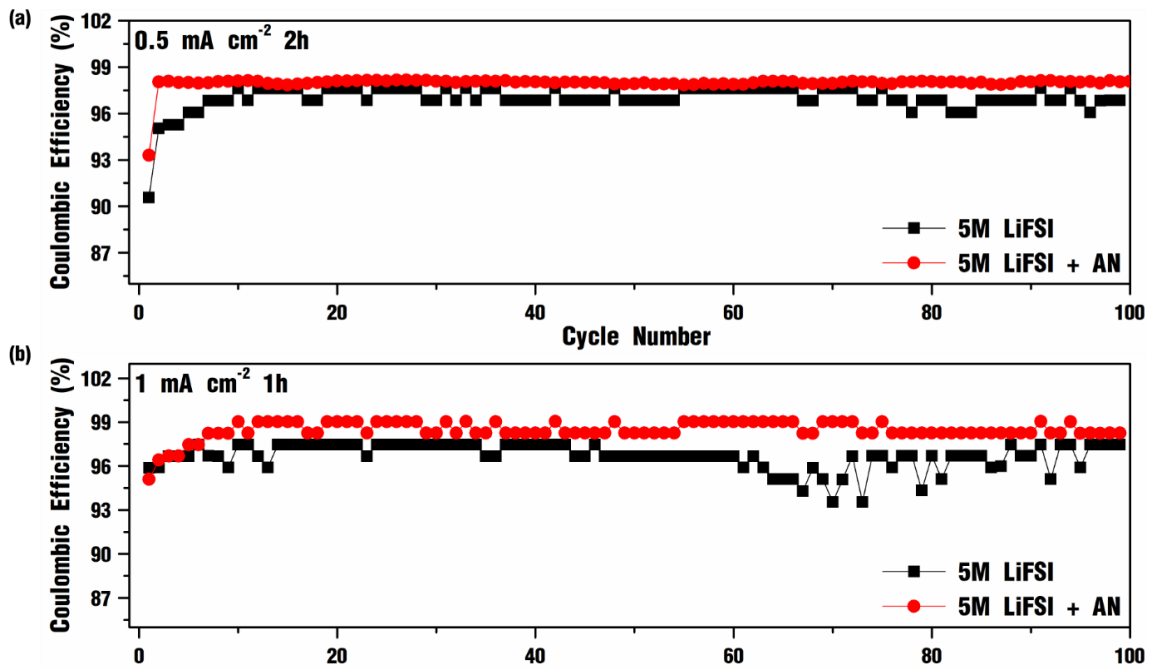


**Figure 4. 10** Li deposition-stripping CE vs. cycle number from Li||Cu cells with 1mAh cm<sup>-2</sup> areal capacity under (a) 0.5mA cm<sup>-2</sup> and (b) 1mA cm<sup>-2</sup> currents.

Li||NMC622 pouch cells with 0.4 Ah capacity were assembled using the 50- $\mu$ m Li anode and NMC622 cathode with areal capacity of 3 mAh cm<sup>-2</sup>. The amount of electrolyte used in the pouch cells is kept at 4 g per Ah, and the cells were discharged at 1 mA cm<sup>-2</sup> (C/3) and charged at 0.3 mA cm<sup>-2</sup> (C/10) after the initial formation cycles (3 cycles at C/20 for both discharge and charge). The specific energy of the 0.4 Ah pouch cell is approximately 245 Wh kg<sup>-1</sup>, and the cell parameters are listed in **Table 4.2**.

**Table 4. 2** Cell parameters of the 0.4Ah Li||NMC622 pouch cell.

	<b>Parameter</b>	<b>Value</b>
NMC622 Cathode	Discharge capacity	180 mAh g <sup>-1</sup>
	Active material loading	90%
	Area capacity (each side)	3.0 mAh cm <sup>-2</sup>
	Electrode thickness (each side)	90 μm
	Number of layers	3
Li anode	Thickness (each side)	50 μm
Electrolyte	E/C ratio	4.0 g Ah <sup>-1</sup>
Cell	Nominal voltage	3.7 V
	Capacity	0.4 Ah
	Cell specific energy density	245Wh kg <sup>-1</sup>
	Dimensions	4 cm × 6 cm

**Figure 4.10c** shows the comparison of cycle stability of the pouch cells using electrolytes with and without AN. The discharge capacity of the Li||NMC622 pouch cell without AN additive quickly decreases after 20 cycles. On the contrary, the pouch cells with AN additive can retain 2.54 mAh cm<sup>-2</sup> capacity (capacity retention: 84.7%) after 120 cycles. It is worth noting that the Li||NMC622 full cells using thick Li metal anode (600 μm) demonstrate identical cycle stability with and without AN additive in **Figure 4.11**. This further demonstrates that AN additive improves the stability of Li anodes with realistic thickness.

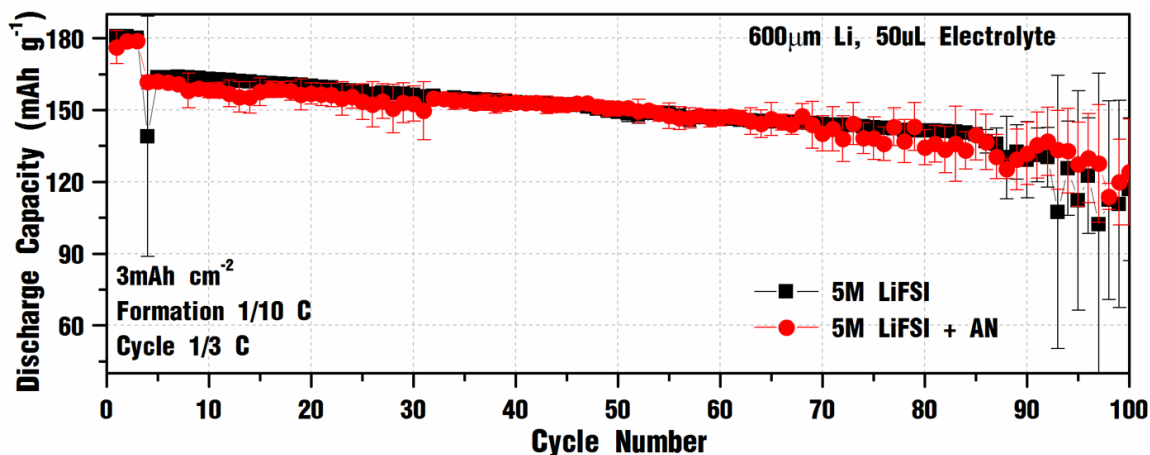
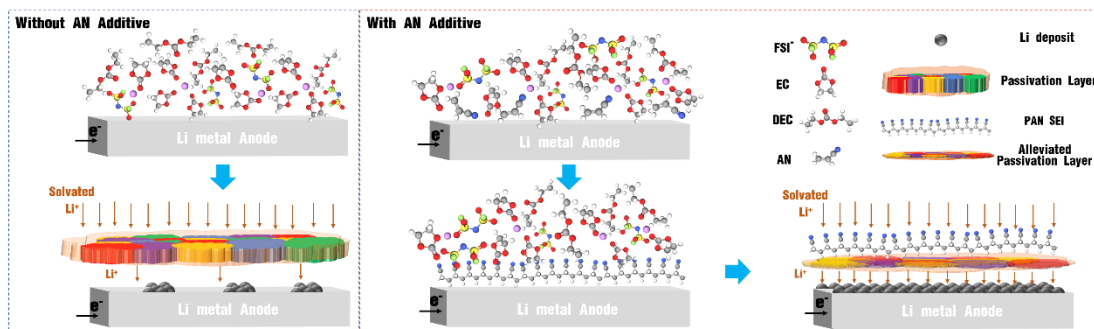


**Figure 4. 11** Electrochemical performance of Li||NMC622 cell using 600- $\mu\text{m}$  Li anode and 50  $\mu\text{L}$  electrolytes with and without AN.



**Scheme 4. 1** The mechanism of uniform Li deposition enabled by the PAN-SEI from in situ electropolymerization of AN additive.

#### 4.4 Conclusion

In this study, we revealed acrylonitrile as an effective electrolyte additive enabling uniform Li deposition with improved coulombic efficiency. As illustrated in **Scheme 4.1**, Li deposition on the Li anode surface without the PAN-SEI results to a severe passivation layer from the decomposition of electrolyte solvents and FSI anions. With the AN additive, PAN is formed by electropolymerization prior to the decomposition of the electrolyte. The PAN-SEI enables the homogeneous distribution of de-solvated Li ions at the interface thus

resulting to uniform Li deposition. The effectiveness of the AN additive is validated by the excellent performance of 0.4 Ah Li||NMC622 pouch cells with realistic cell parameters and operation condition.

## References

- (1) J. Liu, Z. Bao, Y. Cui, E. J. Dufek, J. B. Goodenough, P. Khalifah, Q. Li, B. Y. Liaw, P. Liu, A. Manthiram, Y. S. Meng, V. R. Subramanian, M. F. Toney, V. V. Viswanathan, M. S. Whittingham, J. Xiao, W. Xu, J. Yang, X. Yang, J-G. Zhang, *Nat. Energy* 4 (2019), 180-186.
- (2) P. Albertus, S. Babinec, S. Litzelman, A. Newman, *Nat. Energy* 3 (2018), 16-21.
- (3) J. Zhang, J. Shi, X. Wen, Y. Zhao, J. Guo, *ACS Appl. Mater. Interfaces* 12 (2020), 32863-32870.
- (4) J. Lang, Y. Long, J. Qu, X. Luo, H. Wei, K. Huang, H. Zhang, L. Qi, Q. Zhang, Z. Li, H. Wu, *Energy Storage Mater.* 16 (2019), 85-90.
- (5) J. Xie, L. Liao, Y. Gong, Y. Li, F. Shi, A. Pei, J. Sun, R. Zhang, B. Kong, R. Subbaraman, J. Christensen, Y. Cui, *Sci. Adv.* 3 (2017), eaao3170.
- (6) C. Fu, C. Battaglia, *ACS Appl. Mater. Interfaces* 12 (2020), 41620-41626.
- (7) J. Zhao, L. Liao, F. Shi, T. Lei, G. Chen, A. Pei, J. Sun, K. Yan, G. Zhou, J. Xie, C. Liu, Y. Li, Z. Liang, Z. Bao, Y. Cui, *J. Am. Chem. Soc.* 139 (2017), 11550-11558.
- (8) Z. Peng, N. Zhao, Z. Zhang, H. Wan, H. Lin, M. Liu, C. Shen, H. He, X. Guo, J-G. Zhang, D. Wang, *Nano Energy* 39 (2017), 662-672.
- (9) D. Lin, Y. Liu, W. Chen, G. Zhou, K. Liu, B. Dunn, Y. Cui, *Nano Lett.* 17 (2017), 3731-3737.
- (10) Y. Zhang, W. Wang, H. Tang, W. Bai, X. Ge, X. Wang, C. Gu, J. Tu, *J. Power Sources* 277 (2015), 304-311.
- (11) Y. Li, Y. Sun, A. Pei, K. Chen, A. Vailionis, Y. Li, G. Zheng, J. Sun, Y. Cui, *Acs Cent. Sci.* 4 (2018), 97-104.
- (12) M. Wu, Z. Wen, Y. Liu, X. Wang, L. Huang, *J. Power Sources* 196 (2011), 8091-8097.
- (13) Y. Liu, D. Lin, P. Yuen, K. Liu, J. Xie, R. H. Dauskardt, Y. Cui, *Adv. Mater.* 29 (2017), 1605531.
- (14) R. Khurana, J. L. Schaefer, L. A. Archer, G. W. Coates, *J. Am. Chem. Soc.* 136 (2014), 7395-7402.
- (15) A. A. Assegie, J. Cheng, L. Kuo, W. Su, B. J. Hwang, *Nanoscale* 10 (2018), 6125-6138.

- (16) C. Wang, Y. Yang, X. Liu, H. Zhong, H. Xu, Z. Xu, H. Shao, F. Ding, *ACS Appl. Mater. Interfaces* 9 (2017), 13694-13702.
- (17) W. Zhou, Z. Wang, Y. Pu, Y. Li, S. Xin, X. Li, J. Chen, J. B. Goodenough, *Adv. Mater.* 31 (2019), 1805574.
- (18) D. J. Lee, H. Lee, J. Song, M. H. Ryou, Y. M. Lee, H. T. Kim, J. K. Park, *Electrochem. Commun.* 40 (2014), 45-48.
- (19) H. Lee, D. J. Lee, Y. J. Kim, J. K. Park, H. T. Kim, *J. Power Sources* 284 (2015), 103-108.
- (20) D. J. Lee, H. Lee, Y. J. Kim, J. K. Park, H. T. Kim, *Adv. Mater.* 28 (2016), 857-863.
- (21) M. He, R. Guo, G. M. Hobold, H. Gao, B. M. Gallant, *P. Natl. Acad. Sci. USA* 117 (2020), 73-79.
- (22) A. Rabenau, *Solid State Ionics*, 6 (1982), 277-293.
- (23) X. Zhang, X. Cheng, X. Chen, C. Yan, Q. Zhang, *Adv. Funct. Mater.* 27 (2017), 1605989.
- (24) E. Markevich, G. Salitra, D. Aurbach, *Acs Energy Lett.* 2 (2017), 1337-1345.
- (25) G. M. Veith, M. Doucet, R. L. Sacci, B. Vacaliuc, J. K. Baldwin, J. F. Browning, *Sci. Rep-UK* 7 (2017), 6326.
- (26) K. Schroder, J. Alvarado, T. A. Yersak, J. Li, N. Dudney, L. J. Webb, Y. S. Meng, K. J. Stevenson, *Chem. Mater.* 27 (2015), 5531-5542.
- (27) Y. Yang, J. Xiong, S. Lai, R. Zhou, M. Zhao, H. Geng, Y. Zhang, Y. Fang, C. Li, J. Zhao, *ACS Appl. Mater. Interfaces* 11 (2019), 6118-6125.
- (28) C. Korepp, W. Kern, E. A. Lanzer, P. R. Raimann, J. O. Besenhard, M. Yang, K.-C. Moller, D.-T. Shieh, M. Winter, *J. Power Sources* 174 (2007), 628-631.
- (29) H. J. Santner, C. Korepp, M. Winter, J. O. Besenhard, K.-C. Möller, *Anal. Bioanal. Chem.* 379 (2004), 266-271.
- (30) S. Komaba, T. Itabashi, T. Ohtsuka, H. Groult, N. Kumagai, B. Kaplan, H. Yashiro, *J. Electrochem. Soc.* 152 (2005), 937-946.
- (31) K. C. Moller, H. J. Santner, W. Kern, S. Yamaguchi, J. O. Besenhard, M. Winter, *J. Power Sources* 119 (2003), 561-566.

- (32) Y. Ugata, M. L. Thomas, T. Mandai, K. Ueno, K. Dokko, M. Watanabe, *Phys. Chem. Chem. Phys.* 21 (2019), 9759-9768.
- (33) N. Verdier, D. Lepage, R. Zidani, A. Pr  b  , D. Aym  -Perrot, C. Pellerin, M. Doll  , D. Rochefort, *ACS Appl. Energy Mater.* 3 (2020), 1099-1110.
- (34) P. Hu, J. Chai, Y. Duan, Z. Liu, G. Cui, L. Chen, *J. Mater. Chem. A*, 4 (2016), 10070-10083.
- (35) S. Plimpton, *J. Comput. Phys.* 117 (1995), 1-19.
- (36) L. Martinez, R. Andrade, E. G. Birgin, J. M. Martinez, *J. Comput. Chem.* 30 (2009), 2157-2164.
- (37) K. P. Jensen, W. L. Jorgensen, *J. Chem. Theory Comput.* 2 (2006), 1499-1509.
- (38) K. Shimizu, D. Almantariotis, M. F. C. Gomes, A. A. H. Padua, J. N. C. Lopes, *J. Phys. Chem. B* 114 (2010), 3592-3600.
- (39) M. Valiev, E. J. Bylaska, N. Govind, K. Kowalski, T. P. Straatsma, H. J. J. Van Dam, D. Wang, J. Nieplocha, E. Apra, T. L. Windus, W. de Jong, *Comput. Phys. Commun.* 181 (2010), 1477-1489.
- (40) C. I. Bayly, P. Cieplak, W. D. Cornell, P. A. Kollman, *J. Phys. Chem-Us* 97 (1993), 10269-10280.
- (41) S. Plimpton, R. Pollock, M. Stevens, In *Proceedings of the Eighth SIAM Conference on Parallel Processing for Scientific Computing*, 1997.
- (42) T. Hou, G. Yang, N. N. Rajput, J. Self, S. W. Park, J. Nanda, K. A. Persson, *Nano Energy* 64 (2019), 103881.
- (43) O. Borodin, M. Olguin, P. Ganesh, P. R. C. Kent, J. L. Allen, W. A. Henderson, *Phys. Chem. Chem. Phys.* 18 (2016), 164-175.
- (44) A. Klamt, G. Schuurmann, *J. Chem. Soc. Perk T.* 2 5 (1993), 799-805.
- (45) C. Fu, G. Li, J. Zhang, B. Cornejo, S. Piao, K. N. Bozhilov, R. C. Haddon, J. Guo, *Acs Energy Lett.* 1 (2016), 115-120.
- (46) R. Jay, A. W. Tomich, J. Zhang, Y. Zhao, A. De Gorostiza, V. Lavallo, J. Guo, *ACS Appl. Mater. Interfaces* 11 (2019), 11414-11420.
- (47) H. Xu, Y. Li, A. Zhou, N. Wu, S. Xin, Z. Li, J. B. Goodenough, *Nano Lett.* 18 (2018), 7414-7418.

- (48) T. Takahagi, I. Shimada, M. Fukuhara, K. Morita, A. Ishitani, *J. Polym. Sci. Pol. Chem.* 24 (1986), 3101-3107.

## **Chapter 5: Electrodes/electrolyte interphases stabilization of Li metal battery by phosphorus pentoxide additive in LiPF<sub>6</sub> electrolyte**

### **5.1 Introduction**

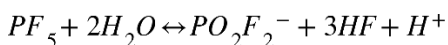
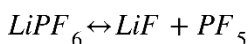
Li metal batteries with high energy density has become the most promising next generation lithium-ion batteries. However, the short cycle life and safety issue hindered its commercialization. LiPF<sub>6</sub> containing electrolyte, which is the most widely used electrolyte in Li ion batteries, is not compatible with Li metal batteries. The major drawback originates from the undesirable autocatalytic decomposition reaction to form lithium fluoride (LiF) and phosphorus pentafluoride (PF<sub>5</sub>), the subsequent hydrolysis process of PF<sub>5</sub> will react with traces of moisture to form HF<sup>(1)-(4)</sup> The resulting HF can degrade electrode materials and electrolyte. The corrosive HF will attack Li metal and then form corrosion pits. It is easily to generate highly resistive LiF passivation layer on Li metal anode, which resulting in the nonuniform electrodeposition process.<sup>(5)</sup> Furthermore, the decomposition reaction of SEI components and HF will trigger the continuous electrolyte decomposition.<sup>(6),(7)</sup> In addition, transition metal dissolution<sup>(8),(9)</sup> and cathode (high Ni content NMC) particle cracking problem<sup>(10)</sup> could result from the presence of HF.

The aforementioned problems were resulting from hydrolysis reaction between the decomposition product of LiPF<sub>6</sub>, the PF<sub>5</sub>, and the trace amount of moisture to form HF.

So, the strategies for stabilizing the LiPF<sub>6</sub> electrolyte could coming from: improving the dissociation of LiPF<sub>6</sub>, which suppress the equilibrium decomposition to form PF<sub>5</sub> and

screening the scavenger additives to eliminate PF<sub>5</sub>, H<sub>2</sub>O, and HF for LiPF<sub>6</sub> based electrolyte system.

The origin of LiPO<sub>2</sub>F<sub>2</sub> in 1M LiPF<sub>6</sub> in carbonate electrolyte (baseline electrolyte) was resulting from the hydrolysis of PF<sub>5</sub> (decomposition from LiPF<sub>6</sub>) with the trace amount of water as shown in the following reactions:<sup>(11)-(14)</sup>



It has been widely studied in J. R. Dahn's group for the effect of LiPO<sub>2</sub>F<sub>2</sub> enhancing the electrochemical performance for Li-ion batteries. They thoroughly studied the impact of extra amount of water on Li-ion batteries consists of LiCoO<sub>2</sub> positive electrode with graphite<sup>(15)</sup> or Lithium titanate negative electrode.<sup>(16)</sup> It was found that the extra amount of water would not negatively affect cell performance (except for cell swelling), and it will increase the capacity retention in some cases. In addition, it was also found that the extra amount of water in the baseline electrolyte does improve the deposition of Li for Li metal batteries.<sup>(17)</sup> The morphology of Li deposition changed from randomly mossy structure to well-ordered structure consists of compactly growth Li rods.

Later, it has been reported the positive effect of extra amount of water in the baseline electrolyte was owing to the formation of extra amount of LiPO<sub>2</sub>F<sub>2</sub><sup>(18)</sup>, since the HF was detrimental for the cathode degradation.<sup>(19),(20)</sup> The following research about the additional LiPO<sub>2</sub>F<sub>2</sub> additive on the performance of Li batteries has been studied.

Chengyuan *et. al*<sup>(21)</sup> found although electrolyte ionic conductivity would decrease with the increasing amount of LiPO<sub>2</sub>F<sub>2</sub> additive from 6.34 mS. cm<sup>-1</sup> (1M LiPF<sub>6</sub> EC/DEC (1:3 wt%)) to 5.72 mS. cm<sup>-1</sup> (1M LiPF<sub>6</sub> EC/DEC (1:3 wt%) +2wt% LiPO<sub>2</sub>F<sub>2</sub>), the anodic stability of the electrolyte (against Pt electrode) increased from ~4.6 V (1M LiPF<sub>6</sub> EC/DEC (1:3 wt%)) to ~5.5 V ((1M LiPF<sub>6</sub> EC/DEC (1:3 wt%))+1wt% LiPO<sub>2</sub>F<sub>2</sub>). Moreover, the capacity retention, long term coulombic efficiency and high-rate performance have been improved with LiPO<sub>2</sub>F<sub>2</sub> additive. The parasitic reaction rates have been suppressed together with the improved cell cycle lifetime with the LiPO<sub>2</sub>F<sub>2</sub> additive.<sup>(22)</sup> Jiawei Chen *et. al*<sup>(23)</sup> pointed the protective low impedance CEI on cathode generated by the film forming LiPO<sub>2</sub>F<sub>2</sub> additive, and this film effectively hindered the electrolyte oxidation, electrode structure destruction, leading to the dramatically improvement of cycle stability of Li||LNCM cells. The Lewis acids<sup>(24)</sup> are able to enhance the dissociation of LiPF<sub>6</sub> by forming the complex with PF<sub>6</sub><sup>-</sup>. The PF<sub>5</sub> can be effectively scavenged by the compounds with P, O, N with lone pair electrons like trimethyl phosphite<sup>(25)</sup> It has been reported that H<sub>2</sub>O in LiPF<sub>6</sub> based electrolyte can be effectively scavenged by Lewis bases additives with specific structure including: Si-N<sup>(26),(27)</sup>, Si-O<sup>(28)</sup>, phosphite<sup>(29)</sup>, and isocyanate moieties.<sup>(30)</sup> HF can be effectively scavenged by the compounds with electron donating sites<sup>(31)</sup> like amino silanes<sup>(32)</sup> and phosphites<sup>(33)</sup>.

P<sub>2</sub>O<sub>5</sub> is a well-known dehydrating agent and acid scavenger, and the hydrolysis product, phosphite, can effectively enhancing the dissociation of LiPF<sub>6</sub> to suppress the PF<sub>5</sub> hydrolysis.<sup>(24)</sup> In this study, we investigate P<sub>2</sub>O<sub>5</sub> as additive to stabilize the electrolyte/electrodes interphases by mitigate the HF based side reactions. The P<sub>2</sub>O<sub>5</sub>

additive not only improve the Li metal deposition morphology for denser deposition layer, but also alleviate the transition metal dissolution and NMC622 particle cracking problems. Thus, the full cell performance has been greatly improved.

## 5.2 Stabilization of Li metal anode/electrolyte interphase by P<sub>2</sub>O<sub>5</sub> additive

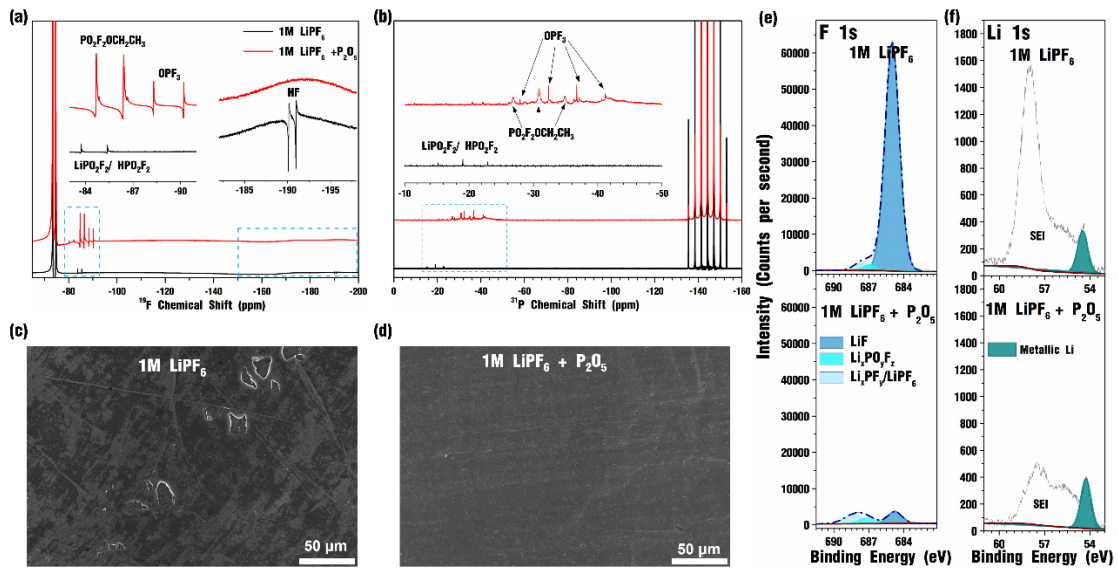


**Figure 5. 1** (a) <sup>19</sup>F and (b) <sup>31</sup>P NMR spectra of 1M LiPF<sub>6</sub> electrolyte without and with P<sub>2</sub>O<sub>5</sub> additive. SEM image of Li metal electrode after soaking in 1M LiPF<sub>6</sub> electrolyte (c) without and (d) with P<sub>2</sub>O<sub>5</sub> additive for 2 days, and the corresponding (e) F 1s and (f) Li 1s XPS spectra.

The effectiveness of P<sub>2</sub>O<sub>5</sub> additive for the absorption of HF acid can be found in <sup>19</sup>F NMR spectra **Figure 5. 1**(a), which indicated no HF (-190.58 ppm)<sup>(13),(14)</sup> existing in of 1M LiPF<sub>6</sub> electrolyte with P<sub>2</sub>O<sub>5</sub> additive. The compound in the electrolyte was identified by matching the peak position and the coupling constant from literature<sup>(11),(13),(14)</sup>, and listed in **Table 5.1**. The <sup>19</sup>F spectra consists of the several typical doublets with chemical shifts:  $\delta$  (<sup>19</sup>F) = -74.01 ppm ( $J(^{19}\text{F}-^{31}\text{P})=708.5$  Hz) that is assigned to PF<sub>6</sub><sup>-</sup>;  $\delta$  (<sup>19</sup>F) = -84.56 ppm ( $J(^{19}\text{F}-^{31}\text{P})=930.4$  Hz) that is assigned to PO<sub>2</sub>F<sub>2</sub><sup>-</sup> (HPO<sub>2</sub>F<sub>2</sub>);  $\delta$  (<sup>19</sup>F) = -85.56 ppm ( $J(^{19}\text{F}-^{31}\text{P})=973.0$  Hz) that is assigned to PO<sub>2</sub>F<sub>2</sub><sup>-</sup> (PO<sub>2</sub>F<sub>2</sub>OCH<sub>2</sub>CH<sub>3</sub>);  $\delta$  (<sup>19</sup>F) = -89.26 ppm ( $J(^{19}\text{F}-^{31}\text{P})=1068.2$

Hz) that is assigned to OPF<sub>3</sub>;  $\delta(^{19}\text{F}) = -190.58$  ppm ( $J(^{19}\text{F}-^{31}\text{P})=481.4$  Hz) that is assigned to HF.

The corresponding <sup>31</sup>P NMR spectra consists of: a septet with  $\delta(^{31}\text{P}) = -144.28$  ppm ( $J(^{19}\text{F}-^{31}\text{P})=708.3$  Hz) that is assigned to PF<sub>6</sub><sup>-</sup>; a triplet with  $\delta(^{31}\text{P}) = -19.5$  ppm ( $J(^{19}\text{F}-^{31}\text{P})=929.8$  Hz) that is assigned to PO<sub>2</sub>F<sub>2</sub><sup>-</sup>(HPO<sub>2</sub>F<sub>2</sub>); a triplet with  $\delta(^{31}\text{P}) = -30.94$  ppm ( $J(^{19}\text{F}-^{31}\text{P})=973.4$  Hz) that is assigned to PO<sub>2</sub>F<sub>2</sub><sup>-</sup>(PO<sub>2</sub>F<sub>2</sub>OCH<sub>2</sub>CH<sub>3</sub>); a quartet with  $\delta(^{31}\text{P}) = -32.34$  ppm ( $J(^{19}\text{F}-^{31}\text{P})=1068.5$  Hz) that is assigned to OPF<sub>3</sub>.

**Table 5. 1** <sup>19</sup>F and <sup>31</sup>P NMR spectra data of 1M LiPF<sub>6</sub> electrolyte without and with P<sub>2</sub>O<sub>5</sub> additive.

Compound	$\delta(^{19}\text{F})/(\text{ppm}), (J(^{19}\text{F}-^{31}\text{P}))$	$\delta(^{31}\text{P})/(\text{ppm}), (J(^{19}\text{F}-^{31}\text{P}))$
PF <sub>6</sub> <sup>-</sup>	-74.01 (d, 708.5 Hz)	-144.28 (sept, 708.3 Hz)
PO <sub>2</sub> F <sub>2</sub> <sup>-</sup> (LiPO <sub>2</sub> F <sub>2</sub> /HPO <sub>2</sub> F <sub>2</sub> )	-84.56 (d, 930.4 Hz)	-19.5 (t, 929.8 Hz)
PO <sub>2</sub> F <sub>2</sub> <sup>-</sup> (PO <sub>2</sub> F <sub>2</sub> OCH <sub>2</sub> CH <sub>3</sub> )	-85.56 (d, 973.0 Hz)	-30.94 (t, 973.4 Hz)
OPF <sub>3</sub>	-89.26 (d, 1068.2 Hz)	-32.34 (q, 1068.5 Hz)
HF	-190.58 (d, 481.4 Hz, $J(^1\text{H}-^{19}\text{F})$ )	

d: doublet; t: triplet; q: quartet; sept: septet

Thus, the Li metal corrosion problem has been mitigated, which can be find in **Figure 5.**

1d. The clear corrosion pits on Li metal anode after soaking in 1M LiPF<sub>6</sub> electrolyte for 2 days is observed in the **Figure 5. 1c**, while with the help of P<sub>2</sub>O<sub>5</sub> additive, the Li metal surface remains almost the same. The corresponding F 1s XPS spectra (in **Figure 5. 1e**) indicates large amount of LiF (684.5 eV)<sup>(5),(34)</sup> is formed on Li metal anode when corrosion happened in 1M LiPF<sub>6</sub> electrolyte. In addition, the thickness of the SEI is alleviated since

the ratio of SEI peak and metallic Li peak (54.8 eV)<sup>(35),(36)</sup> (in Fig. 1f) is decreased when applying P<sub>2</sub>O<sub>5</sub> additive.

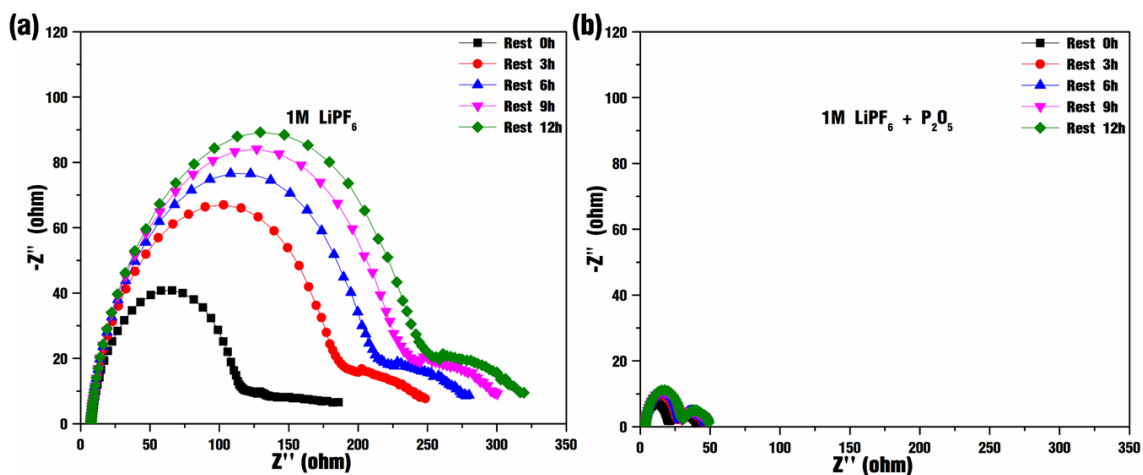


**Figure 5. 2** Nyquist plots at different rest time for Li||Li symmetric cell in 1M LiPF<sub>6</sub> electrolyte (a) without and (b) P<sub>2</sub>O<sub>5</sub> additive.

Consequently, the more stable Li metal anode surface against the electrolyte lead to smaller resistance of the Li metal anode as shown in **Figure 5.2b**, and the increasingly growth resistance (in **Figure 5.2a**) indicates the continuously corrosion reaction happened on Li metal anode with 1M LiPF<sub>6</sub> electrolyte.

### 5.3 Uniform Li deposition layer enabled by P<sub>2</sub>O<sub>5</sub> additive

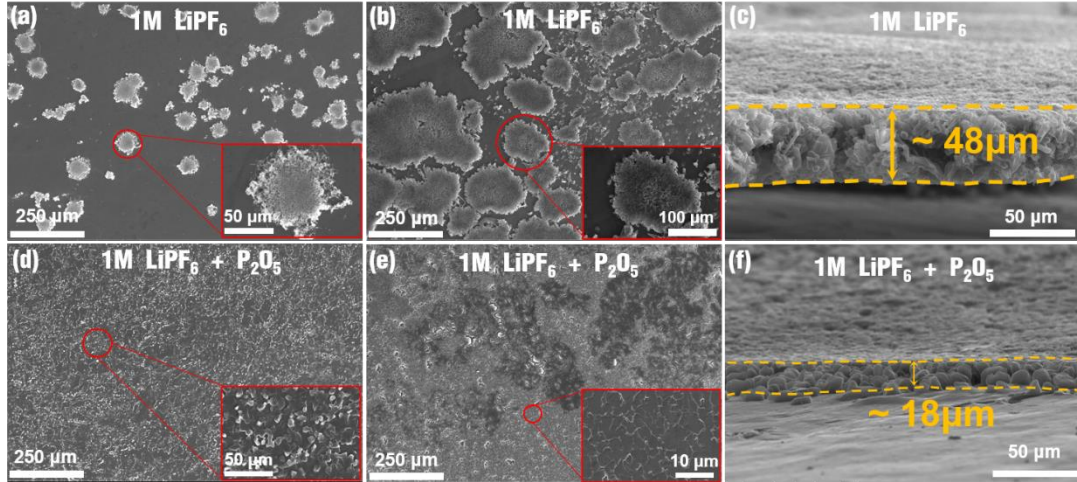


**Figure 5. 3 .** Top view SEM images of Li deposited on Li metal galvanostatically ( $0.3\text{mA cm}^{-2}$ ) for (a and d) 1 hour and (b, e) 10 hours in  $1\text{M LiPF}_6$  electrolyte (a-c) without and (d-f) with  $\text{P}_2\text{O}_5$  additive. Cross-sectional SEM images of Li deposition layer galvanostatically ( $0.3\text{mA cm}^{-2}$ ) for 10 hours in  $1\text{M LiPF}_6$  electrolyte (c) without and (f) with  $\text{P}_2\text{O}_5$  additive.

Our previous work has found the cleaner Li metal surface, the better Li metal nucleation.<sup>Error! Reference source not found.</sup> A salient difference between  $1\text{M LiPF}_6$  electrolyte with and without additive can be anticipated in the morphology of the Li deposits. By comparing the nucleation stage of Li metal deposits in **Figure 5. 2a** and **2d**, the Li nucleation density in  $1\text{M LiPF}_6$  with  $\text{P}_2\text{O}_5$  additive is greatly improved in addition with the more uniform size distribution. Although  $1\text{M LiPF}_6$  electrolyte can generate much higher intensity of LiF on Li metal surface (in **Figure 5. 1e**), the exposed pitting area would favor the Li nucleation and deposition process thus lower the nucleation density and cause the porous Li deposition layer.<sup>(5)</sup>

In the long-term deposition process, the Li deposition layer (in **Figure 5. 2b**) in  $1\text{M LiPF}_6$  electrolyte is discrete which is because of the low nucleation density, while the Li deposition layer (in **Figure 5. 2e**) is much more homogeneous and denser when applying

$P_2O_5$  additive. The thickness of  $3mAh\ cm^{-2}$  (theoretical thickness:  $15\ \mu m$ ) Li deposition layer is reduced from  $48\ \mu m$  (in **Figure 5. 2c**) to  $18\ \mu m$  (in **Figure 5. 2f**) with the help of  $P_2O_5$  additive.

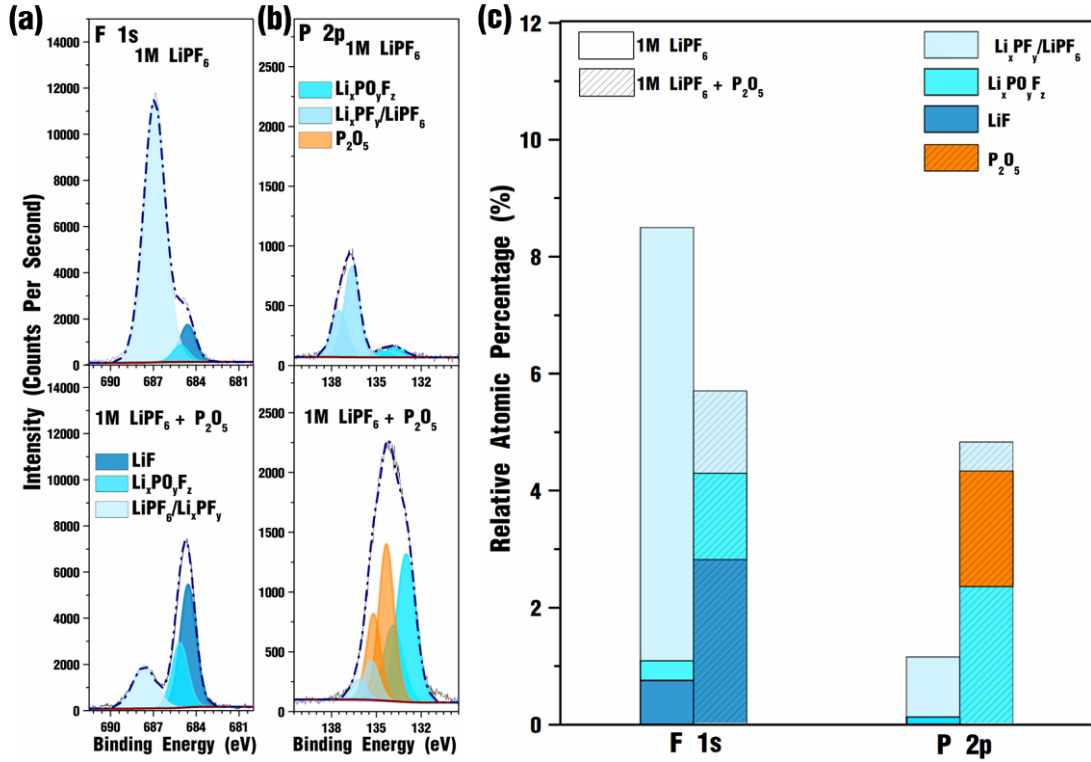


**Figure 5. 4** (a) F 1s, (b) P 2p XPS spectra, and (c) the relative atomic percentage of F and P on Li metal foil after galvanostatically ( $0.3mA\ cm^{-2}$ ) for 10 hours in 1M LiPF<sub>6</sub> electrolyte without and with P<sub>2</sub>O<sub>5</sub> additive.

The SEI properties also played an important role for the uniform and dense deposition layer.<sup>(38)-(40)</sup> From **Figure 5. 3a**, much higher intensity of LiF ( $684.5\ eV$ )<sup>(5),(34)</sup> and Li<sub>x</sub>PO<sub>y</sub>F<sub>z</sub> ( $685.5\ eV$ )<sup>(41)-(43)</sup> and less intensity of organic SEI components (in **Figure 5.5**) were generated during Li deposition in 1M LiPF<sub>6</sub> electrolyte with P<sub>2</sub>O<sub>5</sub> additive.

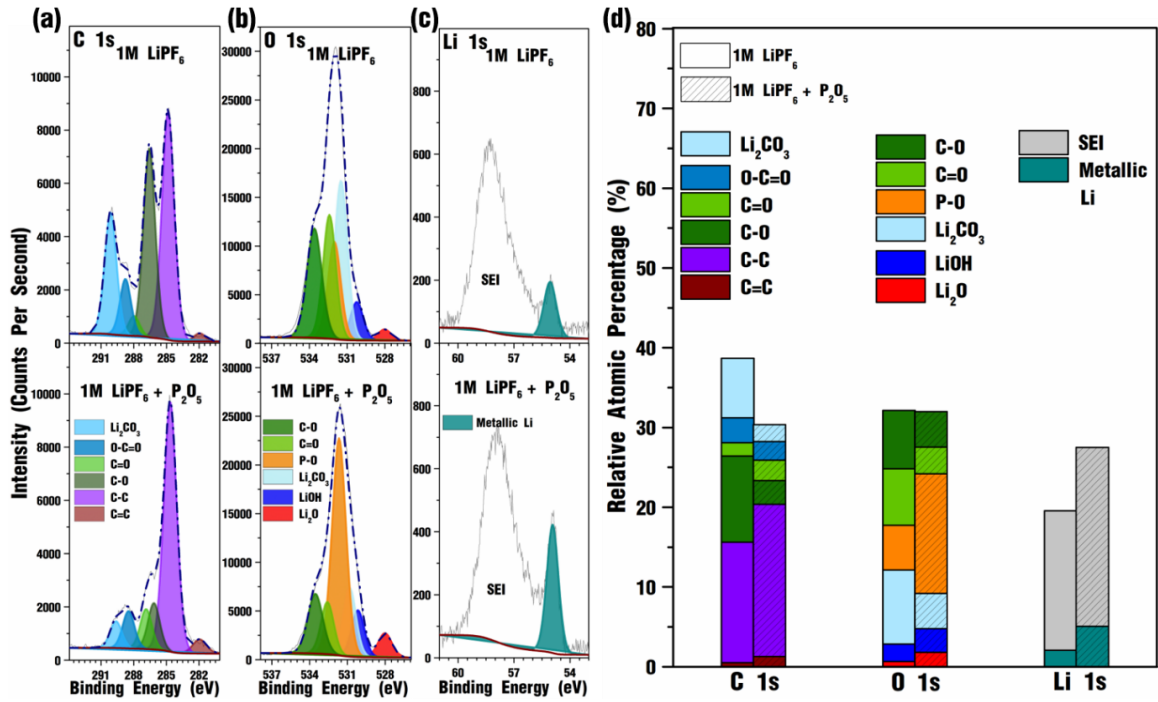


**Figure 5.5** (a) C 1s, (b) O 1s, (c) Li 1s XPS spectra, and (d) the relative atomic percentage of C, O, and Li on Li metal foil after galvanostatically ( $0.3\text{mA cm}^{-2}$ ) for 10 hours in 1M LiPF<sub>6</sub> electrolyte without and with P<sub>2</sub>O<sub>5</sub> additive.

These indicate the 1M LiPF<sub>6</sub> electrolyte with P<sub>2</sub>O<sub>5</sub> will electrochemically generate more stable ceramic SEI than the electrolyte without additive. The higher SEI repair rate was beneficial for smooth Li deposition.<sup>(44)</sup>

## 5.4 Superior electrochemical performance and the working mechanism of $P_2O_5$ additive

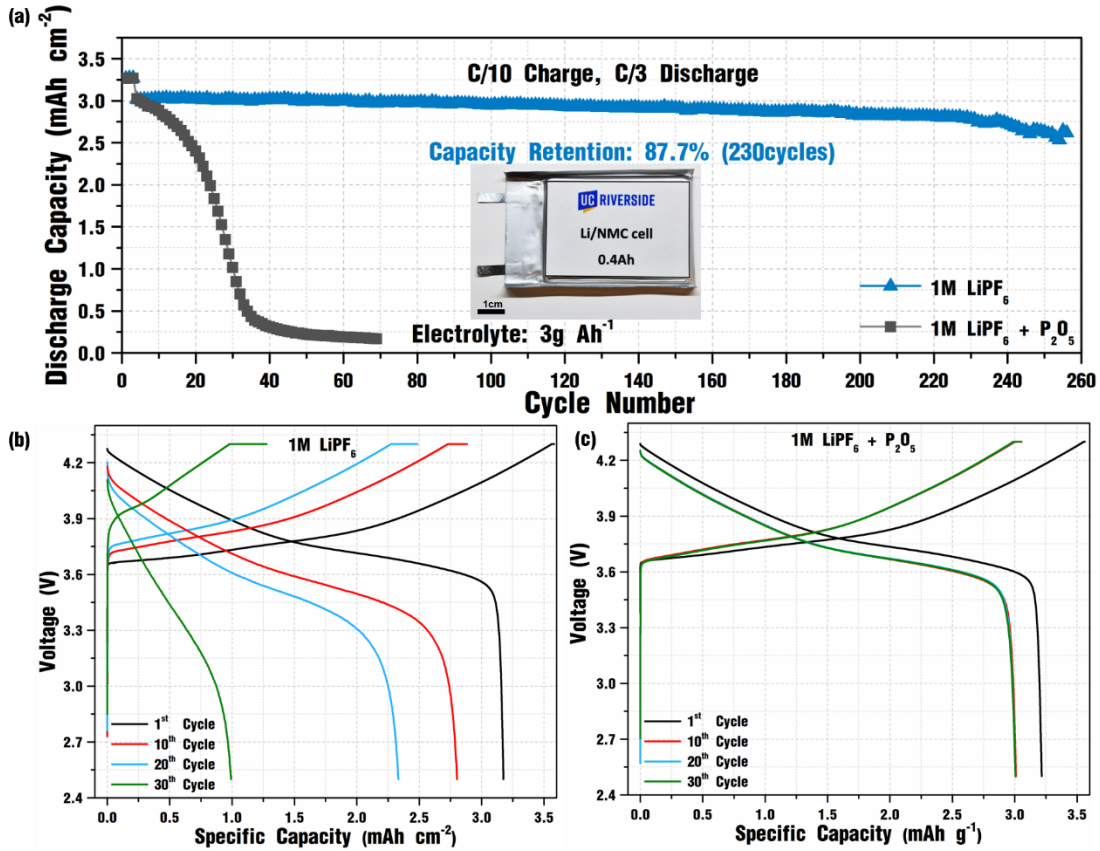


**Figure 5. 6** (a) Cycling performance of 0.4 Ah Li||NMC622 pouch cell (50  $\mu$ m Li anode and 3mAh cm<sup>-2</sup> cathode areal capacity) in lean electrolyte (electrolyte to capacity ratio = 3g Ah<sup>-1</sup>) at C/10 charging and C/3 discharging. Optical image of the 0.4Ah Li||NMC622 pouch cell was inserted in **Figure 5. 4(a)**. Cell voltage profile for 0.4 Ah Li||NMC622 pouch cell in 1M LiPF<sub>6</sub> electrolyte (a) without and (b) with P<sub>2</sub>O<sub>5</sub> additive.

With the help of P<sub>2</sub>O<sub>5</sub> additive, the cycle life of 0.4 Ah Li||NMC622 pouch cell has been improved (in **Figure 5. 4a**) from 30 cycles to more than 200 cycles with capacity retention of 87.7% (230 cycles). The increasingly growth of the cell polarization from 1<sup>st</sup> cycle to 30<sup>th</sup> cycle is observed in the voltage profile of 1M LiPF<sub>6</sub> electrolyte in **Figure 5. 4b**, while the voltage profile almost remains the same for 1M LiPF<sub>6</sub> electrolyte with P<sub>2</sub>O<sub>5</sub> additive in

**Figure 5. 4c.** The corresponding  $dQ/dV$  vs. voltage profile (in **Figure 5. 5a-c**) has been plotted in order to compare the polarization of the cell. The peak voltage shift of  $dQ/dV$  plot can be regarded as the change of the cell overall polarization.<sup>(45)</sup> From **Figure 5. 5a-c**, the major redox peak for the cell testing in 1M  $\text{LiPF}_6$  electrolyte shifted to higher voltages (from 3.76 V—1<sup>st</sup> cycle to 3.96 V—30<sup>th</sup> cycle) for charging process and shifted to lower voltages (from 3.71 V—1<sup>st</sup> cycle to 3.27 V—30<sup>th</sup> cycle) for discharging process, which indicated the higher degree of polarization of the cell.

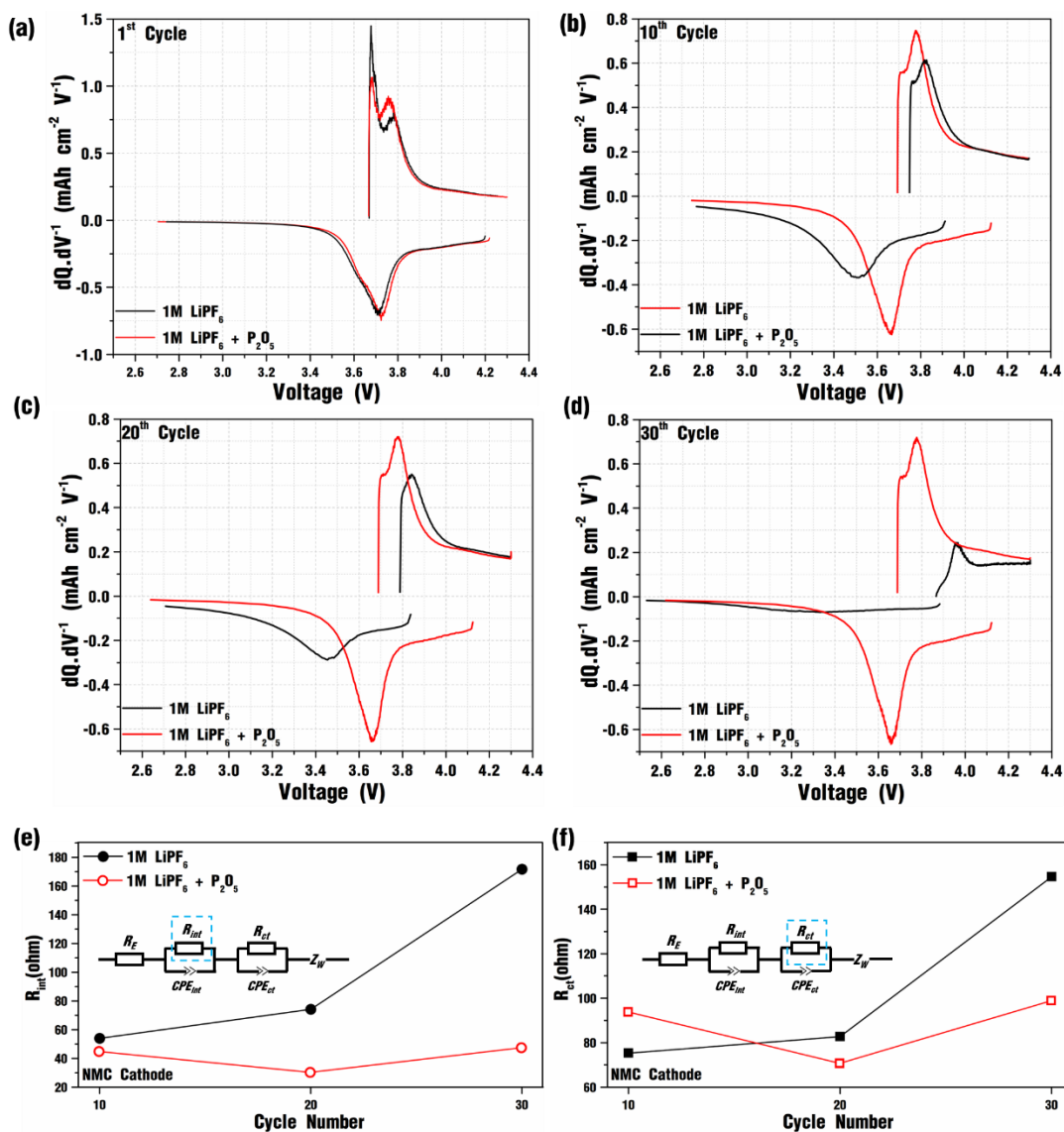


**Figure 5. 7** dQ/dV vs. voltage plot of the comparison between 1M LiPF<sub>6</sub> electrolyte without and with P<sub>2</sub>O<sub>5</sub> additive in (a) 1<sup>st</sup> cycle, (b) 10<sup>th</sup> cycle, (c) 20<sup>th</sup> cycle, and (d) 30<sup>th</sup> cycle. Deconvoluted EIS analysis of (e) interfacial resistance and (f) charge transfer resistance versus cycle number in different electrolyte.

The overall polarization of the cell could be contributed from ohmic, charge transfer and diffusion related effects. In order to deconvolute the origin of the polarization, the EIS analysis on NMC622 cathode and Li metal anode was conducted by using symmetric cells after the cells testing.<sup>(46),(47)</sup> After cycling, two cells in the same condition were

disassembled, and the electrodes with same polarity were paired with new separator and electrolyte to reassemble the NMC622||NMC622 symmetric cells and Li||Li symmetric cells for the testing of EIS on NMC622 cathode and Li metal anode, respectively.

The EIS analysis on NMC622 cathode indicated the resistance of NMC622 cathode continuously increasing during cycling in 1M LiPF<sub>6</sub> electrolyte in Figure. S4a. However, the resistance of NMC622 cathode remained almost the same during cycling when using 1M LiPF<sub>6</sub> electrolyte with P<sub>2</sub>O<sub>5</sub> additive in Figure. S4b. The equivalent circuit is used to fit the EIS data, which is shown in the insert of Fig 5d and 5e, consists of 6 circuit elements as follows. The ohmic resistance of the system, R<sub>E</sub>, was the intercept at high frequency. The first semi-circle consists of interfacial resistance, R<sub>int</sub>, and its corresponding capacitance, CPE<sub>int</sub>. The second semi-circle is attributed to the charge transfer resistance, R<sub>ct</sub>, and its corresponding capacitance, CPE<sub>ct</sub>. The low frequency region included the Warburg impedance, Z<sub>w</sub>.<sup>(48)</sup> From the deconvoluted EIS data, both R<sub>int</sub> and R<sub>ct</sub> increasingly grows with cycle number for 1M LiPF<sub>6</sub> electrolyte, while those values slightly change for 1M LiPF<sub>6</sub> with P<sub>2</sub>O<sub>5</sub> additive. The R<sub>int</sub> for 1M LiPF<sub>6</sub> has increased to 171.7 Ω at 30<sup>th</sup> cycle, while that for 1M LiPF<sub>6</sub> with P<sub>2</sub>O<sub>5</sub> additive was 47.11 Ω. The R<sub>ct</sub> for 1M LiPF<sub>6</sub> has increased to 154.6 Ω at 30<sup>th</sup> cycle, while that for 1M LiPF<sub>6</sub> with P<sub>2</sub>O<sub>5</sub> additive was 98.84 Ω. The resistance of Li metal anode (in **Figure 5.8**)<sup>(49)</sup> continuously decreasing with cycle number no matter in which electrolyte.

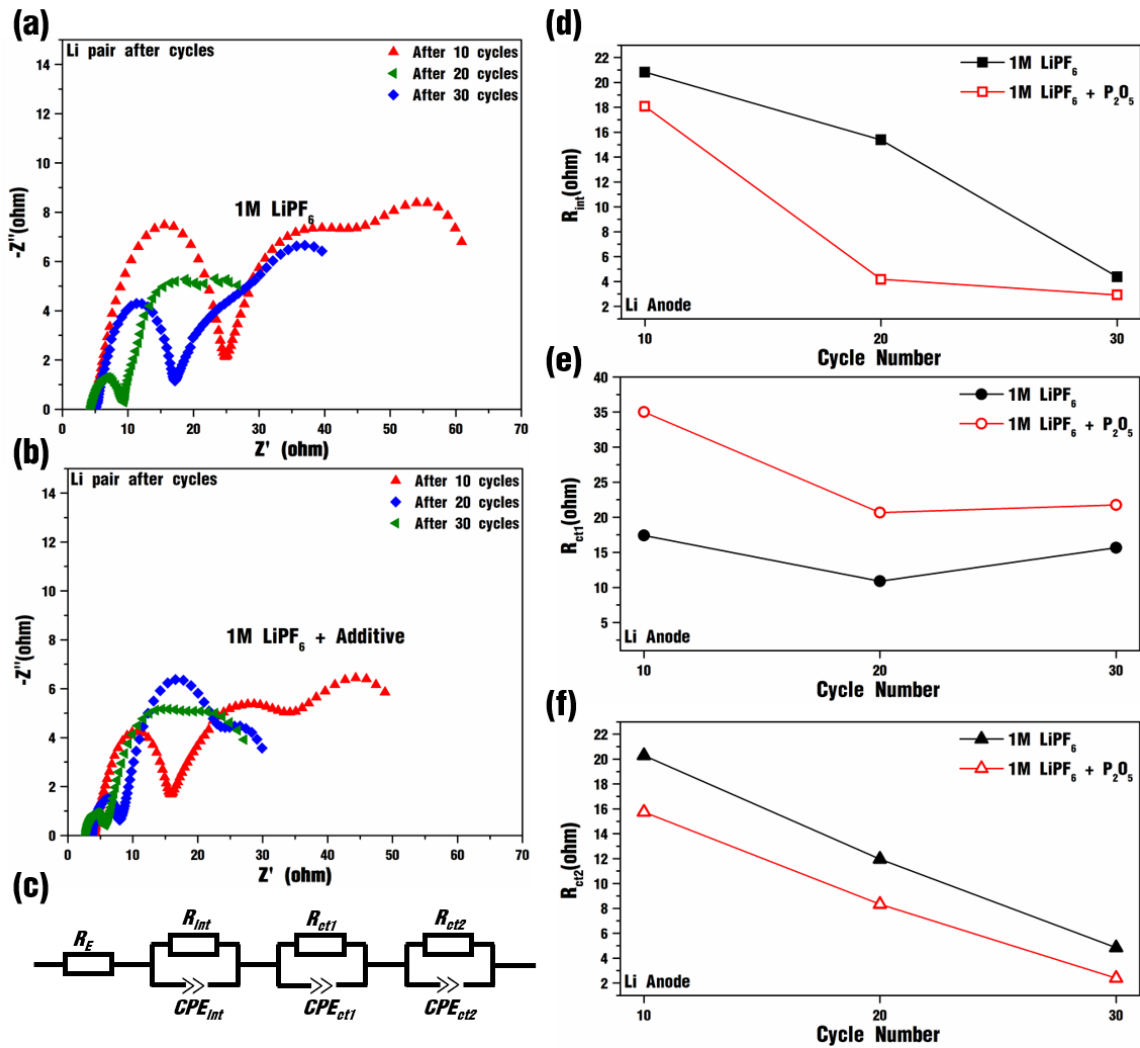


**Figure 5. 8** Nyquist plots for reassembled Li||Li symmetric cell using Li metal anodes after cycling in Li||NMC622 full cells using (a) 1M LiPF<sub>6</sub> electrolyte without and (b) with P<sub>2</sub>O<sub>5</sub> additive. (c) schematic illustration of the impedance fitting model for reassembled Li||Li symmetric cell. EIS fitted (d) interfacial resistance, (e) charge transfer resistance ( $R_{ct1}$ ) and (f) charge transfer resistance ( $R_{ct2}$ ) vs. cycle number for reassembled Li||Li symmetric cells in different electrolytes.

And the resistance difference is far less than that on cathode side, which indicated the major polarization of the cell was coming from the NMC622 cathode.

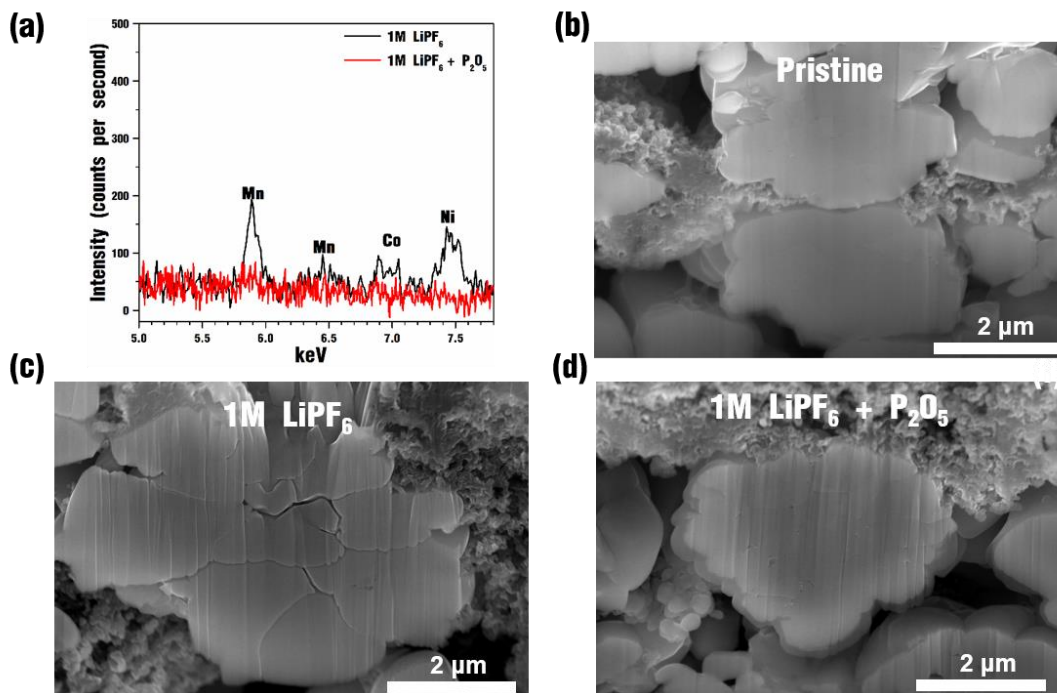


**Figure 5.9 .** (a) EDS spectra of Li metal anode and FIB-SEM images of (b) pristine NMC622 particles, and the NMC622 material after 30 cycles under C/10 charge and C/3 discharge in 1M LiPF<sub>6</sub> electrolyte (c) without and (d) with P<sub>2</sub>O<sub>5</sub> additive.

P<sub>2</sub>O<sub>5</sub> additive not only improved the Li deposition process, but also stabilized NMC622 cathode during cycling. The transition metal dissolution is a major problem for 1M LiPF<sub>6</sub> electrolyte system because of the corrosive HF can dissolve TM<sup>2+</sup> (TM= Co, Ni, Mn) and the EDS analysis result (in **Figure 5. 6a**) shown the distinct evidence.<sup>(8),(9),(50)</sup> After 30 cycles in 1M LiPF<sub>6</sub> electrolyte, Li metal anode has a significant content of transition metal including: Mn, Co and Ni. In contrast, transition metal dissolution problem has been completely suppressed in the presence of P<sub>2</sub>O<sub>5</sub> additive, as presented by the absence of Mn, Co and Ni signal in the EDS spectrum of Li metal anode after 30 cycles in 1M LiPF<sub>6</sub> electrolyte with P<sub>2</sub>O<sub>5</sub> additive. The effect of the deposited transition metal species on Li metal deposition has been thoroughly studied,<sup>(50)</sup> which indicates that the TM

dissolution and deposition would contribute the worse Li deposition behavior in the baseline electrolyte.

The cracking problem for high Ni content cathode material is the dominant reason for the capacity fading. **Figure 5.** 6c and 6d demonstrate the FIB-SEM images of NMC622 particles before and after 30 cycles in 1M LiPF<sub>6</sub> electrolyte without and with P<sub>2</sub>O<sub>5</sub> additive. The distinct cracks (in **Figure 5.** 6c) are observed on NMC622 particles after 30 cycles in 1M LiPF<sub>6</sub>, while the NMC622 particles remained the same after 30 cycles in 1M LiPF<sub>6</sub> with P<sub>2</sub>O<sub>5</sub> additive in **Figure 5.** 6d. And the cracking issue could be the reason for the increasingly growth of cathode resistance, since the precipitation of TMF<sub>2</sub> (TM = Co, Ni and Mn) on the exposed cracking surface.<sup>(10)</sup>

## 5.5 Conclusion

In this study, we revealed phosphorus pentoxide (P<sub>2</sub>O<sub>5</sub>) as an effective electrolyte to stabilize the electrolyte/electrodes interphases. P<sub>2</sub>O<sub>5</sub> additive not only enabling uniform Li deposition but also mitigate the transition metal dissolution and NMC622 particle cracking problems. The effectiveness of P<sub>2</sub>O<sub>5</sub> additive is validated by the excellent performance of Li||NMC622 pouch cells with realistic cell parameters and operation condition.

## 5.6 Methods

### 5.6.1 Materials

The baseline electrolyte of 1M LiPF<sub>6</sub> in the mixture of EC/DEC =50:50 (V/V), battery grade was purchased from Sigma-Aldrich. P<sub>2</sub>O<sub>5</sub> (≥99.99%, trace metal basis, Sigma-Aldrich) was dried under vacuum at 80°C inside argon-filled glovebox for 24 hours prior

to use. The single crystal  $\text{LiNi}_{0.6}\text{Mn}_{0.2}\text{Co}_{0.2}\text{O}_2$  (NMC622) was purchased from Targray Technology International Inc..

### **5.6.2 Electrodes preparation for coin-cells and pouch cells**

The lab-made thin Li foil (50  $\mu\text{m}$  in thickness) was prepared using a previously reported method.<sup>Error! Reference source not found.</sup> The double-side Li metal anode was prepared by sandwiching a copper foil (9  $\mu\text{m}$ , MTI Corporation) with two pieces of lab-made Li metal foil (50  $\mu\text{m}$  in thickness), and pressed with a mechanical roller. The cathode slurry was prepared by mixing 90 wt.% NMC622, 5 wt.% carbon black (Supper C65), and 5 wt.% polyvinylidene fluoride (PVDF, Sigma-Aldrich, Mw~534,000) in N-Methyl-2-pyrrolidone (NMP, Anhydrous, 99.5%, Sigma-Aldrich) through centrifugal mixer (Thinky, AR-100) for 15 mins. All the materials in the slurry preparation except NMP were dried under vacuum at 70°C for 24 hours prior to use. NMP were dried with the 3Å molecular sieves prior to use. The weight ratio of liquid to solid in the slurry was 1.65. The slurry was coated with an automatic tape casting coater (MTI corporation) onto an aluminum current collector (16 $\mu\text{m}$ , Gelon LIB Group) with the film applicator set to 300  $\mu\text{m}$  to make 3 mAh  $\text{cm}^{-2}$  NMC622 cathode. The coated electrodes were transferred into the glovebox and dried at room temperature for 12 hours. Then the electrodes were dried under vacuum inside glovebox at 120°C for 12 hours prior to use. The thickness of electrodes (90  $\mu\text{m}$  for single side) were controlled by calendaring process through mechanic roller. Single-sided and double-sided cathodes were prepared for coin cells and pouch cells, respectively.

### 5.6.3 Cell assembly and electrochemical experiments

CR-2016 type coin cells (Gelon LIB Group) were used in the measurements of the Li||Li symmetric cell cycle stability. Celgard-2400 was used as the separator. Pouch cell were assembled inside an argon-filled glovebox. The amount of electrolyte in the pouch cells was kept at  $3 \text{ g Ah}^{-1}$ . A lab-made pouch cell test holder (**Figure 5.10**) was used during cycling.

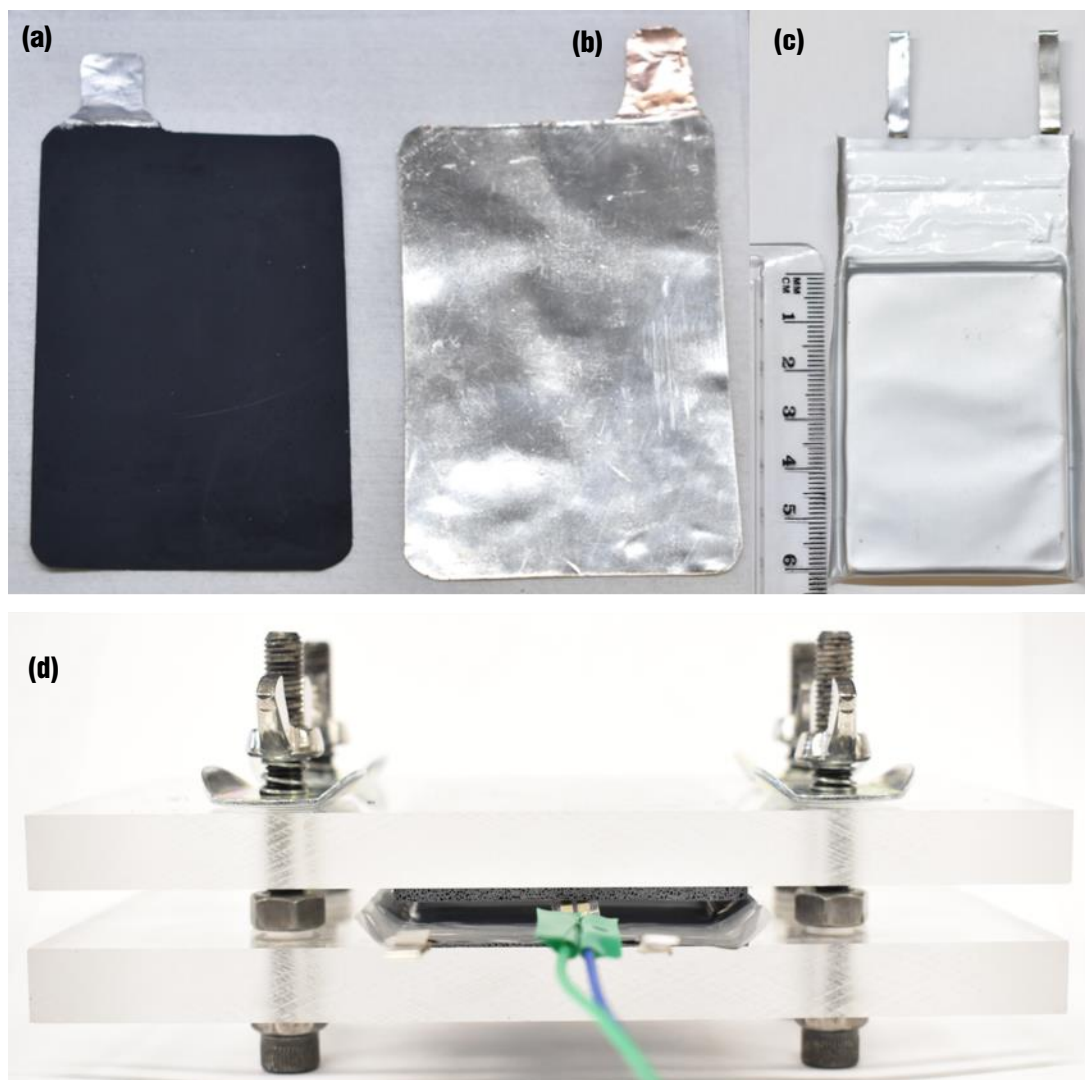


**Figure 5. 10** Optical images of (a) NMC622 electrode (3.8 cm × 5.9 cm), (b) Li metal anode (4.0 cm × 6.0 cm), (c) assembled pouch cell, and (d) testing holder for Li||NMC622 pouch cells.

The cycling experiments were performed with Neware battery testers. All the Li||NMC622 cells were tested under galvanostatically charging to 4.3 V and then hold the voltage at 4.3 V until the current dropped less than  $C/30$ . After that, galvanostatically discharging the cell until voltage less than 2.5 V. The C rate for formation cycles were kept  $C/20$  for charging

and discharging. After formation cycles, using C/10 for charging and C/3 for discharging. And all the constant voltage holding until the current less than C/30.

#### 5.6.4 Average coulombic efficiency measurement

CR-2016 type coin cells were used to measure the average coulombic efficiency: a lab-made Li foil with the thickness around 50  $\mu\text{m}$  was first weighed and then pressed to a Cu substrate as the working electrode. Then pairing with a piece of cathode made of NMC622 and adding electrolyte (3g  $\text{Ah}^{-1}$ ) to assembly the Li metal cell. After a set number of cycles, the remaining Li on the working electrode would be measured by assembling the Li||Li symmetric cell, which consists of the cycled Li metal anode and another identically made Li electrode without weighing. The remaining Li on the working electrode was completely stripped using a 0.3  $\text{mA cm}^{-2}$  current until the stripping cutoff potential (1 V) was reached.

The Li metal consumption rate could be calculated by the following equations:

$$k_{Li} = \frac{Q_{Con}}{Q_{Discharging}}$$

$$Q_{Con} = Q_{original} - Q_{remaining} = m_{Li} \times 3.86 - I_{Strip} \times T_{Strip}$$

$$Q_{Discharging} = \sum_{1,2,\dots,i} Q_{Discharging}^i$$

where  $k_{Li}$  is the Li consumption rate,  $Q_{Con}$  is the total capacity of Li consumed during cycling,  $Q_{original}$  is the original Li source capacity,  $m_{Li}$  is the original weight of Li metal foil ( $\sim 50 \mu\text{m}$ ), 3.86 is the specific capacity of Li metal ( $\sim 3.86 \text{ mAh g}^{-1}$ ),  $I_{Strip}$  is the stripping current for the Li||Li symmetric cell,  $T_{Strip}$  is the total stripping time after the stripping

voltage reaches 1V,  $Q_{Discharging}$  is the cell total discharging capacity during the cycling,  $Q_{Discharging}^i$  is the cell discharging capacity of the  $i^{\text{th}}$  cycle.

Take an example of the Li||NMC622 cell with the weighted Li metal foil of 5.32mg. The total discharging capacity is 0.1165Ah, the total stripping time is 31.9h under the stripping current of 0.3mAh  $\text{cm}^{-2}$  (5/8 inch in diameter for Li metal electrode). The calculated Li consumption rate is 1.389%, which means there will be Li consumed (1.389% of the total discharging capacity on average) from original Li source in each cycle.

#### **5.6.5 Li||Li, NMC622||NMC622 symmetric cells for EIS test**

The Li||NMC622 coin cells were cycling after certain cycles. For each specific cycles, two cells were tested. After cycling, two cells were disassembled and the same electrodes were reassembled to make Li||Li, NMC622||NMC622 symmetric cells with another separator and refilling electrolyte. The EIS measurements were conducted using the Gamry potentiostat Interface 1000, scanning over the frequency range from  $10^6$  Hz to 0.01 Hz with 2 mV amplitude. The EIS data was analyzed by ZSim software to deconvolute the circuit elements using equivalent circuit model.

#### **5.6.6 SEM, EDS and FIB**

The surface morphology and the thickness of the electrode were characterized using scanning electron microscope (SEM, Nova Nano S450, 10 kV). The samples were retrieved in an argon-filled glovebox and washed with dimethyl carbonate thoroughly to remove the residual electrolyte. Prior to the SEM characterization, the samples were dried at room temperature for 24 hours inside the argon-filled glovebox. The samples were then

transported to the SEM facility inside a stainless-steel tube with KF-flange sealing. The samples were loaded in the SEM using a glove-bag with argon purging gas without exposing to ambient environment. The elemental mapping of the samples was collected using an Energy Dispersive X-ray (EDX) spectrometer coupled with the SEM. The focused ion beam (Quanta™ 3D 200i with Ga liquid metal ion source) was used to precisely prepare the cross-sectional image of the NMC622 cathode particles. The ion gun voltage was set to 30 kV, and the current was 30 nA and 7 nA for bulk milling and polishing current, respectively.

### 5.6.7 XPS

X-ray photoelectron spectroscopy (XPS) data were collected using Kratos AXIS Supra (Al K $\alpha$ =1486.7 eV) at UC Irvine Materials Research Institute (IMRI). The samples were prepared following the same procedure for SEM samples. The samples were transported to the XPS facility inside a stainless-steel tube with KF flange sealing filled with argon. Finally, the samples were loaded in the sample chamber in the glovebox integrated with Kratos AXIS Supra for XPS analysis. All peaks of XPS data were analyzed by Casa XPS<sup>52</sup> and calibrated with the reference peak of C 1s at 284.6 eV (the adventitious carbon).

**Table 5. 2** Relative sensitivity factors for Karatos AXIS.

<b>C 1s</b>	<b>O1s</b>	<b>F 1s</b>	<b>S 2p</b>	<b>N 1s</b>	<b>Li 1s</b>
0.278	0.736	1	0.723	0.477	0.025

The relative atomic ratio was calculated by the following equation:

$$RA_i = \frac{A_i/S_i}{\sum A_i/S_i} \times 100\%$$

$RA_i$ : relative atomic ratio of component i

$A_i$ : Area of the deconvoluted peak of component i

$S_i$ : relative sensitivity factor for component i

## References

- (1) Aravindan, V., Gnanaraj, J., Madhavi, S. & Liu, H. K. Lithium-ion conducting electrolyte salts for lithium batteries. *Chem-Eur J* **17**, 14326-14346, (2011).
- (2) Kawamura, T., Okada, S. & Yamaki, J. Decomposition reaction of LiPF<sub>6</sub>-based electrolytes for lithium ion cells. *J. Power Sources* **156**, 547-554, (2006).
- (3) Lux, S. F. *et al.* The mechanism of HF formation in LiPF<sub>6</sub> based organic carbonate electrolytes. *Electrochem. Commun.* **14**, 47-50, (2012).
- (4) Terborg, L. *et al.* Ion chromatographic determination of hydrolysis products of hexafluorophosphate salts in aqueous solution. *Anal. Chim. Acta* **714**, 121-126, (2012).
- (5) Zhang, J., Shi, J. Y., Wen, X. Y., Zhao, Y. F. & Guo, J. C. Properties of thin lithium metal electrodes in carbonate electrolytes with realistic parameters. *ACS Appl. Mater. Inter.* **12**, 32863-32870 (2020).
- (6) Parimalam, B. S., MacIntosh, A. D., Kadam, R. & Lucht, B. L. Decomposition reactions of anode solid electrolyte interphase (SEI) components with LiPF<sub>6</sub>. *J. Phys. Chem. C* **121**, 22733-22738, (2017).
- (7) Agubra, V. A. & Fergus, J. W. The formation and stability of the solid electrolyte interface on the graphite anode. *J. Power Sources* **268**, 153-162, (2014).
- (8) Vetter, J. *et al.* Ageing mechanisms in lithium-ion batteries. *J. Power Sources* **147**, 269-281, (2005).
- (9) Zhan, C., Wu, T. P., Lu, J. & Amine, K. Dissolution, migration, and deposition of transition metal ions in Li-ion batteries exemplified by Mn-based cathodes - a critical review. *Energ. Environ. Sci.* **11**, 243-257, (2018).
- (10) Schipper, F., Erickson, E. M., Erk, C., Shin, J. Y., Chesneau, F. F., & Aurbach, D. Recent advances and remaining challenges for lithium ion battery cathodes I. nickel-rich, LiNi<sub>x</sub>Co<sub>y</sub>Mn<sub>z</sub>O<sub>2</sub>. *J. Electrochem. Soc.* **164**, A6220, (2016).
- (11) Plakhotnyk, A. V., Ernst, L. & Schmutzler, R. Hydrolysis in the system LiPF<sub>6</sub>-propylene carbonate-dimethyl carbonate-H<sub>2</sub>O. *J Fluorine Chem* **126**, 27-31, (2005).
- (12) Campion, C. L., Li, W. T. & Lucht, B. L. Thermal decomposition of LiPF<sub>6</sub>-based electrolytes for lithium-ion batteries. *J Electrochem Soc* **152**, A2327-A2334, (2005).

- (13) Wiemers-Meyer, S., Winter, M. & Nowak, S. Mechanistic insights into lithium ion battery electrolyte degradation - a quantitative NMR study. *Phys Chem Chem Phys* **18**, 26595-26601, (2016).
- (14) Rinkel, B. L. D., Hall, D. S., Temprano, I. & Grey, C. P. Electrolyte Oxidation Pathways in Lithium-Ion Batteries. *J Am Chem Soc* **142**, 15058-15074, (2020).
- (15) Burns, J. C. *et al.* The Impact of Intentionally Added Water to the Electrolyte of Li-ion Cells. *J Electrochem Soc* **160**, A2281-A2287, (2013).
- (16) Burns, J. C. *et al.* The Impact of Intentionally Added Water to the Electrolyte of Li-Ion Cells II. Cells with Lithium Titanate Negative Electrodes. *J Electrochem Soc* **161**, A247-A255, (2014).
- (17) Qian, J. F. *et al.* Dendrite-free Li deposition using trace-amounts of water as an electrolyte additive. *Nano Energy* **15**, 135-144, (2015).
- (18) Xiong, D. J., Petibon, R., Madec, L., Hall, D. S., & Dahn, J. R. Some Effects of Intentionally Added Water on LiCoO<sub>2</sub>/Graphite Pouch Cells. *J Electrochemical Society*, **163**, A1678, (2016).
- (19) Vetter, J. *et al.* Ageing mechanisms in lithium-ion batteries. *J Power Sources* **147**, 269-281, (2005).
- (20) Zhan, C., Wu, T. P., Lu, J. & Amine, K. Dissolution, migration, and deposition of transition metal ions in Li-ion batteries exemplified by Mn-based cathodes - a critical review. *Energ Environ Sci* **11**, 243-257, (2018).
- (21) Wang, C. Y. *et al.* Lithium Difluorophosphate As a Promising Electrolyte Lithium Additive for High-Voltage Lithium-Ion Batteries. *Acs Appl Energ Mater* **1**, 2647-2656, (2018).
- (22) Ma, L. *et al.* LiPO<sub>2</sub>F<sub>2</sub> as an Electrolyte Additive in Li[Ni<sub>0.5</sub>Mn<sub>0.3</sub>Co<sub>0.2</sub>]O<sub>2</sub>/Graphite Pouch Cells. *J Electrochem Soc* **165**, A891-A899 (2018).
- (23) Chen, J. W. *et al.* Outstanding electrochemical performance of high-voltage LiNi<sub>1/3</sub>Co<sub>1/3</sub>Mn<sub>1/3</sub>O<sub>2</sub> cathode achieved by application of LiPO<sub>2</sub>F<sub>2</sub> electrolyte additive. *Electrochim Acta* **290**, 568-576 (2018).
- (24) Sun, X., Lee, H. S., Yang, X. Q. & McBreen, J. Using a boron-based anion receptor additive to improve the thermal stability of LiPF<sub>6</sub>-based electrolyte for lithium batteries. *Electrochem. Solid St.* **5**, A248-A251, (2002).

- (25) Choo, M. H. *et al.* Combination of acid-resistor and -scavenger improves the SEI stability and cycling ability of tin-nickel battery anodes in LiPF<sub>6</sub>-containing electrolyte. *Electrochim. Acta* **112**, 252-257, (2013).
- (26) Wotango, A. S. *et al.* Improved interfacial properties of MCMB electrode by 1-(trimethylsilyl)imidazole as new electrolyte additive to suppress LiPF<sub>6</sub> decomposition. *ACS Appl. Mater. Inter.* **9**, 2410-2420, (2017).
- (27) Yamane, H., Inoue, T., Fujita, M. & Sano, M. A causal study of the capacity fading of Li<sub>1.01</sub>Mn<sub>1.99</sub>O<sub>4</sub> cathode at 80 °C, and the suppressing substances of its fading. *J. Power Sources* **99**, 60-65, (2001).
- (28) Deng, B. W. *et al.* Investigating the influence of high temperatures on the cycling stability of a LiNi<sub>0.6</sub>Co<sub>0.2</sub>Mn<sub>0.2</sub>O<sub>2</sub> cathode using an innovative electrolyte additive. *Electrochim. Acta* **236**, 61-71, (2017).
- (29) Qi, X. *et al.* Lifetime limit of tris(trimethylsilyl) phosphite as electrolyte additive for high voltage lithium ion batteries. *Rsc Adv.* **6**, 38342-38349, (2016).
- (30) Zhang, S. S. Aromatic isocyanate as a new type of electrolyte additive for the improved performance of Li-ion batteries. *J. Power Sources* **163**, 567-572, (2006).
- (31) Han, J. G., Kim, K., Lee, Y. & Choi, N. S. Scavenging materials to stabilize LiPF<sub>6</sub>-containing carbonate-based electrolytes for Li-ion batteries. *Adv. Mater.* **31**, 1804822, (2019).
- (32) Li, Y. K., Zhang, R. X., Liu, J. S. & Yang, C. W. Effect of heptamethyldisilazane as an additive on the stability performance of LiMn<sub>2</sub>O<sub>4</sub> cathode for lithium-ion battery. *J. Power Sources* **189**, 685-688, (2009).
- (33) Song, Y. M., Kim, C. K., Kim, K. E., Hong, S. Y. & Choi, N. S. Exploiting chemically and electrochemically reactive phosphite derivatives for high-voltage spinel LiNi<sub>0.5</sub>Mn<sub>1.5</sub>O<sub>4</sub> cathodes. *J. Power Sources* **302**, 22-30, (2016).
- (34) Grissa, R. *et al.* XPS and SEM-EDX study of electrolyte nature effect on li electrode in lithium metal batteries. *ACS Appl. Energ. Mater.* **1**, 5694-5702, (2018).
- (35) Kowalczy, S. P., Ley, L., Mcfeely, F. R., Pollak, R. A. & Shirley, D. A. X-Ray Photoemission from Sodium and Lithium. *Phys. Rev. B* **8**, 3583-3585, (1973).
- (36) Wood, K. N. & Teeter, G. XPS on Li-battery-related compounds: analysis of inorganic SEI phases and a methodology for charge correction. *ACS Appl. Energ. Mater.* **1**, 4493-4504, (2018).

- (37) Zhang, J. *et al.* Regulating lithium deposition via electropolymerization of acrylonitrile in rechargeable lithium metal batteries. *Nano Energy* **88**, 106298, (2021).
- (38) Yu, Z. A., Cui, Y. & Bao, Z. N. Design principles of artificial solid electrolyte interphases for lithium-metal anodes. *Cell Rep. Phys. Sci.* **1**, 100119, (2020).
- (39) Fu, C. Y. *et al.* Universal chemomechanical design rules for solid-ion conductors to prevent dendrite formation in lithium metal batteries. *Nat. Mater.* **19**, 758-766, (2020).
- (40) Shi, J. Y., Zhang, J., Guo, J. C. & Lu, J. Interfaces in rechargeable magnesium batteries. *Nanoscale Horiz.* **5**, 1467-1475, (2020).
- (41) Hekmatfar, M., Kazzazi, A., Eshetu, G. G., Hasa, I. & Passerini, S. Understanding the electrode/electrolyte interface layer on the Li-rich nickel manganese cobalt layered Oxide cathode by XPS. *ACS Appl. Mater. Inter.* **11**, 43166-43179, (2019).
- (42) Musella, E. *et al.* Detailing the Self-Discharge of a Cathode Based on a Prussian Blue Analogue. *Energies* **13**, 4027, (2020).
- (43) Su, C. C. *et al.* Solvation rule for solid-electrolyte interphase enabler in lithium-metal batteries. *Angew. Chem. Int. Edit.* **59**, 18229-18233, (2020).
- (44) He, M. F., Guo, R., Hobold, G. M., Gao, H. N. & Gallant, B. M. The intrinsic behavior of lithium fluoride in solid electrolyte interphases on lithium. *P. Natl. Acad. Sci. USA* **117**, 73-79, (2020).
- (45) Martha, S. K. *et al.* Solid electrolyte coated high voltage layered-layered lithium-rich composite cathode:  $\text{Li}_{1.2}\text{Mn}_{0.525}\text{Ni}_{0.175}\text{Co}_{0.1}\text{O}_2$ . *J. Mater. Chem. A* **1**, 5587-5595, (2013).
- (46) Gordon, I. J. *et al.* Original implementation of Electrochemical Impedance Spectroscopy (EIS) in symmetric cells: Evaluation of post-mortem protocols applied to characterize electrode materials for Li-ion batteries. *J. Power Sources* **307**, 788-795, (2016).
- (47) Zhang, X. *et al.* Promoting transport kinetics in Li-ion battery with aligned porous electrode architectures. *Nano Lett.* **19**, 8255-8261, (2019).
- (48) Mohanty, D. *et al.* Modification of Ni-rich FCG NMC and NCA cathodes by atomic layer deposition: preventing surface phase transitions for high-voltage lithium-ion batteries. *Sci Rep-Uk* **6**, 26532, (2016).

- (49) Woo, J. J. *et al.* Symmetrical impedance study on inactivation induced degradation of lithium electrodes for batteries beyond lithium-ion. *J. Electrochem. Soc.* **161**, A827-A830, (2014).
- (50) Gilbert, J. A., Shkrob, I. A. & Abraham, D. P. Transition metal dissolution, ion migration, electrocatalytic reduction and capacity loss in lithium-ion full cells. *J. Electrochem. Soc.* **164**, A389-A399, (2017).
- (51) Betz, J. *et al* Cross talk between transition metal cathode and Li metal anode: unraveling its influence on the deposition/dissolution behavior and morphology of lithium. *Adv. Energy Mater.* **9**, 1900574, 2019.
- (52) Fairley, N *et al.* Systematic and collaborative approach to problem solving using X-ray photoelectron spectroscopy. *Applied Surface Science Advances*, **5**, 100112, (2021).

## **Chapter 6: Summary and future directions**

In Chapter 1, we have introduced the basic of Li-ion batteries including the working mechanism, electrode materials and electrolytes. In addition, the motivation of Li metal batteries has been discussed and its mitigation strategies towards the stabilization of interphase has been summarized.

In Chapter 2 and 3, mainly discussed the properties of Li metal anode and the failure mechanism identification for Li metal batteries in carbonate electrolytes. The large volume expansion of Li deposition causing the increasing of concentration overpotential finally leading the failure of Li metal batteries. The better interphase of Li metal anode need to be designed in order to improve the performance of Li metal batteries.

In Chapter 4 and 5, two strategies has been introduced for the stabilization of Li metal anode/electrolyte interphases. The acrylonitrile can be used as electrolyte additive which can be electropolymerized on Li metal via Li deposition process, this in-situ formed protective film can regulating the Li metal deposition to improve the performance of Li metal batteries. Phosphorus pentoxide can be used for Hydrofluoric acid scavenger to eliminate the side reactions in  $\text{LiPF}_6$  based electrolyte system, which can significantly improve the battery performance of Li metal batteries.

The future directions are mainly improving the cycle life of Li metal batteries and the safety of organic liquid-based electrolyte systems.